Mechanism Study of Skin Tissue Ablation by Nanosecond Laser Pulses

A Dissertation

Presented to

the Faculty of the Department of Physics

East Carolina University

In Partial Fulfillment

of the Requirements for the Degree

Doctor of Philosophy in Biomedical Physics

by

Qiyin Fang

Feburary 2002

Mechanism Study of Skin Tissue Ablation by Nanosecond Laser Pulses

by

Qiyin Fang

APPROVED BY:
ADVISOR OF DISSERTATION_____

XIN-HUA HU, Ph.D.
DEPARTMENT OF PHYSICS

COMMITTEE MEMBER_____

MUMTAZ A. DINNO, Ph.D.
DEPARTMENT OF PHYSICS

COMMITTEE MEMBER_____

EDWARD J. SEYKORA, Ph.D.
DEPARTMENT OF PHYSICS

COMMITTEE MEMBER_____

MOHAMMAD R. SALEHPOUR, Ph.D.
DEPT. OF RADIATION PHYSICS
M. D. ANDERSON CANCER CENTER
UNIVERSITY OF TEXAS

COMMITTEE MEMBER_____

GERHARD W. KALMUS, Ph.D.
DEPARTMENT OF BIOLOGY

DEAN OF THE GRADUATE SCHOOL_____

THOMAS L. FELDBUSH, Ph.D.

Acknowledgements

I would like to thank the Physics Department of ECU for their support and confidence in my ability to perform to their expectations, for everybody's kindness to me for the five and half years. Most of all, I am greatly indebted to Dr. Xin-Hua Hu, who first recruited me and then served as my advisor for both of my MS thesis and Ph.D. dissertation, for his time and patience. His ability and originality made this project and writing of this manuscript possible.

I would like to thank Dr. Mumtaz Dinno for his trust and encouragement throughout the years as well as these discussions that brought me to the world of biophysics.

Thanks and appreciation are also due to Drs. Gerhard Kalmus, Edward Seykora, and Mohammad Salehpour for serving on my dissertation committee, reviewing this manuscript, and for making sure that I met all the graduation requirements set by the department and the university.

My appreciation is also due to Dr. Xiaoning Pan and Dr. Jianguo Tian, who were visiting faculty at ECU, for the valuable discussion with them and their encouragement. I worked with Dr. Pan in the tissue ablation experiments and with Dr. Tian in optical breakdown and n_2 measurement in water. I would like to thank Mr. Michael Cariveau who did the histology measurements.

I would also like to express my appreciation to the following:

Mr. Ken Jacobs, Raymond Mills, Jim Gilbert, and Carl Hartsfield for making the new devices and helping to redesign and repair them. Working with them is a very precious learning experience.

Mr. Charles Goodman, Mr. Michael Cariveau, and Yong Du, who are always the ones I can turn to, for their friendship.

My thanks also go to the faculty, staff and my fellow graduate students in the department of physics for their friendship.

Finally, I would like to thank my parents for their trust, support, and understanding throughout the years. I own much gratitude to my wife, Vivian Jin, for the encouragement and support.

To Vivian

Table of Contents

List of Figures

Abstract

Qiyin Fang MECHANISM STUDY OF SKIN TISSUE ABLATION BY NANOSECOND LASER PULSES. (Under the direction of Dr. Xin-Hua Hu) Department of Physics, February 2002.

Understanding the fundamental mechanisms in laser tissue ablation is essential to improve clinical laser applications by reducing collateral damage and laser pulse energy requirement. The motive of this dissertation is to study skin tissue ablation by nanosecond laser pulses in a wide spectral region from near-infrared to ultraviolet for a clear understanding of the mechanism that can be used to improve future design of the pulsed lasers for dermatology and plastic surgery.

Multiple laser and optical configurations have been constructed to generate 9 to 12ns laser pulses with similar profiles at 1064, 532, 266 and 213nm for this study of skin tissue ablation. Through measurements of ablation depth as a function of laser pulse energy, the 589nm spectral line in the secondary radiation from ablated skin tissue samples was identified as the signature of the occurrence of ablation. Subsequently, this spectral signature has been used to investigate the probabilistic process of the ablation near the threshold at the four wavelengths. Measurements of the ablation probability were conducted as a function of the electrical field strength of the laser pulse and the ablation thresholds in a wide spectral range from 1064nm to 213nm were determined. Histology analysis and an optical transmission method were applied in assessing of the ablation depth per pulse to study the ablation process at irradiance levels higher than threshold. Because more than 70% of the wet weight of the skin tissue is water, optical breakdown and backscattering in water was also investigated along with a nonlinear refraction index

measurement using a z-scan technique. Preliminary studies on ablation of a gelatin based tissue phantom are also reported.

The current theoretical models describing ablation of soft tissue ablation by short laser pulses were critically reviewed. Since none of the existing models was found capable of explaining the experimental results, a new plasma-mediated model was developed. A laser-induced and localized thermal ionization pathway has been investigated and it was found to have significant influence on the initial free electron density during plasma formation due to the combination of strong light absorption by chromophores and confined temperature rise in the chromophores. Good agreements have been found between the new plasma-mediated ablation model and experimental results. The implications of this dissertation research to the future improvement of laser systems in dermatology and plastic surgery are discussed.

Mechanism Study of Skin Tissue Ablation by Nanosecond Laser Pulses

A Dissertation

Presented to

the Faculty of the Department of Physics

East Carolina University

In Partial Fulfillment

of the Requirements for the Degree

Doctor of Philosophy in Biomedical Physics

by

Qiyin Fang

Feburary 2002

Mechanism Study of Skin Tissue Ablation by Nanosecond Laser Pulses

by

Qiyin Fang

APPROVED BY:
ADVISOR OF DISSERTATION_____
XIN-HUA HU, Ph.D.
DEPARTMENT OF PHYSICS

COMMITTEE MEMBER_____
MUMTAZ A. DINNO, Ph.D.
DEPARTMENT OF PHYSICS

COMMITTEE MEMBER_____
EDWARD J. SEYKORA, Ph.D.
DEPARTMENT OF PHYSICS

COMMITTEE MEMBER_____
MOHAMMAD R. SALEHPOUR, Ph.D.
DEPT. OF RADIATION PHYSICS
M. D. ANDERSON CANCER CENTER
UNIVERSITY OF TEXAS

COMMITTEE MEMBER_____
GERHARD W. KALMUS, Ph.D.
DEPARTMENT OF BIOLOGY

DEAN OF THE GRADUATE SCHOOL_____
THOMAS L. FELDBUSH, Ph.D.

Acknowledgements

I would like to thank the Physics Department of ECU for their support and confidence in my ability to perform to their expectations, for everybody's kindness to me for the five and half years. Most of all, I am greatly indebted to Dr. Xin-Hua Hu, who first recruited me and then served as my advisor for both of my MS thesis and Ph.D. dissertation, for his time and patience. His ability and originality made this project and writing of this manuscript possible.

I would like to thank Dr. Mumtaz Dinno for his trust and encouragement throughout the years as well as these discussions that brought me to the world of biophysics.

Thanks and appreciation are also due to Drs. Gerhard Kalmus, Edward Seykora, and Mohammad Salehpour for serving on my dissertation committee, reviewing this manuscript, and for making sure that I met all the graduation requirements set by the department and the university.

My appreciation is also due to Dr. Xiaoning Pan and Dr. Jianguo Tian, who were visiting faculty at ECU, for the valuable discussion with them and their encouragement. I worked with Dr. Pan in the tissue ablation experiments and with Dr. Tian in optical breakdown and n_2 measurement in water. I would like to thank Mr. Michael Cariveau who did the histology measurements.

I would also like to express my appreciation to the following:

Mr. Ken Jacobs, Raymond Mills, Jim Gilbert, and Carl Hartsfield for making the new devices and helping to redesign and repair them. Working with them is a very precious learning experience.

Mr. Charles Goodman, Mr. Michael Cariveau, and Yong Du, who are always the ones I can turn to, for their friendship.

My thanks also go to the faculty, staff and my fellow graduate students in the department of physics for their friendship.

Finally, I would like to thank my parents for their trust, support, and understanding throughout the years. I own much gratitude to my wife, Vivian Jin, for the encouragement and support.

To Vivian

Table of Contents

List of Figures

List of Tables

List of Symbol, Constants, and Abbreviations

Symbol	Name	Value	Unit
α	Ionization coefficient		m^{-1}
α'	Linear absorption coefficient		m^{-1}
A	Area		m^2
c	Light speed in vacuum	2.99×10^{8}	m/s
C	Initial confinement coefficient		
C_m	Specific heat for chromophores	2.51×10^{3}	J/kg·K
C_s	Speed of sound in water	1500	m/s
C_v	Specific heat at constant volume	2.51×10^{3}	J/kg·K
Δ	Effective ionization potential ≈ E_{ion}		eV
d	Tissue slab thickness		m
D	Penetration depth		m
e	Unit electron charge	1.602×10^{-19}	C
$\mathcal{E}$	Electric field		V/m
$\mathcal{E}_0$	Permittivity of vacuum,	8.854×10^{-12}	F/m
E	Particle energy		J
E´	Energy density in tissue		J/m^3
E_0	Ground state for electrons at room temperature T_0		J
E_{ab}	Excited State for an electron after absorbing a photon		J
E_{av}	Steady state energy for an average carrier		N·m
E_1	Threshold energy for ionization of water,	6.5	eV
E_{ion}	Binding energy	4.56	eV
E_{p0}	Pulse energy for incident laser pulse		J
E_T	Average energy for hot carriers		J
E_{th}	Threshold energy density	190	J/m^3
Φ	Laser fluence		J/m^2
Φ_0	Laser original fluence		J/m^2
F	Helmholtz free energy		J or eV
Γ	Grüneisen parameter	0.1~1.0	
h	Planck's constant	6.626×10^{-34}	J·s
$\hbar$	Planck's constant = $h/2\pi$		J·s
η_c	Cascade ionization rate		s^{-1}
η_m	Multiphoton ionization rate		s^{-1}
η_{th}	Thermal ionization rate		s^{-1}
I	Laser irradiance		W/m^2

I_0	Laser peak irradiance		W/m^2
k(E)	Wave vector for the carrier, = mv/ħ		s/kg·m
k_B	Boltzmann constant	1.381×10^{-23}	J/K
		8.617×10^{-5}	eV/K
κ_w	Thermal conductivity of water	0.57	J/m·s·K
K	Number of photons needed in multiphoton ionization		
λ	Mean free path between collisions		m
$\lambda(E)$	Momentum-relaxation mean free path		m
λ_{av}	Average mean free path in $0 \le E \le E_1$		
L_v	Latent heat of water	2.26×10^3	J/kg
μ	Chemical potential $\mu \approx E_{ion}/2$		eV
μ_α	Absorption coefficient		m^{-1}
μ_s	Scattering coefficient		m^{-1}
μ_s'	Effective scattering coefficient		m^{-1}
μ_T	Total attenuation coefficient		m^{-1}
m′	Reduced mass ≈ m_e /2		kg
m*(E)	Effective mass		kg
m_{ch}	Chromophore mass ≈ $n_b \times m_p$	1.67×10^{-16}	kg
m_e	Electron mass,	9.109×10^{-31}	kg
m_{H2O}	Molar mass of Water		kg
m_p	Proton mass,	1.67×10^{-27}	kg
ν	Optical frequency of the incident laser pulse		m^{-1}
N	Total number of electrons in the region		
n	Number of electrons per molecule in water ≈1~2		
n_0	Refraction index	1.3	
n_{ch}	Number of bound electrons in a chromophore	10^{11}	
n_j	Primary quantum number of the j^{th} particle		
p	Pressure		Pa or N/m^2
P_0	Atmosphere pressure	1.01×10^5	Pa or N/m^2
$P(E, E_1)$	Probability that an electron avoid energy loss over a path that acquires threshold energy E_1, starting at energy 0.		
$P_0(t)$	Probability of avoiding a collision in a time t		
$P_1(E, t)$	Probability that an electron traveling for a time t avoids a momentum-relaxing collision.		
$P_2(E, t)$	Probability that an electron traveling for a time t and avoids significant energy-relaxation.		
P_T	Probability of hot electron thermalisation		
P_1^T	Probability of of lucky flight from average energy		
P_2^T	Probability of of lucky drift from average energy		

ρ_{ch}	Chromophore molecular density in tissue	$10^{22\sim24}$	m^{-3}
ρ_{cr}	Critical free carrier density	$10^{24\sim26}$	m^{-3}
ρ_{H2O}	Mass density of water		kg/m^3
ρ_m	Mass density of chromophore	1.35×10^3	kg/m^3
ρ_{mol}	Molecular density of condensed matter	$10^{28\sim29}$	m^{-3}
R	Reflectance		
R_{ch}	Chromophore character size		m
σ_a	Absorption cross section		m^2
τ_0	Laser pulse width	9.0×10^{-9}	s
$\tau(E)$	Scattering time constant		s
τ_c	Pressure dissipation time		s
$\tau_E(E)$	Energy-relaxation time constants		s
$\tau_m(E)$	Momentum-relaxation time constants		s
τ_{H2O}	Mean momentum transfer collision time for electrons in water	1.0×10^{-15}	s
t	Time period		s
T	Temperature		K
T_0	Room temperature	300	K
T_c	Critical temperature for vaporization	373	K
U	Total energy		J or eV
$v_g(E)$	Group velocity of the electron		m/s
$v_d(E)$	Drifting velocity of the electron		m/s
ω	Photon angular frequency		s^{-1}
ω_j	Vibration frequency of the j^{th} particle		s^{-1}
ω_p	Phonon angular frequency		s^{-1}
W_{th}	Threshold radiant energy density		J/m^3
Z	Distribution function		

Chapter 1 Introduction

Since its invention, in the early nineteen sixties, lasers become very valuable tools in a variety of fields including science, engineering, and medicine. Along with diagnostic applications, laser surgery and other therapeutic treatments have been extensively studied. The four most important parameters of surgical laser are wavelength, pulse duration, energy, and focusing spot size. The goal of studying surgical application of laser is to find out the optimum combination of these four parameters for certain procedures, while the laser system by itself can be made into a small box with four controls that can obtain any combination of the corresponding parameters.

Ophthalmologic applications such as treating retinal detachment in the eye were also carried out using selective absorption of argon laser [Hillegersberg 1997]. Whereas in dermatology, Goldman pioneered in the treatments of a variety of skin tumors [Hillegersberg 1997].

In the early applications during 1960's and 70's, clinical lasers in use were mostly continuous-wave (cw) systems with simple structures. As laser technology advanced, pulsed laser systems became readily available since early 1980's and laser surgery using short laser pulse became widely accepted. Consequently, investigations on the physical mechanisms underlying tissue ablation with short laser pulse have become increasingly active [Cheong, Prahl 1990; Deutsch 1991; Welch, Motamedi 1991; Oraevsky, Esenaliev 1992; Albagli, Dark 1994; Itzkan, Albagli 1995; Kennedy 1995; Kennedy, Boppart 1995; Vogel, Nahen 1996; Hillegersberg 1997]. Short laser pulses can significantly reduce the

collateral tissue damage that occurs when cw is used by minimizing the deposited energy while still maintaining an irradiance above the threshold, therefore, leading to faster patient recovery. In addition, pulsed lasers offer accurate control over the amount of tissue removed through precise control of the pulse energy delivered to the patient. These features are especially important in the precision procedures required in ophthalmology, dermatology, and plastic surgery.

Among the most important phenomena identified with tissue ablation by nanosecond laser pulses, the presence of an irradiance threshold and its variation as a function of laser parameters and tissue optical properties are most important. The formations of shock waves, acoustic transients, and bubbles have also been documented [Oraevsky, Esenaliev 1992]. Understanding the fundamental mechanisms in laser tissue ablation is essential for the improvement of clinical laser applications by reducing collateral damage and laser pulse energy requirements. Numerous models have been proposed to understand the above phenomena, which may be separated into three major types according to their proposed pathways leading to tissue ablation. They are namely: the photothermal models represented by the selective photothermolysis [Anderson and Parrish 1983] and the photomechanical models [Albagli, Banish 1994; Albagli, Dark 1994; Albagli, Dark 1994; Albagli, Perelman 1994]; the photochemical model [Srinivasan 1986; Srinivasan, Braren 1986; Pettit and Sauerbrey 1993; Sentrayan, Jr. 1998]; and the plasma-medicated models [Kennedy 1995; Kennedy, Boppart 1995; Vogel, Nahen 1996]. A key difference among these models is whether there is laser-induced plasma formation during the ablation. Therefore, clinical laser design depends on a particular theoretical model. For example,

the plasma-mediated ablation model has been developed for optical breakdown in water and other aqueous solutions and ablation of ocular tissues. Based on this model, ophthalmologic laser systems typically use a focused beam with a spot diameter as small as 10μm and pulse energy in the order of 1mJ for nanosecond pulses [Docchio, Sacchi 1986; Stern, Schoenlein 1989; Niemz, Klancnik 1991; Pettit and Ediger 1993; Juhasz, Hu 1994; Juhasz, Frieder 1999]. On the other hand, the designs of dermatology lasers are based on the photothermolysis model and use much larger beam diameter on the target, 2 or 3mm, which requires pulse energy as high as over 1J or more [Reichel, Schmidt-Kloiber 1987; Loesel, Niemz 1996; Palanker, Turovets 1997; Lee and Doukas 1999]. This has caused significant collateral damage and costly system implementations. Hence, it is expected that a clear understanding of the mechanism underlying soft tissue ablation by nanosecond laser pulses will significantly improve future design of the pulsed lasers for dermatology and plastic surgery. Furthermore, an improved laser design may eliminate the current need of multiple laser systems for treatment of pigmented lesions of different colors by enabling efficient ablation of different pigments or tissues at a single wavelength. This dissertation presents a comprehensive research project to study the fundamental mechanism of skin tissue ablation by nanosecond laser pulses in a wide spectral region from near-infrared to ultraviolet.

In Chapter 2, a general description for the list of events occurring sequentially from femtoseconds to milliseconds time scale during short pulse laser ablation is first introduced. Following a brief review of the basic structure of human skin and the optical properties of its components, the existing theoretical models suitable for soft tissue

ablation by nanosecond laser pulses are examined. It is pointed out that these models are not compatible with each other and only capable of explaining part of the experimentally observed phenomenon, i.e., wavelength dependence of ablation thresholds and its probabilistic behavior.

Consequently, a new plasma ablation model is derived in Chapter 3, which combines the concepts from the existing models. Specifically, the rate equation approach in the existing plasma-mediated model has been adopted as the framework of this modification. Considering the complexity of skin tissue components, a laser-induced and localized thermal ionization pathway is introduced to obtain a modified ~~the~~ rate equation. Combining the strong absorption from chromophores proposed by the selective photothermolysis and the confinement of the mechanical and thermal response by the inertial confinement model, the localized thermal ionization rate is obtained from the sudden rise in temperature confined within the chromophores. The modified theoretical model is then evaluated with the experimental parameters for ablation of skin tissue by nanosecond laser pulses. It is found that the localized thermal ionization plays a significant role during plasma formation and greatly affects the optical breakdown thresholds.

In Chapter 4, the probabilistic behavior of the ablation thresholds as a function of the laser electric field has been experimentally studied on fresh porcine skin tissue. The secondary radiation spectra from the plasma were obtained and analyzed. The sodium atom spectra line at 589nm in the ablation secondary radiation spectra has been identified as the signature for the occurrence of ablation. Subsequently, this signature has been

applied to determine the ablation thresholds as a function of laser electric field at wide wavelength range and variety of spot sizes. Histology and optical transmission measurements have been performed to confirm the occurrence of ablation in tissue at irradiance around the thresholds determined by the optical signature via measurements of the ablation depth per pulse. Different ablation rate were found between ablation of the epidermis and dermis sections using the drilling setup at 1064nm, 532nm, 266nm, and 213nm.

Since more than 70% of soft tissue is water, optical breakdown and backscattering in water for nanosecond pulses at 1064nm and 532nm were also investigated along with a nonlinear refraction index measurement using a z-Scan technique. This is presented in Chapter 5 in which also presented is the preliminary results on optical breakdown measurements on Gelatin based tissue phantom.

In Chapter 6, a summary of the theoretical and experimental work as well as future directions of this research is given. In Appendices, some experimental and instruments setup, interfacing programs, and statistical methods are documented for future references.

Chapter 2 Background

In this chapter, the major existing models that are relevant to the study of skin tissue ablation by nanosecond laser pulses will be discuss. A general description of the laser-tissue interaction process and skin optics will be provided in section 2.1. In the following three sections, three major types of tissue ablation models will be critically reviewed. A microscopic model of the cascade ionization will be discussed in the last section to achieve a better understanding of the probabilistic behavior of the ablation process near the threshold.

2.1 Soft Tissue Ablation by Laser Pulses and Skin Optics

The observed phenomena identified with tissue ablation by short laser pulses have been summarized as follows [Oraevsky, Esenaliev 1992; Oraevsky, Jacques 1995]:

1. The presence of an irradiance threshold of the pulsed laser radiation under which no ablation can be observed;
2. The variation of the irradiance threshold as a function of laser parameters and tissue optical properties;
3. The formation of shock waves and acoustic transients;
4. The emission of visible sparks;
5. The gasdynamic sputtering of the ablation products with supersonic velocities.

It is worth noting that the experimental studies on skin tissue ablation provide convincing evidences of other characteristics of tissue ablation in addition to those summarized above and will be discussed in details in the following chapters.

Numerous models have been proposed to understand the above phenomena, which may be separated into three major categories according to their proposed pathways leading to tissue ablation. These are: the photothermal models represented by the selective photothermolysis [Anderson and Parrish 1983] and the photomechanical models [Albagli, Banish 1994; Albagli, Dark 1994; Albagli, Dark 1994; Albagli, Perelman 1994]; the photochemical model [Srinivasan 1986; Srinivasan, Braren 1986; Kitai, Popkov 1991; Pettit and Sauerbrey 1993; Sentrayan, Jr. 1998]; the plasma-mediated models [Kennedy 1995; Kennedy, Boppart 1995; Vogel, Nahen 1996]. A key difference among these models is whether a laser-induced plasma exists to cause the ablation. Before analyzing these models, it is necessary to briefly examine the optical and thermal responses of tissue to laser radiation on different time scales based on the vast volume of literature on time-resolved studies of condensed matters [DeMichelis 1969; Bloembergen 1974].

The photon-electron interaction and collisions between quasi-free electrons in condensed matters occur on femtosecond scales. Subsequently on picosecond scales, electron-ion interaction and collisions between ions become possible and the lattice temperature of the illuminated region starts to rise due to the collisions between atoms [Smith 1978]. The thermal response of the tissue is localized and no global change is expected within a few nanoseconds [Albagli, Perelman 1994]. Acoustical shock waves propagate outside the illuminated region a few tens nanoseconds after the laser pulse.

This pressure build-up could subsequently breaks the tissue structure and removes particles from the surface in additional to the high pressure due to possible plasma formation in the illuminated region. The heat converted from the optical energy dissipates inside tissue on time scales of sub-milliseconds or longer. In the case of continuous wave or laser pulses with very high repetition rate, the energy dissipation may be interrupted by the subsequent pulses such that a steady state with an elevated temperature can therefore be maintained in the illuminated region. For laser pulses with low repetition rate, the temperature of the illuminated region will relax to ambient temperature before the successive pulses. Therefore, each pulse can be treated independently to other pulses, which is also called the single-pulse condition.

An exact assessment of light propagation inside tissue requires the understanding of its biological composition and major component structure. A concise description of human skin structure was given by Parrish and Anderson [Anderson and Parrish 1981; Parrish and Deutsch 1984] and those parts relevant to this study will be summarized here. Figure 2-1 is a diagrammatic cross section of human skin [Parrish and Deutsch 1984]. The human skin has two main layers: the epidermis and the dermis, which are connected by the epidermis-dermis junction. The keratinocytes are major cells in the epidermis producing keratin, which are the fibrous protective proteins in skin. Keratinocytes are derived from a single germinative layer called basal cells, which divides and pushes daughter cells outward toward the surface and forms the tough stratum corneum as the top sub-layer of the epidermis with keratin and lipids. Specialized cells called melanocytes reside between basal cells in the innermost epidermis. These cells produce

melanin, a complex macromolecular protein derived from tyrosine, which strongly absorbs visible to ultraviolet light. Dendrites of the melanocytes interdigitate between keratinocytes and facilitate the transfer of melanin containing granules, called melanosomes, into the keratinocytes. These melanosomes are carried outward within the keratinocytes and ultimately deposited in the stratum corneum.

The dermis is mostly a semisolid mixture of fibers, water, and a viscous gel called the ground substance, which consists largely of water and mucopolysaccharides. There are three types of fibers present in the ground substance: collagen, reticulum, and elastin. Collagen constitutes about 70% of the dry weight of dermis. The complex nature of the dermis and its fibers make it a tissue with high tensile strength, which can resist compression but, at the same time, remains pliable and movable. Like melanin in epidermis, hemoglobin is the main chromophore that absorbs light in dermis from near-infrared to ultraviolet. Absorption of the scattered light by chromophores, such as melanin in epidermis and hemoglobin in dermis, gives skin its color. Human skin is difficult to obtain in large quantities for *in vitro* studies so an animal model is desired. Because of its similarities to human skin in histology, morphology, cellular composition, immunoreactivity, and physical properties [Bartell and Mustoe 1987; Lavker, Dong 1990], the white domestic pig has thus been selected as the animal model used for studying laser interaction with skin tissues.

The propagation of light in the skin can be accurately described within the framework of radiative transfer theory in which the optical properties of a homogeneous skin layer, such as the epidermis or dermis, can be described with three parameters: the absorption

coefficient μ_α, the scattering coefficient μ_s, and the scattering phase function $p(\theta)$, which is the probability of light being scattered from the incident direction to another direction of θ angular distance [Ishimaru 1978]. When light penetrates deep into a turbid medium such as the skin, at a distance much larger than $1/\mu_s$, most of the photons suffer multiple scattering and a light diffusion equation can be used as a good approximation to the radiative transfer equation to calculate the light distribution. In these cases, a penetration depth D for an incident light beam is provided by [Cheong, Prahl 1990]:

$$D = \left[3\mu_\alpha \left(\mu_\alpha + \mu_s' \right) \right]^{-\frac{1}{2}}, \tag{2.1}$$

where $\mu_s'=(1-g)\,\mu_s$ and $g = \int_{4\pi} p(\theta)\cos\theta\, d\Omega$. The optical parameters of μ_s, μ_α and g from 250 to 1000nm of human epidermis and dermis have been reported [van Gemert, Jacques 1989; Cheong, Prahl 1990; Welch and Gemert 1995]. These parameters at 213nm have been estimated from literature [van Gemert, Jacques 1989] and the tissue transmittance measurement of $\mu_t = \mu_s + \mu_\alpha$ down to 200nm, which will be discussed later in Chapter 4.

2.2 The Photothermal Models

All photothermal models explain the ablation process because of the direct transformation of optical energy into thermal energy via the absorption of the pulsed laser radiation in tissue or pigments. The subsequent rise of the local temperature causes the irradiated region to undergo an overheated metastable state within a time interval shorter than the heat diffusion time. Temperature higher than normal human body temperature

T_0 will result in significant tissue damages [Anderson and Parrish 1983]. For instance, if temperature rises above 60° to 70°C, structural proteins including collagens are denatured. Nucleic acids will start to be denatured and membrane starts becoming permeable from 70° to 80°C. Above 100°C, vaporization of tissue water with fast volume expansion occurs and it is followed by carbonization of the dry mass. Rapid vaporization was regarded as the direct reason leading to tissue ablation. Various photothermal models have been developed for both continuous wave laser and pulsed laser ablation.

Considering a collimated beam with a top-hat spatial profile, one can find the minimum thermal energy needed to vaporize the tissue in a very crude approximation [Welch, Motamedi 1991]:

$$\Delta Q = \Phi \cdot A = \rho \cdot A \cdot D\left[C_v \left(T_c - T_0 \right) + L_v \right], \tag{2.2}$$

where Φ is the laser fluence, A is the beam cross section area, C_v=4.2J/g is the specific heat of the tissue, m is the illuminated volume mass, ρ=1.03g/cm^3 is the tissue density, D is the laser penetration depth, and L_v=2.26$\times 10^3$J/g at 1atm is the latent heat of vaporization for water, T_0=293K is the ambient temperature and T_c=373K is the vaporization temperature. Then the required energy density to achieve ablation is given by

$$E_{th} = \frac{\Phi}{D} = \rho\left[C_v \left(T_c - T_0 \right) + L_v \right]. \tag{2.3}$$

which can be calculated as 2554J/cm^3 at 1064nm.

Beyond the above simple considerations of photothermal action, two models are specific interesting for their intended applications to skin tissue ablation by nanosecond pulses. Ablation through high temperature protein denaturation and thermal diffusion of the absorbed energy in targeted chromophores inside tissue is proposed in a selective photothermolysis model [Anderson and Parrish 1983]. The effect of abrupt changes in pressure is considered in a photomechanical model [Izatt, Albagli 1991; Albagli, Banish 1994; Albagli, Dark 1994; Albagli, Perelman 1994; Itzkan, Albagli 1995].

2.2.1 The Selective Photothermolysis Model

In order to achieve precise ablation of small targets inside tissue while avoiding excess collateral damage to the surrounding tissue, a selective photothermolysis model have been proposed [Anderson and Parrish 1983]. In this model, the ablation of targeted chromophores inside tissue relies on selective absorption of short laser pulses at optimum wavelength for the chromophores while the light absorption in the surrounding region is minimal. The pulse duration is selected to be short enough that the total energy deposited into tissue is limited while the ablation threshold in irradiance is exceeded. Hence, the heat diffusion beyond the targeted region is limited such that the rise in temperature of the surround tissue is kept at minimum. On the other hand, the pulse duration should be long enough to minimize the intensity of the shock waves from targets that may damage the surrounding tissue.

If both the appropriate wavelength and pulse duration have been achieved, thermal diffusion during exposure can be neglected. The temperature rise of the target is then given by:

$$\Delta T = \frac{\varepsilon}{\rho_m C_V}, \tag{2.4}$$

where ε is the absorbed energy density, C_V is the target heat capacity and ρ_m is the target mass density. In most mammalian tissues, $\Delta T \geq 40^{\circ}C$ should correspond to significant thermal damage. For a target with $\mu_\alpha d<1$, where μ_α is the absorption coefficient, and d is the distance between the target and surface of the skin,

$$\varepsilon \cong f \cdot \Phi_{th} \cdot \mu_\alpha, \tag{2.5}$$

where Φ_{th} is the laser threshold fluence for that specific target, and the incident fluence is decreased by a factor f before reaching the targets. Hence, the threshold fluence is given by

$$\Phi_{th} \cong \frac{\rho_m \cdot C_V \cdot \Delta T}{f \cdot \mu_\alpha}, \tag{2.6}$$

for $\mu_\alpha d<1$. For cases when $\mu_\alpha d \geq 1$, one can estimate the threshold by assuming that all the energy incident on the cross sectional area A_t of the target chromophores along the incident beam direction is absorbed and uniformly distributed into the target volume V_t, giving

$$\Phi_{th} \cong \frac{\rho_m \cdot C_V \cdot \Delta T \cdot A_t}{f \cdot V_t}. \tag{2.7}$$

2.2.2 The Inertial Confinement Model

The irradiation of materials and biological tissues by short laser pulses may be accompanied by secondary effects besides diffusive heating, such as generation of powerful acoustic transients with pressure amplitude of up to a few hundred atmospheres [Albagli, Dark 1994]. Acoustic transients formed within the illuminated region will lead to the expulsion of micropaticles by acting on the surface of the material without evaporation.

An inertial confinement model has been developed [Albagli, Perelman 1994] by assuming that the pressure build-up plays a key role in initializing ablation under the condition of initial confinement, in which the laser pulse duration (τ_p) is shorter than the time for the laser-induced pressure change to dissipate (τ_c). An inertial confinement coefficient, defined as $C= \tau_p/\tau_c$, is used to check the applicability of this assumption in which $\tau_c=D/C_s$ is defined as the pressure dissipation time, D is the optical penetration depth defined in Eq. (2.1) and $C_s \sim 1500$m/s is the speed of sound in the tissue. Within the confinement regime with $C < 1$, the thermal energy density $\Delta\varepsilon$ deposited into the illuminated region is completely converted into thermoelastic stress Δp given by [Paltauf and Schmidtkloiber 1995]:

$$\Delta p = \Gamma \cdot \Delta \varepsilon \,, \tag{2.8}$$

where Γ is the Grüneisen parameter of the tissue. This result can be obtained through the following derivations [Ashcroft and Mermin 1976].

If the Helmholtz free energy of the illuminated region can be written as F(T, V), where T is its temperature and V is its volume, the pressure of the illuminated region was found as

$$p = -\left(\frac{\partial F}{\partial V}\right)_T . \tag{2.9}$$

The free energy function can be generally expressed as:

$$F = -kT \ln Z = -kT \ln\left(\sum_i e^{-E_i/kT}\right) \tag{2.10}$$

where Z is the distribution function and E_i is the energy of state *i*. If the lattice oscillations are small, E_i is the sum of the lattice equilibrium energy and all phonon vibration energy:

$$E_i = \sum_j \left(n_j + \frac{1}{2}\right)\hbar\omega_j , \tag{2.11}$$

where j identifies different phonon, n_j is the corresponding quantum number. Z includes all possible quantum states that need sums over n_j:

$$\begin{aligned} Z &= e^{-U/kT} \prod_j e^{-\frac{1}{2}(\hbar\omega_j/kT)} \left(\sum_{n_j=0}^{\infty} e^{-n_j\hbar\omega_j/kT}\right) \\ &= e^{-U/kT} \prod_j e^{-\frac{1}{2}(\hbar\omega_j/kT)} \left(\frac{1}{1-e^{-\hbar\omega_j/kT}}\right) \end{aligned} . \tag{2.12}$$

Substitute Eq. (2.12) into Eq. (2.10),

$$F = U + kT\left[\sum_j \frac{1}{2}\frac{\hbar\omega_j}{kT} + \ln\left(1-e^{-\hbar\omega_j/kT}\right)\right]. \tag{2.13}$$

When the volume V changes, the vibration frequency ω_j will change as well, hence the equation of state is given by:

$$\begin{aligned} p &= -\frac{dU}{dV} - \sum_j \left(\frac{1}{2}\hbar + \frac{\hbar}{e^{-\hbar\omega_j/kT} - 1} \right) \frac{d\omega_j}{dV} \\ &= -\frac{dU}{dV} - \sum_j \left(\frac{1}{2}\hbar\omega_j + \frac{\hbar\omega_j}{e^{-\hbar\omega_j/kT} - 1} \right) \frac{1}{V} \frac{d\ln\omega_j}{d\ln V} \end{aligned} . \tag{2.14}$$

The quantity inside the bracket is the average vibration energy $\bar{E}$. Grüneisen assumed that the quantity:

$$\Gamma = \frac{d\ln\omega_j}{d\ln V} \tag{2.15}$$

is the same for all vibration modes. Therefore, Eq. (2.14) becomes:

$$p = -\frac{dU}{dV} + \Gamma\frac{\bar{E}}{V} . \tag{2.16}$$

Under the inertial confinement condition, the total energy U does not change with the volume of the illuminated region within the laser pulse duration and therefore Eq. (2.8) is obtained.

To achieve ablation of certain type of biological tissue when the inertial confinement condition is satisfied ($C \leq 1$), a threshold pressure, p_{th}, has to be surpassed which corresponds to a threshold energy density $\varepsilon_{th}^{C\leq 1}$ through Eq. (2.8), which shows $\varepsilon_{th}^{C\leq 1}$ is independent of the ablation wavelength since both p_{th} and Γ are properties of the tissue. $\varepsilon_{th}^{C\leq 1}$ has been determined to be a constant of about $200 J/cm^3$ by averaging published data on calcified tissues at wavelengths ranging from 266 to 1064nm [Albagli, Perelman

1994] and confirmed by experiments on bovine shank bone and human arterial calcified plaque ranging from 308nm to 2μm [Itzkan, Albagli 1995].

To examine the inertial confinement condition, the order of magnitude of the pressure dissertation time τ_c can be roughly estimate from the value of the characteristic time for motion related to thermal fluctuation inside tissue. If assuming the energy deposited in the tissue is converted into kinetic energy with a speed v_c:

$$mv_c^2 \sim \Phi \cdot D^2, \tag{2.17}$$

with the penetration depth $D \sim \tau_c \cdot v_c$ and the mass of the illuminated region $m \sim D^3 \cdot \rho$, the pressure dissertation time is given by:

$$\tau_c \approx \sqrt{D^3 \rho / \Phi} = \left(D^2 \rho / \varepsilon \right)^{1/2}, \tag{2.18}$$

which ranges from 74μs to 1.5ms.

The ablation threshold has also been estimated in the cases when the inertial confinement condition are not met, i.e. C>1 [Albagli, Perelman 1994]. The corresponding threshold energy density, $\varepsilon_{th}^{C>1}$, is higher because of the pressure dissipation. To relate the two thresholds, one may separate the laser pulse with a total energy density of $\varepsilon_{th}^{C>1}$ into two parts: a fraction of the pulse with duration $\tau_p' < \tau_p$ that the pressure is still confined with a deposited energy density of E' in the tissue; the rest of the pulse with duration $\tau_p - \tau_p'$ and energy density $\varepsilon E_{th}^{C>1} - \varepsilon'$. Since τ_p' is the portion of the pulse satisfies the inertial confinement condition, $\tau_p' = (D^2 \rho / \varepsilon')^{1/2}$. By assuming the square wave temporal profile, $\varepsilon' = (\tau_p' / \tau_p)\, \varepsilon_{th}^{C>1}$. Consequently,

$$\varepsilon' = \frac{\tau_p'}{\tau_p} \cdot \varepsilon_{th}^{C>1} = \frac{\tau_p'}{C \cdot \tau_p} \cdot \varepsilon_{th}^{C>1} = \frac{\sqrt{\frac{D^2 \rho}{\varepsilon'}}}{C \cdot \sqrt{\frac{D^2 \rho}{\varepsilon_{th}^{C>1}}}} \cdot \varepsilon_{th}^{C>1} \quad . \tag{2.19}$$

$$\varepsilon'^{\frac{3}{2}} = C \cdot \left(\varepsilon_{th}^{C>1}\right)^{\frac{3}{2}}$$

If the pressure reached in the time τ_p' is sufficient to initiate ablation of the tissue, then $\varepsilon' = \varepsilon_{th}^{C \le 1}$, and

$$\varepsilon_{th}^{C>1} = C^{2/3} \cdot \varepsilon_{th}^{C \le 1} . \tag{2.20}$$

Despite the claimed success in explaining hard tissue ablation, the calculated results on the ablation energy density threshold in soft tissues remains questionable because the conditions of Oraevsky's experiment are not clearly given besides why and how the scattering factor is considered. In order to define the energy density using the corrected penetration depth given in Eq. (2.1), it assumed the light diffusion approximation. This assumption is only valid when the light incident into medium has been highly scattered even in the area close to the surface such as dense bone and calcified arterial plaque, contains about 20% collagen, 5% water, and 75% hydroxyapatite by mass [Izatt, Albagli 1991]. This gives a much higher scattering coefficient that satisfied the assumption. Similar arguments can be used to explain why the additional photomechanical models from the same group fail to describe soft tissue ablation [Albagli, Banish 1994; Albagli, Dark 1994; Itzkan, Albagli 1995].

The predicted values of threshold fluence for skin ablation based on the inertial confinement model are significantly different from the experimental results [Hu, Fang

2001], as shown in Table 2-1. Furthermore, the photomechanical model cannot be used to explain the probabilistic behavior of tissue ablation near the threshold that have been observed at wavelengths from 1064 to 213nm.

Table 2-1 Comparison of experimental and predicted values of laser fluence threshold for skin tissue ablation

	1064nm	532nm	266nm	213nm
Porcine skin – experimental (10%) [1,2]	41.8J/cm^2	18.9J/cm^2	5.36J/cm^2	0.711J/cm^2
Porcine skin – experimental (90%) [1,2]	129J/cm^2	35.8J/cm^2	14.3J/cm^2	1.6J/cm^2
Dermis μ_a(cm^{-1}) [2]	3.0	4.5	43	3400
Dermis μ_s(cm^{-1}) [2]	350	600	2000	2400
Dermis D(μm) [2]	540.7	339	56.5	26.9
Human skin – calculated [3]	108J/cm^2	6.78J/cm^2	1.13J/cm^2	0.538 J/cm^2

1. Calculated from the fluence determined by Hu et al. [Hu, Fang 2001] with pulse duration at 10 and 12ns.
2. *D* is calculated from Eq. (2.1) with μ_s and μ_a given by van Gemert *et al.* [van Gemert and Welch 1989; van Gemert, Lucassen 1996], where g is assumed to be 0.9;
3. Calculated from the predicted energy density *200J/cm^3* based on the photomechanical model.

2.3 The Photochemical Model

For soft tissue ablation with UV laser pulses, a photochemical model has been proposed to explain the ablation process [Srinivasan 1986; Srinivasan, Braren 1986; Ojamae, Tegenfeldt 1992; Pettit and Sauerbrey 1993]. In the photochemical model, the laser energy absorbed by tissue molecules excites electrons in proteins or other biopolymers to the states lying above the dissociation and ionization limits of these

molecules. The direct dissociation of molecular bonds, or the mediated dissociation through reactions with ions or radicals formed from the highly excited electronic states, lead to the splitting of long polymer chains into short fragments. The numerous bond breakings cause pressure to rise substantially inside the irradiated tissue volume and push the molecular fragments away from the tissue. To reach the threshold of ablation photon energy, $h\omega$, ranging from 6 to 8eV, is required to dissociation molecules, which corresponds to the UV region of the laser radiation spectrum. Therefore, any appreciable quantum yields of photochemical reactions in proteins and other biopolymers can only be expected at irradiation wavelengths shorter than 250nm [Oraevsky, Esenaliev 1992].

The typical laser irradiance threshold range predicted by photochemical model is around $10^7 W/cm^2$ [Pettit and Sauerbrey 1993]. Investigations of the molecular products of UV laser etching suggest that photochemical substrate decomposition plays a significant role. Several important features of UV ablation are summarized as [Pettit and Sauerbrey 1993]: a threshold fluence that mainly depends on the target absorption coefficient at the wavelength; below the threshold, the temperature increase due to absorption is directly proportional to the laser fluence, while above the threshold the rate of the rise in temperature is significant slower;

Quantitative studies on UV ablation of PMMA polymers [Srinivasan 1986; Srinivasan, Braren 1986] found that although the threshold fluence value is not sharply defined, the ablation depth d can be derived as a function of laser fluence Φ without explicit assumption about the nature of the decomposition process:

$$d = \frac{1}{\mu_\alpha} \log \frac{\Phi}{\Phi_{th}}. \tag{2.21}$$

There is an obvious disagreement between the UV absorption coefficient μ_α found from the slopes of the d vs. logΦ plots and the value obtained from the absorbance measurements. This disagreement was explained by both the absorption coefficient change due to successive pulses and change occurs within a single pulse duration [Pettit and Sauerbrey 1993].

2.4 Plasma-Mediate Model

During pulsed laser ablation of biological tissues, when the short pulse and tight focus setup has been implemented, the strong electromagnetic field of the laser pulse can ionize the bound electrons inside tissue and form localized plasma that strongly absorbs the incident laser energy. The plasma radiates and, after the laser pulse, its energy decays into shock waves and acoustic transients. A plasma-mediated model has been proposed in the early 1980s to interpret the tissue ablation as a result of plasma formation [Fujimoto, Lin 1985].

Laser-induced plasma has been intensively studied in the optical breakdown of condensed matters, as reviewed by Bloembergen [Bloembergen 1974], Demichelis [DeMichelis 1969], and Shen [Shen 1984]. The occurrence of plasma in the ocular tissue ablated by nanosecond pulses in the visible and near-infrared regions has been widely accepted because the tissues are nearly transparent and the photothermal pathway is not a valid possibility [Fujimoto, Lin 1985; Docchio, Sacchi 1986; Stern, Schoenlein 1989;

Kennedy 1995; Kennedy, Boppart 1995; Vogel, Nahen 1996]. Very little considerations have been given to the cases of soft tissue ablation by the short UV laser pulses because of concurrence of both the strong electromagnetic field of the pulse and significant tissue ablation. Hu *et al.* have used the plasma model to explain the corneal tissue ablation by UV picosecond laser pulses at 263 and 211nm [Hu and Juhasz 1996]. However, the characteristics of the plasma-mediated ablation model need to be further elucidated to account for significant tissue absorption.

A rate equation approach was used as a framework to consider plasma formation and optical breakdown in solids [Bloembergen 1974; Shen 1984]. It has been adopted for studying the optical breakdown in ocular tissue and water with an added multiphoton ionization term [Kennedy 1995]. Plasma is a state of matter with highly concentrated charged species as a result of ionization of the atoms and molecules in medium. The rate equation describes the free electron density ρ(t) as a function of time within the illuminated volume of tissue [Kennedy 1995]:

$$\frac{\partial \rho(t)}{\partial t} = \eta \rho(t) + (\frac{\partial \rho(t)}{\partial t})_m - g\rho(t)\,, \tag{2.22}$$

where η is the cascade ionization rate for free electrons to ionize bound electrons through collisions and g is the rate of free electron loss through recombination, trapping, and diffusion out of the illuminated volume. The three terms on the right-hand side of Eq. (2.22) represent contributions from cascade ionization, multiphoton ionization, and the electron loss, respectively.

For nanosecond pulses, the cascade ionization dominates over the multiphoton pathway when enough seed electrons are present because of the relatively low peak irradiance in comparison with the multiphoton ionization dominance for picoseconds and femtoseconds pulses. Hence, one can assume the multiphoton ionization rate as a constant b and Eq. (2.22) takes the simple form of a linear differential equation

$$\frac{\partial \rho(t)}{\partial t} - a\rho(t) = b\,, \tag{2.23}$$

where

$$\begin{aligned} a &= \eta - g \\ b &= \left(\frac{\partial \rho}{\partial t}\right)_m \end{aligned}\,. \tag{2.24}$$

Subject to the initial condition, $\rho(0) = \rho_0$, Eq. (2.23) can be solved as

$$\rho(t) = \rho_0 e^{at} + \frac{b}{a}(e^{at} - 1)\,. \tag{2.25}$$

The optical breakdown is assumed to occur when the free electron density reaches a critical value of $\rho_{cr} \approx 10^{20}/\text{cm}^3$ [Kennedy 1995]. With the single-pulse condition, the irradiance threshold is defined to be the minimum irradiance that creates ρ_{cr} given an initial free electron density ρ_0 within the pulse duration τ_0.

2.4.1 Multiphoton Ionization

The multiphoton term can be written as

$$(\frac{\partial \rho(t)}{\partial t})_m = \eta_m \rho_b(t)\,, \tag{2.26}$$

where η_m is the multiphoton ionization rate and $\rho_b(t)$ is the density of bound electrons with a binding energy E_{ion} at time t given by

$$\rho_b(t) = n\rho_{mol} - \rho(t)\,. \tag{2.27}$$

Here n is the number of electrons per molecule in the tissue medium with a binding energy E_{ion} and ρ_{mol} is the molecular density. In condensed matters, $\rho_{mol} \cong 10^{22}$~$10^{23}/cm^3$ and thus the last term in Eq. (2.27) can be neglect since only cases when $\rho(t) \sim \rho_{cr} \approx 10^{20}/cm^3$ are considered [Kennedy 1995]. This provides

$$(\frac{\partial \rho}{\partial t})_m \cong \eta_m \cdot n \cdot \rho_{mol} \approx \text{constant} \tag{2.28}$$

To calculate the rate η_m, the probability P_m of multiphoton ionization is needed:

$$\eta_m = \frac{P_m}{\rho_b}, \tag{2.29}$$

where the Keldysh's expression has been used for [Keldysh 1965]

$$P_m = \left(\frac{2}{9\pi}\right)\omega\left(\frac{m'\omega}{\hbar}\right)^{\frac{3}{2}} e^{2K(1-\frac{1}{4\gamma^2})}\Phi(z)(\frac{1}{16\gamma^2})^K\,. \tag{2.30}$$

In Eq. (2.30), $\Phi(z)$ is a numerical factor given by the Dawson's integral:

$$\Phi(z) = e^{-z^2}\int_0^z e^{y^2}dy = e^{-z^2}\sum_{n=0}^{\infty}\frac{z^{2n+1}}{n!(2n+1)}, \tag{2.31}$$

where

$$z = \sqrt{2K - \frac{2\Delta'}{\hbar\omega}}\,. \tag{2.32}$$

where Δ' is the ionization energy; K is an integer for the minimum number of photons required to ionize a molecule

$$K = \mathrm{mod}(\Delta'/\hbar\omega) + 1. \tag{2.33}$$

where mod means modulus value. An effective ionization energy in the electric field $\mathcal{E}$ of the laser pulse is defined as

$$\Delta' = \Delta + \frac{e^2\mathcal{E}_2}{4m'\omega^2} = \Delta\left(1 + \frac{1}{4\gamma^2}\right), \tag{2.34}$$

in which m′ represents the exciton reduced mass:

$$\frac{1}{m'} = \frac{1}{m_e} + \frac{1}{m_h}, \tag{2.35}$$

where $m_h \approx m_e$ is assumed. The ratio γ of the optical frequency ω to the tunneling frequency ω_t is define as:

$$\gamma = \frac{\omega}{\omega_t} = \frac{\omega\ \sqrt{m'\Delta}}{e\mathcal{E}}. \tag{2.36}$$

The tunneling effect is the case that one electron is extracted from the atom by a static or low frequency electric field. The tunneling time is determined by the mean free time of the electron passing through a barrier of width $l_{ion}=\Delta/e\mathcal{E}$. The average electron velocity v_e is of the order of $(\Delta/2m_e)^{1/2}$. Therefore, the tunneling frequency is on the order of

$$\omega_t = \frac{v_e}{l_{ion}} = \frac{e\cdot\mathcal{E}}{\Delta}\cdot\sqrt{\frac{\Delta}{2m_e}} = \frac{e\cdot\mathcal{E}}{\sqrt{2m_e\cdot\Delta}}. \tag{2.37}$$

Keldysh has shown that the multiphoton ionization effects share a common nature, and are limiting cases of a single process in which one electron goes from a bound state in the atom into a free state under the influence of an alternating electromagnetic field. The tunneling effect is in the limit of low frequencies and the multiphoton effect is in the limit of high frequencies [DeMichelis 1969]. Using the limiting condition for laser electromagnetic field, where $\gamma \gg 1$ (in the order of $10^{2\sim5}$):

$$1 \pm \frac{1}{4\gamma^2} \approx 1, \tag{2.38}$$

$$\Delta' \approx \Delta, \tag{2.39}$$

Combine Eqs. (2.29), (2.31), and (2.36) to (2.39), the multiphoton ionization rate is found to be:

$$\eta_m = \frac{P_m}{\rho_b} = \left(\frac{2}{9\pi}\right)\frac{\omega}{\rho_b}\left(\frac{m'\omega}{\hbar}\right)^{\frac{3}{2}} e^{2K}\Phi(z)\left(\frac{1}{16}\right)^K \left(\frac{e^2 I_0}{m'\Delta \;\; \omega^2 c\varepsilon_0 n_0}\right)^K. \tag{2.40}$$

2.4.2 Cascade Ionization Rate and Electron Loss Rate

The collision or cascade ionization process is a process in which free electrons gain energy from the electric field of a laser pulse through the inverse bremsstrahlung [Bloembergen 1974]. Two conditions must be met for the process to start: the strong laser field and the availability of initial free electrons or the seed electrons. For biological tissues with significant light absorption, it has been proposed that the initial seed electrons be provided through the pre-existing free electrons, multiphoton ionization, and ionization due to the thermal fluctuation in the media at the ambient temperature [Kennedy 1995]. To distinguish the thermal ionization defined by Kennedy

from the thermal ionization considered in the new plasma model, to be described in next chapter, the former will be define as extended thermal ionization and the latter as the localized thermal ionization. In fact, Kennedy neglected the extended thermal ionization as a mechanism in creating seed electrons in his modeling of breakdown [Kennedy 1995].

To initiate cascade ionization, a minimum of one free electron is required in the illuminated region whose volume is V_0. Therefore, the requirement of the initial free electron density ρ_0 can be expressed as:

$$\rho_0 \geq \rho_0(\min). \tag{2.41}$$

where $\rho_0(\min)= 1/V_0$. In the absence of the pre-existing free electrons, the cascade ionization threshold may be delayed and some times larger than that of multiphoton ionization to generate seed electrons. In the latter case, the optical breakdown threshold is therefore determined by the irradiance for multiphoton ionization to initiate cascade ionization [Kennedy 1995].

The electron gains energy in an electric field of frequency ω and rms filed strength $\mathcal{E}$.

The average rate of energy gain of one electron from an ensemble is given by [DeMichelis 1969]

$$\frac{dE}{dt} = \frac{e^2 \boldsymbol{\mathcal{E}}^2 \nu}{m\omega^2} \frac{\omega^2}{\omega^2 + \nu^2}, \tag{2.42}$$

where m is the electron mass and the effective collision frequency can be expressed as

$$\nu = n_a v_e \sigma_{tr}. \tag{2.43}$$

Here n_a is the atomic (or molecular) density, v_e is the electron velocity and σ_{tr} is the electron transport cross section. Similarly, energy loss from elastic collisions can be found as [DeMichelis 1969]:

$$\frac{dE}{dt} = - \frac{2mE_{av}\nu}{M}\frac{\omega^2}{\omega^2+\nu^2}, \tag{2.44}$$

where E_{av} is the average electron energy and M is the atomic (or molecular) mass. The mean free time between collisions electron-ion is:

$$\tau = \frac{1}{\nu}. \tag{2.45}$$

Combining Eqs. (2.42) and (2.44), the energy of the average electron changes at the rate:

$$\frac{d\varepsilon}{dt} = \left[\frac{e^2\mathcal{E}^2}{m} - \frac{2m\varepsilon_{av}\omega^2}{M}\right]\frac{\tau}{\omega^2\tau^2+1} \tag{2.46}$$

It is assumed that any electron, whose kinetic energy reaches the ionization energy, E_{ion}, will shortly produce a new free electron. Thus,

$$\eta = \frac{dE/dt}{E_{ion}} = \left[\frac{e^2\mathcal{E}^2}{m} - \frac{2m\varepsilon_{av}\omega^2}{M}\right]\frac{\tau}{(\omega^2\tau^2+1)E_{ion}} \tag{2.47}$$

The peak irradiance I_0(W/m^2) is related to the rms field $\mathcal{E}$(V/m) by

$$\mathcal{E}^2 = \frac{I_0}{cn_o\varepsilon_0}, \tag{2.48}$$

where n_0 is the refraction index of the medium.

Eq. (2.47) now becomes

$$\eta = \left[\frac{e^2 I_0}{m} - \frac{2m\varepsilon_{av}\omega^2}{M} \right] \frac{\tau}{(\omega^2\tau^2 + 1)E_{ion}} . \tag{2.49}$$

The loss of high-energy electrons proceeds at a rate, g, because of recombination, trapping, and diffusion [Kennedy 1995]. The lifetime of quasi-free electrons is assumed longer than the nanosecond laser pulses especially when the electron is absorbing energy from an intense optical field. Electron recombination during the breakdown process will therefore be neglected. Although trapping in localized potential wells or solvent states is well known in water, the binding energy of these states are low (~1.5±0.5eV) that they can be very easily re-ionized. In the first order model, Kennedy consequently assumed the solvation and desolvation do not significantly affect the breakdown process near the thresholds. The loss rate g is thus the rate of diffusion out of the focal volume with recombination and trapping neglected for nanosecond pulse ablations [Kennedy 1995]:

$$g = \frac{D_e}{\Lambda^2}, \tag{2.50}$$

where D_e is the electron diffusion coefficient, and Λ is the characteristic diffusion length:

$$D_e = \frac{2\varepsilon_{av}}{3m\nu}, \tag{2.51}$$

$$\frac{1}{\Lambda^2} = \left(\frac{4.8}{d}\right)^2 + \left(\frac{1}{l}\right)^2 \tag{2.52}$$

where l and d are the length and diameter of the focal volume, respectively. Assuming Gaussian beam of wavelength λ, the focal volume is approximately a cylinder of radius r_0 and length l with r_0 as the waist radius and l the Rayleigh range, z_R, so

$$d = 2r_0 \tag{2.53}$$

$$l = z_R = \frac{\pi r_o^{\,2}}{\lambda}. \tag{2.54}$$

$$V_0 = l\pi r_0^{\,2}. \tag{2.55}$$

Moreover, the electron loss rate g can be expressed as

$$g = \frac{D_e}{\Lambda^2} = \left(\frac{2\varepsilon_{av}}{3m\nu}\right)\left[(\frac{4.8}{d})^2 + (\frac{1}{l})^2\right] = \left(\frac{2\varepsilon_{av}\tau}{3m}\right)\left[\left(\frac{4.8}{2r_0}\right)^2 + \left(\frac{\lambda}{\pi r_o^{\,2}}\right)^2\right]. \tag{2.56}$$

2.5 Microscopic model of the cascade ionization process

The microscopic process of the cascade ionization has been studied by B. K. Ridley, who proposed a lucky drift concept describing how electrons exchange energy through collisions with ions and atoms, and interacting with external fields [Ridley 1983]. Based on the relaxation time approximation, this approach separates the electron collisions into momentum relaxation process and energy relaxation process. Two basic assumptions of this approximation on the electrons' distribution function after a collision are [Ashcroft and Mermin 1976]: first, it is independent of any non-equilibrium distribution function just prior to the collision; second, collisions will not alter its form if the electrons in a region have the equilibrium distribution appropriate to a local temperature.

The cascade ionization of electrons in a strong electric field can be divided into three processes according to their different time scales: ballistic motion without a collision within a momentum relaxing time constant $\tau_m(E)$, lucky drift followed by a momentum-relaxing collision without energy exchange within an energy-relaxing time constant $\tau_E(E)$, and energy relaxation to reach equilibrium.

$$\begin{array}{ll} 0 \le t \le \tau_m(E) & ballistic\ motion \\ \tau_m(E) \le t \le \tau_E(E) & lucky\ drift \\ \tau_E(E) \le t & to\ equilibrium \end{array} . \qquad (2.57)$$

Consequently, there are three possible ways for an electron to gain energy to reach ionization energy E_{ion} from its initial value: directly through acceleration by the optical field in a ballistic motion without collision; directly in a lucky drift through a momentum-relaxing collision without losing energy; or increasing its initial energy to an energy $E \le E_{ion}$ through ballistic motion and then up to E_{ion} through lucky drift.

For the ballistic motion, the momentum change relates to the external electric field $\mathcal{E}$.

For a carrier of effective mass $m^*(E)$ drifting with velocity $v_d(E)$ the equation of motion is given:

$$\frac{d}{dt}(m*(E)v_d(E)) \approx \hbar \frac{dk(E)}{dt} = e\mathcal{E} . \qquad (2.58)$$

At the end of the ballistic motion, $t=\tau_m$, the carrier reaches the drift velocity, which can be obtained by integrating Eq. (2.58):

$$v_d(E) = \frac{e\mathcal{E}\tau_m(E)}{m^*(E)} . \qquad (2.59)$$

When a steady state is achieved around $t \sim \tau_m$, the average carrier has a drift velocity given by

$$v_d(E_{av}) = \frac{e\mathcal{E}\tau_m(E_{av})}{m^*(E_{av})} . \qquad (2.60)$$

For a hot carrier, the energy relaxation can be described by the relaxation time approximation

$$\frac{dE}{dt} \approx e\mathcal{E}v_d(E) - \frac{E}{\tau_E(E)} \qquad E >> k_B T \,. \tag{2.61}$$

Since there is no significant energy relaxing during lucky drift, the last term in Eq. (2.61) can be dropped and the energy variation can be found by combining Eqs. (2.59) and (2.61):

$$\frac{dE}{dt} \approx \frac{e^2 \mathcal{E}^2 \tau_m(E)}{m^*(E)}. \tag{2.62}$$

Integrating Eq. (2.62), the average energy of an electron at the end of lucky drift, $t \sim \tau_E$ can be found as:

$$E_{av} = \frac{e^2 \mathcal{E}^2 \tau_m(E_{av}) \tau_E(E_{av})}{m^*(E_{av})}. \tag{2.63}$$

Since neither ballistic motion nor lucky drift loses energy, the mean path length for the carrier to achieve threshold energy E_{ion} is $E_{ion}/e\mathcal{E}$. If the probability for an electron avoiding energy loss over such a length is given by $P(\mathcal{E}, E_{ion})$, the ionization rate per unit of length α can be defined as:

$$\alpha = \frac{e\mathcal{E}}{E_{ion}} P(\mathcal{E}, E_{ion}). \tag{2.64}$$

The probability of an electron undergoing a collision in any infinitesimal time interval length dt is dt/τ in which the time τ is variously known as the relaxation time, the collision time, or the mean free time. It follows that an average electron travels for a time

τ before its next collision and have been travel for a time τ since its last collision. If the probability for an electron moving from time t' to t without suffering a collision is defined as P(t, t'):

$$P(t,t'+dt') = P(t,t')\left[1-\frac{dt}{\tau(t')}\right], \tag{2.65}$$

and

$$\frac{P(t,t')-P(t,t'+dt')}{dt} = \frac{P(t,t')}{\tau(t')}. \tag{2.66}$$

In the limit as dt'$\rightarrow$ 0, this gives:

$$\frac{\partial}{\partial t}P(t,t') = -\frac{P(t,t')}{\tau(t')}. \tag{2.67}$$

Hence the probability for an electron avoiding a collision between 0 and *t* is:

$$P_0(t) = \exp\left[-\int_0^t \frac{dt}{\tau(E)}\right]. \tag{2.68}$$

In order to define probabilities using this model, the collision has been treated to have only two categories: one type of collisions which totally relax momentum but does not relax energy with collision time $\tau_m(E)$; and the other which totally relax energy only with collision time $\tau_E(E)$.

As mentioned earlier, there are three possible ways for an electron to gain energy to reach the threshold energy E_{ion}. Correspondingly, using the relationship obtained in Eq. (2.62), the probability for an electron to reach E_{ion} without any collision within $\tau_m(E)$ is found as

$$P_1(\mathcal{E}, E_{ion}) = \exp\left[-\int_0^t \frac{dt}{\tau_m(E)}\right] = \exp\left[-\int_0^{E_{ion}} \frac{dE}{e\mathcal{E}\, v_d(E)\tau_m(E)}\right]. \quad (2.69)$$

Introducing a momentum-relaxing mean free path λ(E),

$$\lambda(E) = v_d(E)\,\tau_m(E). \quad (2.70)$$

and

$$P_1(\mathcal{E}, E_{ion}) = \exp\left[-\int_0^{E_{ion}} \frac{dE}{e\mathcal{E}\,\lambda(E)}\right]. \quad (2.71)$$

It is assumed that once an electron suffers a momentum-relaxing collision, it finds itself in the drift mode. Similarly, through Eq. (2.62) the probability of an electron drifting for a time t and avoiding significant energy relaxation is given by

$$P_2(\mathcal{E}, E_{ion}) = \exp\left[-\int_0^{E_{ion}} \frac{m^*(E)\,dE}{e^2\mathcal{E}^2\,\tau_m(E)\tau_E(E)}\right]. \quad (2.72)$$

The third case is that an electron starting from zero energy moves ballistically up to energy E, and then up to E_{ion} via lucky drift after a collision. The probability for it to reach E in time t without collision is $P_1(\mathcal{E}, t)$ and the probability of a collision in the time interval dt is $dt/\tau_m(E)$. Thus the probability of a first collision in the time interval dt after t is just $P_1(\mathcal{E}, E)dt/\tau_m(E)$ after converting dt to dE using Eq. (2.62). This first collision, according to the assumption, marks the transition from the ballistic motion to lucky drift mode. The probability of lucky drift to E_{ion} from E is $P_{21}(\mathcal{E}, E, E_{ion})$, which is obtained from Eq. (2.72):

$$P_{21}(\mathcal{E}, E, E_{ion}) = \exp\left[-\int_{E}^{E_{ion}} \frac{m^*(E)\,dE}{e^2\,\mathcal{E}^2\,\tau_m(E)\tau_E(E)} \right]. \tag{2.73}$$

Thus the total probability of lucky drift from zero energy to E_{ion} is:

$$P_2(\mathcal{E}, E_{ion}) = \int_0^{E_{ion}} P_1(\mathcal{E}, E_{ion}) P_{21}(\mathcal{E}, E, E_{ion}) \frac{dE}{e\mathcal{E}\,\lambda(E)}. \tag{2.74}$$

Thus the probability for an electron's energy to increase to E_{ion} can be summarized as

$$P(\mathcal{E}, E_{ion}) = P_1(\mathcal{E}, E_{ion}) + P_2(\mathcal{E}, E_{ion}). \tag{2.75}$$

Besides the contribution of lucky drift from zero energy electrons, it is also necessary to consider the contribution of lucky drift from electrons been thermalized into hot electron distribution where they have a non-zero kinetic energy. For low electric field, the mean free path $E_{ion}/e\mathcal{E}$ is long that the vast majority of the electrons will therefore be thermalized and their contribution must not be neglected, which means changing the lower integration limit in Eqs. (2.71) to (2.75) from zero to E_{av} obtained from Eq. (2.63).

For high fields, the mean free path is short and the finite time need to be taken into account, or equivalently, length required an average energy to be established. An absolute cut-off distance is assumed to be three mean free paths by Ridley, which means that no hot-electron thermalization occurs when

$$\frac{E_{ion}}{e\mathcal{E}} < 3\lambda_{av}, \tag{2.76}$$

where λ_{av} is some average mean free path. If $(v_d\tau_E)_{av}$ is the average energy-relaxation drift length, the probability for thermalization to occur is:

$$P_T = 1 - \exp\left(-\frac{\left(E_{ion}/e\mathcal{E}\right) - 3\lambda_{av}}{\left(v_D \tau_E\right)_{av}} \right). \tag{2.77}$$

Thus the final expression for the ionization coefficient is:

$$\alpha = \frac{e\mathcal{E}}{E_{ion}} \left[P_1(\mathcal{E}, E_{ion}) + P_2(\mathcal{E}, E_{ion}) + P_T \left(P_1^T(\mathcal{E}, E_{ion}) + P_2^T(\mathcal{E}, E_{ion}) \right) \right]. \tag{2.78}$$

Assuming the dominance of high-energy ions scattering, a simple relation between momentum and energy relaxation times can be derived. If the phonons are in thermodynamic equilibrium, the scattering rate is proportional to $2n(\omega_p)+1$, where $n(\omega_p)$ is the Bose-Einstein number. Since only a fraction $1/(2\, n(\omega_p)+1)$ results in the net energy loss of $\hbar\omega_p$ and the scattering rate and momentum-relaxation rate are nearly identical, in the case of deformation-potential scattering, the energy-relaxation rate can be written as follows:

$$\left(\frac{dE}{dt}\right)_{optical\ phonon} = -\frac{1}{2n(\omega_p)+1} \frac{\hbar\omega_p}{\tau_m(E)}. \tag{2.79}$$

Integrate Eq. (2.79),

$$E = \frac{1}{2n(\omega_p)+1} \frac{\tau_m(E) \cdot \hbar\omega_p}{\tau_m(E)}. \tag{2.80}$$

Hence:

$$\frac{\tau_E(E)}{\tau_m(E)} = \frac{2n(\omega_p)+1}{\hbar\omega_p} E = \frac{2n(\omega_p)+1}{\hbar\omega_p / E_{ion}} \frac{E}{E_{ion}} = \frac{E}{rE_{ion}}, \tag{2.81}$$

where the factor r is introduced as the ratio of the effective energy loss per collision to E_{ion}:

$$r = \frac{\hbar\omega_p / E_{ion}}{2n(\omega_p)+1}. \tag{2.82}$$

If the mean free path λ(E) is independent of energy E,

$$\begin{aligned} E &= \frac{1}{2}m^*(E)\cdot v_d^2(E) = \frac{1}{2}m^*(E)\cdot\left(\frac{\lambda}{\tau_m(E)}\right)^2 \\ \frac{2E}{\lambda^2}\cdot\tau_m(E) &= \frac{m^*(E)}{\tau_m(E)} \\ \frac{2E}{\lambda^2}\cdot\frac{\tau_m(E)}{\tau_E(E)} &= \frac{m^*(E)}{\tau_E(E)\cdot\tau_m(E)} \end{aligned}. \tag{2.83}$$

Using Eq. (2.81),

$$\begin{aligned} \frac{m^*(E)}{\tau_E(E)\cdot\tau_m(E)} &= \frac{2E}{\lambda^2}\cdot\frac{\tau_m(E)}{\tau_E(E)} = \frac{2E}{\lambda^2}\cdot\frac{rE}{E} \\ \frac{m^*(E)}{\tau_E(E)\cdot\tau_m(E)} &= \frac{2rE_{ion}}{\lambda^2} \end{aligned}. \tag{2.84}$$

The first term in Eq. (2.78) is $P_1(\mathcal{E}, t)$. From Eq. (2.71),

$$P_1(\mathcal{E}, E_{ion}) = \exp\left[-\int_0^{E_{ion}}\frac{dE}{e\mathcal{E}\,\lambda(E)}\right] = \exp\left(-\frac{E_{ion}}{e\mathcal{E}\,\lambda}\right) = e^{-x}, \tag{2.85}$$

where

$$x = \frac{E_{ion}}{e\mathcal{E}\lambda}. \tag{2.86}$$

The second term in Eq. (2.78) is $P_2(\mathcal{E}, t)$. From Eqs. (2.73) and (2.84),

$$P_2(\mathcal{E},E,E_{ion}) = \exp\left[-\int_E^{E_{ion}} \frac{m^*(E)dE}{e^2\mathcal{E}^2\tau_m(E)\tau_E(E)}\right] = \exp\left[-\int_E^{E_{ion}} \frac{2rEdE}{e^2\mathcal{E}^2\lambda^2}\right]$$
$$= \exp\left[-\frac{2rE_{ion}E}{e^2\mathcal{E}^2\lambda^2}\right]_E^{E_{ion}} = \exp\left[-\frac{2rE_{ion}^2}{e^2\mathcal{E}^2\lambda^2}+\frac{2rE_{ion}E}{e^2\mathcal{E}^2\lambda^2}\right] \quad .$$
$$= e^{-2rx^2}\cdot e^{2rx^2\frac{E}{E_1}}$$

From (2.72) and (2.74),

$$P_2(\mathcal{E},E_{ion}) = \int_0^{E_{ion}} P_1(\mathcal{E},E_{ion})P_2(\mathcal{E},E,E_{ion})\frac{dE}{e\mathcal{E}\lambda(E)}$$
$$= \int_0^{E_{ion}} \left(e^{-\frac{E}{e\mathcal{E}\lambda}}\right)\cdot\left(e^{-2rx^2}\cdot e^{2rx^2\frac{E}{E_{ion}}}\right)\frac{E_{ion}}{e\mathcal{E}\lambda E_{ion}}dE$$
$$= \int_0^{E_{ion}} e^{-x\frac{E}{E_{ion}}}\cdot e^{-2rx^2}\cdot e^{2rx^2\frac{E}{E_{ion}}}\frac{x}{E_{ion}}dE \quad . \qquad (2.87)$$
$$= e^{-2rx^2}\cdot x\int_0^{E_{ion}} e^{\left(2rx^2-x\right)\frac{E}{E_{ion}}}d\frac{E}{E_{ion}}$$
$$= \frac{e^{-2rx^2}}{2rx-1}\left(e^{\left(2rx^2-x\right)}-1\right) = \frac{e^{-2rx^2}-e^{-x}}{1-2rx}$$

Now it is necessary to calculate the contribution of hot electrons. From (2.77), (2.60), and (2.84),

$$P_T = 1-\exp\left(-\frac{\left(E_{ion}/e\mathcal{E}\right)-3\lambda_{av}}{\left(v_d\tau_E\right)_{av}}\right)$$
$$= 1-\exp\left(-\frac{x\lambda-3\lambda}{e\mathcal{E}\tau_m(E)\tau_m(E)/m^*(E)}\right) = 1-\exp\left(-\frac{x\lambda-3\lambda}{\lambda/2rx}\right). \qquad (2.88)$$
$$= 1-\exp\left(-2rx^2-6rx\right) = 1-e^{-2rx(x-3)}$$

Hence from (2.77), (2.63), and (2.84), the thermalized electron energy is given by

$$E_T = E_{av}P_T = \left[\frac{e^2\,\mathcal{E}^2\,\tau_m(E_{av})\,\tau_E(E_{av})}{m^*(E_{av})}\right]\cdot P_T$$
$$= \left[e^2\,\mathcal{E}^2\,\frac{\lambda^2}{2rE_{ion}}\right]\cdot P_T = \left[e^2\,\mathcal{E}^2\,\frac{E_{ion}\lambda^2}{2rE_{ion}^2}\right]\cdot P_T\,. \tag{2.89}$$
$$\frac{E_T}{E_1} = \frac{P_T}{2rx^2} = \zeta$$

From (2.71),

$$P_1^T(\mathcal{E}, E_{ion}) = \exp\left[-\int_{E_T}^{E_{ion}}\frac{dE}{e\mathcal{E}\,\lambda(E)}\right] = \exp\left[-\frac{E_{ion}-E_T}{e\mathcal{E}\,\lambda}\right], \tag{2.90}$$
$$= \exp\left(-x+\zeta x\right) = e^{-x(1-\zeta)}$$

From (2.73) and (2.74),

$$P_2^T(\mathcal{E}, E_{ion}) = \int_{E_T}^{E_{ion}} P_1^T(\mathcal{E}, E_{ion})P_2^T(\mathcal{E}, E, E_{ion})\frac{dE}{e\mathcal{E}\,\lambda}$$
$$= \int_{E_T}^{E_{ion}}\left[e^{-x(1-\zeta)E/E_{ion}}\right]\cdot\left[e^{-2rx^2+2rxE/E_{ion}}\right]\frac{xdE}{E_{ion}}. \tag{2.91}$$
$$= \frac{e^{-2rx^2(1-\zeta)}\cdot e^{-x(1-\zeta)}}{1-2rx}$$

Finally, the ionization coefficient is given by:

$$\alpha = \frac{1}{x\lambda}\left\{e^{-x} + \left(\frac{e^{-2rx^2}-e^{-x}}{1-2rx}\right) + P_T\left[e^{-x(1-\zeta)} + \frac{e^{-2rx^2(1-\zeta)}-e^{-x(1-\zeta)}}{1-2rx}\right]\right\}. \tag{2.92}$$

In Eq. (2.92), the terms with exp(-x) represent the contribution from the ballistic mode, while the terms with exp(-x^2) are for lucky drift mode. At low field, i.e. $\mathcal{E}$ is small and x is large, the drift is slow hence the emphasis is on electrons that avoid momentum relaxation during the relatively long mean free time. Consequently, the exp(-x) terms exceed the exp(-x^2) terms and the Shockley-like lucky-ballistic mode P~exp(-K/$\mathcal{E}$)

dominates the ionization process. On the contrary, at high field, i.e. $\mathcal{E}$ is large and x is small, the electrons move much faster and there is more chance for them undergoes loss-free collision per unit time. As a result, the $\exp(-x^2)$ terms dominate in Eq. (2.92), which corresponds the domination of the lucky-drift mode $P \sim \exp(-K/\mathcal{E}^2)$ in this region.

Chapter 2 Figures

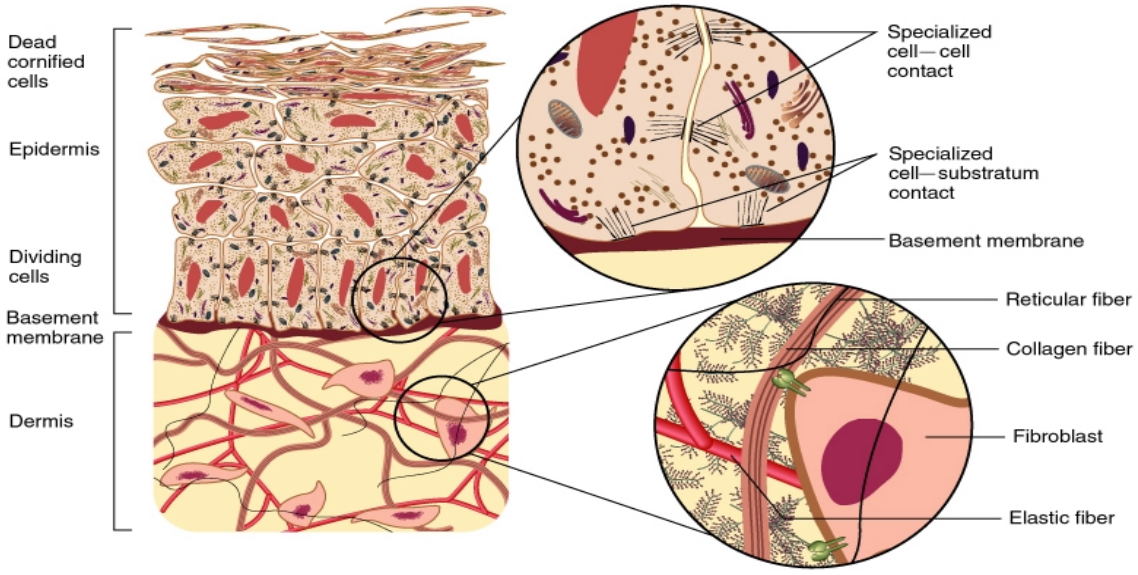

Figure 2-1 Diagrammatic cross section of human skin [Du, Hu 2001].

Chapter 3 Theoretical Modeling

The existing plasma model [Docchio, Sacchi 1986; Sacchi 1991; Kennedy, Boppart 1995; Vogel, Nahen 1996] has been quantitatively validated for providing correct predictions on the optical breakdown thresholds by short laser pulses from visible to near infrared wavelength in transparent media such as water and a variety of ocular tissues. For ablation of skin tissues by nanosecond laser pulses in a wide spectrum from ultraviolet to near infrared, however, the tissue absorption has to be considered. In this chapter, a modified rate equation will be proposed to develop a framework for a unified model of plasma-mediated ablation. A new term will be introduced in the rate equation, which takes into account of important pathway of localized thermal ionization due to tissue absorption, in addition to cascade and multiphoton ionization pathways discussed in Chapter 2. The rest of the chapter will be devoted for solving the modified rate equation.

3.1 Modified Rate Equation

In contrast to condensed matter, which was investigated previously in optical breakdown studies [Bloembergen 1974; Kennedy 1995; Kennedy, Boppart 1995], skin tissues have very complex and microscopically heterogeneous structures, which include keratinocytes, melanocytes and pigment granules in the epidermis, fibroblasts, elastin and interlacing collagen fibers in the dermis. First, the absorption of radiation by the macromolecules in the skin tissues is significant in the ultraviolet region, electronic in origin, and of broadband resonance in nature. Therefore, a monotonic increase in tissue

absorption as the wavelength of laser radiation decreases is expected and consequently no abrupt changes in the tissue ablation threshold is expected since it is a continuous function of the tissue absorption coefficient. Secondly, the degree of disorder in skin tissues is much larger than that of water, cornea, and other transparent ocular humors, therefore it introduces different characteristics of the optical breakdown in the skin in addition to light absorption. For instance, light scattering cannot be ignored when light penetration into the skin bulk in comparison with absorption is considered. In fact, scattering dominates absorption in most of the spectral regions from 200nm to 1500nm and light diffusion theory becomes a valid model [Welch and Gemert 1995]. By the same argument, the free electrons are expected to be highly localized on the spatial scales comparable with the light wavelength and therefore the loss of free electrons due to diffusion in the last term of the rate equation (2.21) can be neglected over the short time scales of nanoseconds.

Skin tissue ablation mechanism has been investigated using ablation probability data through probit analysis and discussed in light of a plasma-mediated ablation model [Hu, Fang 2001]. It has also been shown that the probability breakdown threshold has a strong dependence on laser wavelength, and thus on tissue absorption, which cannot be explained by the existing plasma model studied in water [Vogel, Nahen 1996] and ocular tissue [Kennedy 1995; Kennedy, Boppart 1995]. Therefore, a commonly neglected ionization pathway through laser-induced and localized thermal ionization as a consequence of tissue absorption needs to be considered in the process of seed electron generation. The ionization of the atoms or molecules in a region of high temperature at

local thermal equilibrium is defined as laser-induced and localized thermal ionization and discussed in details in this chapter. The existing plasma model has only been studied in transparent media where heterogeneity is not significant. As a result, thermal ionization was only considered in room temperature conditions, where its role of providing seed electrons before the laser pulse can be neglected [Nasser 1971]. Under certain circumstances, i.e. in cases of localized absorption and confined thermal energy, a very high temperature may be achieved such that the localized thermal ionization pathway may not be excluded.

Consequently, a modified rate equation was proposed to take into account the contribution of localized thermal ionization due to transient rise in the temperature of the chromophores as a result of the absorption of laser pulse energy. The rate of increase in the free electron density ρ(t) within the illuminated volume of tissue can be described in general by

$$\frac{\partial \rho(t)}{\partial t} = \eta \rho(t) + (\frac{\partial \rho(t)}{\partial t})_{th} + (\frac{\partial \rho(t)}{\partial t})_{m} - g\rho(t)\,. \qquad (3.1)$$

The second term on the right-hand side of Eq. (2.22) represents the additional ionization pathways due to laser-induced localized thermal ionization.

In nanosecond pulse ablation, given the presence of the existing free seed electrons in the region, it has been proven that the cascade ionization rate greatly surpasses the multiphoton rate. Consequently, the multiphoton ionization is only considered during the early stages of the pulse in the cases when the cascade ionization cannot start due to the lack of seed electrons [Kennedy 1995; Vogel, Nahen 1996]. A similar approach was

adopted considering the localized thermal ionization. Assuming a Gaussian temporal pulse profile with pulse duration τ_0 (FWHM), a time instant t_p is defined as the time when the irradiance reaches its maximum and $t_0 \approx t_p - 2\tau_0$ as the starting time of the pulse where the irradiance is less than 1% of the peak value. As a result, the ionization of bound electrons can be separated into two processes sequentially in time: seed electron generation via thermal and multiphoton ionization from t_0 to t_s ($t_0 < t_s < t_p$), and avalanche multiplication mainly through cascade ionization starting from t_s and lasting to the rest of the pulse where the other two ionization pathways can be neglected. This approach will be justified and the estimation of the seed electron generation time $\tau_s = t_s - t_0$ will be given later in this chapter by solving the free electron density as a function of time from the Eq. (3.1) for a laser pulse with Gaussian temporal profile.

Hence, for the avalanche multiplication process, $t_s \le t$, the Eq. (2.22) takes the simple form:

$$\frac{\partial \rho(t)}{\partial t} = (\eta - g)\,\rho(t) = a \cdot \rho(t) \tag{3.2}$$

with a solution similar to Eq. (2.23) being

$$\rho(t - t_s) = \rho_0(\tau_s) e^{a(t - t_s)}. \tag{3.3}$$

In Eq. (3.3), the seed electron density, ρ_0, is provided through the thermal and multiphoton ionization during τ_s or $t_0 \le t \le t_s$

$$\frac{\partial \rho(t)}{\partial t} = \left(\frac{\partial \rho(t)}{\partial t}\right)_{th} + \left(\frac{\partial \rho(t)}{\partial t}\right)_{m}. \tag{3.4}$$

The solution of Eq. (3.4) can be found as:

$$\rho_0 = \rho(\tau_s) = \int_{t_0}^{t_s} [(\frac{\partial \rho(t')}{\partial t'})_{th} + (\frac{\partial \rho(t')}{\partial t'})_m] dt' = \rho_{th}(\tau_s) + \eta_m \cdot \tau_s , \quad (3.5)$$

where η_m is given in Eq. (2.40) and $\rho_{th}(\tau_s)$ is the free electron density generated via localized thermal ionization during τ_0 and it is assumed that the laser pulse entering the sample at $t=t_0$ with no pre-existing free electrons. With the cascade and multiphoton ionization rate given in Chapter 2, it is necessary to determine the localized thermal ionization term in Eq. (3.5) in order to obtain a solution given by Eq. (3.3).

3.2 Localized Thermal Ionization

In the localized thermal ionization, electrons bound to atoms or molecules may be freed by thermal fluctuation due to the high temperature rise within a chromophore, which absorbs the incident laser energy. The free electron density generated through thermal ionization by a laser pulse can be written as

$$\rho_{th} = \rho_{ch} n_{ch} P , \quad (3.6)$$

where ρ_{ch} is the number density of the chromophores in skin; n_{ch} is the average number of bound electrons per chromophore; P is the probability a bound electron being thermally ionized and usually depends on laser irradiance, chromophore absorption coefficient, and chromophore volume.

Even for the transient nature of the chromophore heating, it is reasonable to assume that local thermal equilibrium is reached within the chromophores on the spatial scale of 0.5~1μm [Jacques and McAuliffe 1991] and time scales of 1ns while no phase change occurs. For laser radiation at wavelengths that strongly absorbed by tissue, it will be

shown that temperature up to 10^4K can be reached, which leads to the formation of laser-induced and thermally excited free electrons acting as the seeds for avalanche ionization process. To find the explicit form of free electron density due to localized thermal ionization, additional approximations are needed owing to lacking either accurate knowledge of skin chromophores or the optical properties of biological cells in the skin tissue. First, it is assumed that various chromophores in the skin tissue can be represented by a mean absorption cross-section σ_a which is related to the bulk absorption coefficient of the skin tissue through $\mu_a = \rho_{ch}\sigma_a$ for either epidermis or dermis. Furthermore, it is also assumed that the thermal properties of the chromophores are similar to those of melanin pigments with specific heat $c_m=2.51\times10^3$(J/kg·K) and mass density $\rho_m=1.35\times10^3$(kg/m^3) [Jacques and McAuliffe 1991]. The ground substance, intercellular space and part of the collagen matrix, contains large amount of water [Anderson and Parrish 1981] and thus its thermal properties can be reasonably assumed to be as those of water with specific heat $c_w=4.19\times10^3$(J/kg·K), mass density $\rho_w=1.00\times10^3$(kg/m^3), and thermal conductivity κ_w =0.57(J/m·s·K). In addition, the light absorption by the ground substance is, like water, negligible in the spectral region from 200 to 1300nm [Ojamae, Tegenfeldt 1992].

The characteristic time of thermal energy transportation can be estimated from elementary considerations of the thermal diffusion process within the chromophore having a characteristic size R_{ch} about 0.5~1μm [Ojamae, Tegenfeldt 1992]. If the thermal flux is linearly related to the temperature gradient ΔT between the inside of a

chromophore and the ambient temperature, then the transportation speed of the corresponding energy over the scale of R_{ch} is approximately given by considering the heat transfer between two regions with volume ΔV, mass Δm, density ρ_m, a distance L between them and the thermal energy $\Delta\varepsilon_{th}$ transported between them. athermal flux j through thermal diffusion is hence defined as:

$$j = -k\frac{\Delta T}{\Delta x} = -k\frac{\Delta T}{\Delta \varepsilon_{th}} \cdot \frac{\Delta \varepsilon_{th}}{L} = -k\frac{1}{c_v \cdot \Delta m} \cdot \frac{\Delta \varepsilon_{th}}{L}. \tag{3.7}$$

The thermal flux is the equivalent to the flow of thermal energy with a density ρ_{th} at a speed v_{th}:

$$j = \rho_{th} \cdot v_{th} = \frac{\Delta \varepsilon_{th}}{\Delta V} \cdot v_{th}. \tag{3.8}$$

From Eqs. (3.8) and (3.7):

$$\frac{\Delta \varepsilon_{th}}{\Delta V} \cdot v_{th} = -k \cdot \frac{1}{c \cdot \rho_m} \cdot \frac{\Delta \varepsilon_{th}}{\Delta V} \cdot \frac{1}{L}, \tag{3.9}$$

or

$$\left| v_{th} \right| = \frac{k}{c \cdot \rho_m} \cdot \frac{1}{L}. \tag{3.10}$$

Then the thermal energy transfer speed in a chromophore is given:

$$v_{th} = \frac{\kappa_m}{\rho_m c_m R_{ch}} \approx 0.2\left(\frac{m}{s}\right), \tag{3.11}$$

where the thermal conductivity of the chromophore have been assumed $\kappa_m \approx \kappa_w$. For a laser pulse duration of 10ns, thermal conduction over the size of a chromophore is

consequently negligible and the heating within the chromophore can be regarded as an adiabatic process or under an inertial confinement condition [Albagli, Perelman 1994]. Using the same argument, a condition of fixed volume for the chromophore during the heating process can be assumed since the changes in the chromophore volume can be ignored during the laser pulse. For a laser pulse with fluence $\Phi_0(t)$, the energy absorbed by a chromophore is given by

$$\Delta E(t) = \Phi_0(t) \cdot \sigma_a . \tag{3.12}$$

and the corresponding temperature rise inside the chromophore can be obtained as

$$\Delta T = T - T_0 = \frac{\Delta E(t)}{c_m \rho_m v_m} = \frac{\Phi_0(t)\sigma_a}{c_m \rho_m v_m}, \tag{3.13}$$

where v_m is the volume of the chromophore and T_0 is the ambient temperature.

In the ultraviolet region, the skin has an electronic absorption peak around 270nm [Anderson and Parrish 1981; Parrish and Deutsch 1984] due to the light absorption by urocanic acid and DNA, which corresponds to an energy level at 4.5eV above the ground states. Bound electrons excited onto this energy level will become quasi-free electrons shared by neighboring ions. Therefore, the ionization energy for chromophores E_{ion}, can be assumed to be about 4.5eV. Melanin by itself, however, shows no characteristic absorption maxima in the visible or the UV regions, while its absorption increases monotonically with decreasing wavelength. The population of the bound electrons inside tissue follows Fermi-Dirac distribution and is a function of temperature T when a local thermal equilibrium inside the chromophore is reached. To determine the probability for a bound electron to be thermally ionized, it is necessary to know the energy distribution

of electronic states inside the skin chromophore, which, at this time, is not available in literature. Therefore, the widely accepted results for the density of states for electrons in amorphous semiconductors are used [Tauc 1974; Ashcroft and Mermin 1976; Morigaki 1999] to calculate the localized thermal ionization probability.

In the modeling of thermal ionization, a simple two-band energy structure of energy states is assumed for the density of state for electrons inside a skin chromophore: the band of bound states at E=0 and a band of ionized states with lowest energy at E_{ion}. The chemical potential μ, is approximated to be in the middle of the gap between the band: $\mu \approx E_{ion}/2$ [Ashcroft and Mermin 1976], which is the same as many amorphous semiconductors. The density of the state for the electrons in the ionized states with energy $\varepsilon \geq E_{ion}$ may thus be written as [Morigaki 1999]:

$$g(\varepsilon) = 8\pi \left(\frac{2m_e}{h^2} \right)^{\frac{3}{2}} \sqrt{\varepsilon - E_{ion}} , \tag{3.14}$$

where m_e is the electron mass and h is the Plank constant. According to Fermi-Dirac distribution, the probability of finding an electron in a quantum state with energy ε under thermal equilibrium condition is given by

$$f(\varepsilon) = \left[\exp\left(\frac{\varepsilon - \mu}{k_B T} \right) + 1 \right]^{-1} . \tag{3.15}$$

where k_B is the Boltzmann's constant. Hence, the density of quasi-free electrons with energy $\varepsilon \geq E_{ion}$ is provided by

$$N(E_{ion}) = \int_{E_{ion}}^{\infty} g(\varepsilon) f(\varepsilon) d\varepsilon \,. \tag{3.16}$$

In the case of the ionization energy E_{ion} and the temperature T satisfying the condition:

$$e^{(E_{ion}-\mu)/k_B T} >> 1\,, \tag{3.17}$$

the electrons are assumed to be in the so called "nondegenerate" electronic states that the Fermi-Dirac distribution function can be approximated by the Boltzmann distribution.

$$\begin{aligned} N(E_{ion}) &= \int_{E_{ion}}^{\infty} g(\varepsilon) f(\varepsilon) d\varepsilon \\ &= 8\pi \left(\frac{2m_e}{h^2}\right)^{\frac{3}{2}} \int_{E_{ion}}^{\infty} \sqrt{\varepsilon - E_{ion}} \, \frac{d\varepsilon}{e^{\frac{\varepsilon-\mu}{k_B T}} + 1} \\ &\approx 8\pi \left(\frac{2m_e}{h^2}\right)^{\frac{3}{2}} e^{\mu/k_B T} \int_{E_{ion}}^{\infty} e^{-\varepsilon/k_B T} \cdot \sqrt{\varepsilon - E_{ion}} \cdot d\varepsilon \\ &= 8\pi \left(\frac{2m_e}{h^2}\right)^{\frac{3}{2}} \cdot \frac{\sqrt{\pi}}{2} \cdot (k_B T)^{3/2} \cdot e^{\mu/k_B T} \cdot e^{-E_{ion}/k_B T} \end{aligned} \,. \tag{3.18}$$

Eq. (3.17) can be very well satisfied for $T \leq 10^4$ K when the ionization energy E_{ion} is 4~6eV. The total electron density consists of two parts: the ionized free electron and the bound electron. Since the critical electron density for plasma formation ($\sim 10^{18}/cm^3$) is only a very small fraction of the total bound electron density ($\sim 10^{23}/cm^3$) [Kennedy 1995; Vogel, Nahen 1996], the change of the total number of bound electrons due to ionized electrons can be neglected and hence treated as constant. Subsequently, the total bound electron density $N=N(E \to \infty)$ at any temperature T can be approximated by the total bound electron density at T=0K, which follows the Fermi-Dirac distribution given by

$$f(\varepsilon)=\begin{cases}1, \varepsilon \le \mu \\ 0, \varepsilon > \mu\end{cases}. \tag{3.19}$$

Hence, the following integral can be evaluated as

$$N=\int_0^\infty g(\varepsilon) f(\varepsilon) d\varepsilon = 8\pi\left(\frac{2m_e}{h^2}\right)^{\frac{3}{2}} \int_0^\infty \sqrt{\varepsilon} f(\varepsilon) d\varepsilon = 8\pi\left(\frac{2m_e}{h^2}\right)^{\frac{3}{2}} \cdot \frac{16}{3}\mu^{3/2} \tag{3.20}$$

Since a bound electron is assumed to be ionized when its energy exceeds the ionization energy E_{ion}, the localized thermal ionization probability of a bound electron is given by the portion of bound electrons with energy $E \ge E_{ion}$ at a local temperature T:

$$\begin{aligned} P=\frac{N(E_{ion})}{N} &= \frac{3\sqrt{\pi}}{4}\cdot\left(\frac{k_B T}{\mu}\right)^{\frac{3}{2}} e^{\mu/k_B T}\cdot e^{-E_{ion}/k_B T} \\ &\approx \frac{3\sqrt{\pi}}{4}\cdot\left(\frac{k_B T}{E_{ion}/2}\right)^{\frac{3}{2}}\cdot e^{-E_{ion}/2k_B T} \end{aligned}, \tag{3.21}$$

where $\mu \approx E_{ion}/2$ was used in the last step. It should be noted that Eq. (3.21) is only valid when Eq. (3.17) is satisfied. For temperature higher than 10^4 K, the localized thermal ionization probability approaches to 1, which means all the bound electrons are ionized. Therefore, the free electron density generated through the localized thermal ionization during the period of τ within the laser pulse duration is:

$$\begin{aligned} \rho_{th}(\tau) &= \rho_{ch}\cdot n_{ch}\cdot P \\ &= \rho_{ch}\cdot n_{ch}\cdot\frac{3\sqrt{\pi}}{4}\cdot\left(\frac{k_B T}{E_{ion}/2}\right)^{\frac{3}{2}}\cdot e^{-E_{ion}/2k_B T} \\ &= \rho_{ch}\cdot n_{ch}\cdot\frac{3\sqrt{\pi}}{4}\cdot\left[\frac{k_B}{E_{ion}/2}\cdot\left(T_0+\frac{\sigma_a\cdot I\cdot\tau}{c_m\rho_m v_m}\right)\right]^{\frac{3}{2}}\cdot\exp\left\{-\frac{E_{ion}/2k_B}{T_0+\frac{\sigma_a\cdot I\cdot\tau}{c_m\rho_m v_m}}\right\} \end{aligned}. \tag{3.22}$$

3.3 Solutions of the Rate Equation and Discussion

In the previous section, the localized thermal ionization pathway was studied and the corresponding free electron density was obtained. Along with the cascade and multiphoton ionization rates given in Chapter 2, it is possible now to quantitatively compare the three ionization pathways in skin tissue ablation by nanosecond laser pulses. The numerical calculations can provide important insights on the plasma-mediated ablation processes in cases of significant tissue absorption. Before proceeding to solve the modified rate equation, it is instructive to consider the effects of the three pathways on the ionization process independently at different times to illustrate their roles in the optical breakdown process. Under the single-pulse condition, the free electron density generated due to each of the three pathways can be found by either setting other ionization rates to zero in the rate equation (3.1) for cascade and multiphoton ionizations or through Eq. (3.6) for thermal ionization:

$$\rho_{th}(\tau_s) = \rho_{ch} \cdot n_{ch} \cdot \frac{3\sqrt{\pi}}{4} \cdot \left[\frac{k_B}{\mu} \cdot \left(T_0 + \frac{\sigma_a \cdot I \cdot \tau_s}{c_m \rho_m v_m} \right) \right]^{\frac{3}{2}} \cdot \exp\left\{ - \frac{E_{ion}/2k_B}{T_0 + \frac{\sigma_a \cdot I \cdot \tau_s}{c_m \rho_m v_m}} \right\}, \quad (3.23)$$

$$\rho_m(\tau_s) = \eta_m \cdot \tau_s = \left(\frac{2}{9\pi}\right) \frac{\omega}{\rho_b} \left(\frac{m'\omega}{\hbar} \right)^{\frac{3}{2}} e^{2K} \Phi(z) \left(\frac{1}{16}\right)^K \left(\frac{e^2 I_0}{m' \Delta \quad \omega^2 c \varepsilon_0 n_0} \right)^K \cdot \tau_s, \quad (3.24)$$

$$\rho_c(\tau) = \rho_0(\tau_s) e^{\eta(\tau_0)}, \quad (3.25)$$

where ρ_c is the free electron density due to cascade ionization; ρ_{th} due to thermal and ρ_m due to multiphoton ionization. For thermal and multiphoton ionization, the seed electron generation time $\tau_s = t_s - t_0$ is used and their contribution to the overall free electron density

once cascade ionization starts has been neglected, where $t_0=t_p-2\tau_0$ is defined as the starting point of the pulse and t_s is the time after which only cascade ionization should be considered. For cascade ionization, a free seed electron density $\rho_0(\tau_s)$ is assumed to be present inside the illuminated region at t_s, and the pulse duration τ_0 is used to calculate the free electron density.

In order to compare the new plasma model with experimental data, the parameter values were adopted corresponding to the experiment conditions for the numerical calculation of the free electron density. The parameters used in the calculation are given by τ_0=10ns, E_{ion}=4.56eV, $R_c=5\times10^{-7}$m (estimated from the size of the melanin granules), $\rho_b=1.0\times10^{29}m^{-3}$, and $C_m=2.15\times10^{3}J\cdot K^{-1}\cdot kg^{-1}$. In the experiment of surface ablation of skin tissue with a 75mm focusing lens at different wavelengths of 1064, 532, 266 and 213nm, the volume of the focal point is given by $V_0=\pi\omega_x\omega_y D\sim10^{-8}cm^3$, in which ω_x and ω_y are the radii of the cross section of the focusing spot and D is the penetration depth. As an estimate of the number of the bounded electrons inside an average chromophore containing proteins, the number of bounded electrons in each protein is assumed to be on the same order of its molecular weight. On average, a typical cell has about 5×10^6 protein molecules whose average molecular weight is on the order of 10^5 [Hughes 1979; Kollias, Sayre 1991]. Therefore, the number of bound electrons in an average chromophore, n_{ch}, is approximately 10^{11}. The total bound electrons inside the chromophores within the focusing region is given by:

$$N_0 = V_0 \cdot \rho_{ch} \cdot n_{ch}, \tag{3.26}$$

where ρ_{ch} (m^{-3}) is the chromophore number density in skin tissue. The chromophore mass can be found by $m_{ch} \approx n_{ch} \times m_p \approx 10^{11} \times 1.67 \times 10^{-27} kg \approx 2 \times 10^{-16} kg$, where m_p is the proton mass and it is assumed there's one bound electron per atom. If assuming 20% of the wet weight of skin tissue consists of absorbing chromophores, then the chromophore number density in the tissue is given by $\rho_{ch}=0.2\rho_m/m_{ch} \approx 1.0 \times 10^{18}/m^3$, where $\rho_m \approx 1.0 \times 10^3 kg/m^3$ is the mass density of most non-fat soft tissues including the skin. The chromophore absorption cross-section σ_a, is subsequently estimated through the relation $\mu_a = \rho_{ch}\sigma_a$. Table 3-1 lists the values of the parameters used in calculations and readers are referred to Chapter 2 for definitions of these parameters.

Table 3-1 Wavelength dependence parameters for free electron density calculation.

	1064nm	532nm	266nm	213nm
σ_a ($10^{-16} m^2$)*	5.0	1.0	60	126
D (m)	5.42×10^{-4}	3.39×10^{-4}	5.65×10^{-5}	2.69×10^{-5}
K	6	3	2	2
z	0.885	0.626	1.09	1.32
$\Phi(z)$	0.540	0.485	0.527	0.477

*Calculated from the absorption coefficient of dermis [van Gemert, Jacques 1989].

For a 10ns pulse at 532nm with a Gassian temporal profile, the free electron densities generated through the three pathways as a function of time within the first half of pulse duration $\tau_0/2$ are compared in Figure 3-1 along with the laser irradiance. At the beginning of the pulse when there are few free electrons in the illuminated region, the

cascade ionization pathway develops very slowly while the localized thermal ionization rises quickly until saturation when all the bound electrons inside the chromophores have been ionized. The multiphoton ionization changes slowly throughout the whole pulse duration. Consequently, the seed electron generation characteristic time was chosen to be $\tau_s \approx \tau_0/5$, a choice same as the one employed for estimating the seed electron generation via multiphoton ionization [Kennedy 1995; Kennedy, Boppart 1995; Vogel, Nahen 1996]. The multiphoton and thermal ionization contributions to the overall free electron density during the rest of the pulse duration can be neglected without introducing much error. Figure 3-1 clearly shows that even at the wavelength with very weak absorption, the localized thermal ionization exceeds the multiphoton pathway for nanosecond laser pulses in providing free seed electron for the cascade or avalanche ionization process to start.

Figure 3-2 to Figure 3-5 depict the free electron density through the three pathways at 1064, 532, 266, and 213nm as a function of incident laser irradiance at the peak of the pulse. At low irradiance where there is not sufficient seed electrons to initiate cascade ionization, the localized thermal ionization contribution rises at a faster rate as shown in the figures. At irradiance near the threshold value, however, it is shown that the free electron density from cascade ionization increases at much higher rate than that of either thermal or multiphoton ionization when there are enough seed electrons in the illuminated region. At 1064nm and 532nm the tissue absorption is small and the localized thermal ionization contribution is significantly less than that of the cascade ionization for $t > t_s$. Therefore, it has less influence to the overall free electron generation

as well as the ablation thresholds as shown in Figure 3-2 and Figure 3-3. Therefore, it is reasonable for the existing plasma models to ignore the two pathways in the homogeneous and weakly absorbing mediums or nanosecond pulses. In the ultra violet region at 266nm and 213nm as shown in Figure 3-4 and Figure 3-5, significant tissue absorption in the chromophores causes the localized thermal ionization contribution surpassing the cascade ionization at low irradiance range and therefore cannot be neglected when calculating the thresholds. Since the photon energy is larger than E_{ion} for UV wavelengths, multiphoton absorption can be neglected in the discussion.

To illustrate the effect of tissue absorption on the generation of free electron, the different $\rho_{th}(I)$ at 1064, 532, 266, and 213nm are compared in Figure 3-6. The localized thermal ionization contribution rise rapidly as laser irradiance increases and then saturates at all four wavelengths when the localized thermal ionization probability approaches to 1, which means nearly all bound electrons in tissue chromophores have been ionized. Because of the strong dependence on the tissue absorption shown in Eq. (3.23), free electron generated through thermal ionization rises faster at wavelength where tissue absorption is greater, i.e. it reaches saturation at 266 and 213nm with irradiance two orders of magnitude less than at 532 and 1064nm. For comparison, the irradiance dependence of the free electron density generated through cascade ionization is plotted at 1064, 532, 266, and 213nm in Figure 3-7. Since the cascade ionization rate is higher at longer wavelength as given by Eq. (2.40), its contribution to free electron density rises faster in the visible and near-infrared than that in the ultraviolet.

The total free electron density generated through ionization is given by the solution of the modified rate equation (3.1). For avalanche multiplication through cascade ionization, the solution is given by Eq. (3.3), where the initial free electron density is the summation of existing free electrons in the medium ρ_c and free electrons generated by multiphoton and thermal ionization within t_s. When the existing free electrons in tissue can be neglected, i.e. $\rho_c \sim 0$, the total free electron density generated via the three pathways within the pulse duration τ_0 is given by:

$$\rho(t) = \begin{cases} \rho_{th}(t) + \eta_m t, & t \le t_s \\ \rho_0 e^{(\eta_c - g)t}, & t_s \le t \le \tau_0 \end{cases}. \tag{3.27}$$

Since the free electron density considered in this study is less than the critical free electron density for plasma generation, $\rho \le \rho_{cr} \sim 10^{24}/m^3$, the total bound electron density, $\rho_b \sim 10^{29}/m^3$, can be assumed as a constant [Kennedy 1995]. Therefore, the thermal and multiphoton contributions to the total free electron density do not depend on the presence or the quantity of existing free electrons in the region. Consequently, when all three pathways are considered, the free electron generated from thermal and multiphoton ionization are the same as when they develop independently as given by Eqs. (3.23) and (3.24). The thermal and multiphoton ionization contributions to the overall free electron density beyond t_s are neglected. The free electron generation through all three pathways according to Eq. (3.27) is plotted in Figure 3-8 as a function of laser irradiance at 1064, 532, 266, and 213nm.

Optical breakdown or plasma generation irradiance threshold is defined as the irradiance when the free electron density reaches a critical value $\rho_{cr}=10^{24}/m^3$ [DeMichelis

1969; Bloembergen 1974; Shen 1984; Kennedy 1995]. Figure 3-7 plots the theoretical predication of the total free electron generation at the four wavelengths in the early stage of plasma formation including the contribution of all three pathways according to this model. Additional curves also plotted in Figure 3-9 are the wavelength dependence of the ablation irradiance thresholds calculated from the plasma medicated model as well as the experiment result given by Hu *et al*. [Hu, Fang 2001] and from other models discussed in Chapter 2. Figure 3-6 shows that the shorter ablation wavelength, the faster the free electrons generated via thermal ionization. On the contrary, the free electron generated through cascade ionization, given in Eq. (3.25), increases slower with the increasing of laser irradiance when the ablation wavelength becomes shorter, as shown in Figure 3-7. The wavelength dependences of free electron density generation for different ionization pathways are shown in Figure 3-9 in term of threshold dependence on laser wavelength. Specifically, if thermal ionization can be neglected, i.e. only considering the cascade ionization [Kennedy 1995; Vogel, Nahen 1996], the ablation threshold decreases when the laser wavelength increases from ultraviolet to near inferred. In the case when the localized thermal ionization contribution cannot be neglected, however, this ablation model predicts that the ablation threshold will increase with the increase of the laser wavelength, which is consistent with the experiment results also shown in Figure 3-9. In addition, it should be noted here that according to Eqs. (3.23), (3.24), and (3.27), the free electron density does not have a focusing spot size dependence, as predicted by Vogel *et al.* [Vogel, Nahen 1996].

The new plasma model will be further analyzed and discussed with the experiment results in Chapter 4 and 5.

Chapter 3 Figures

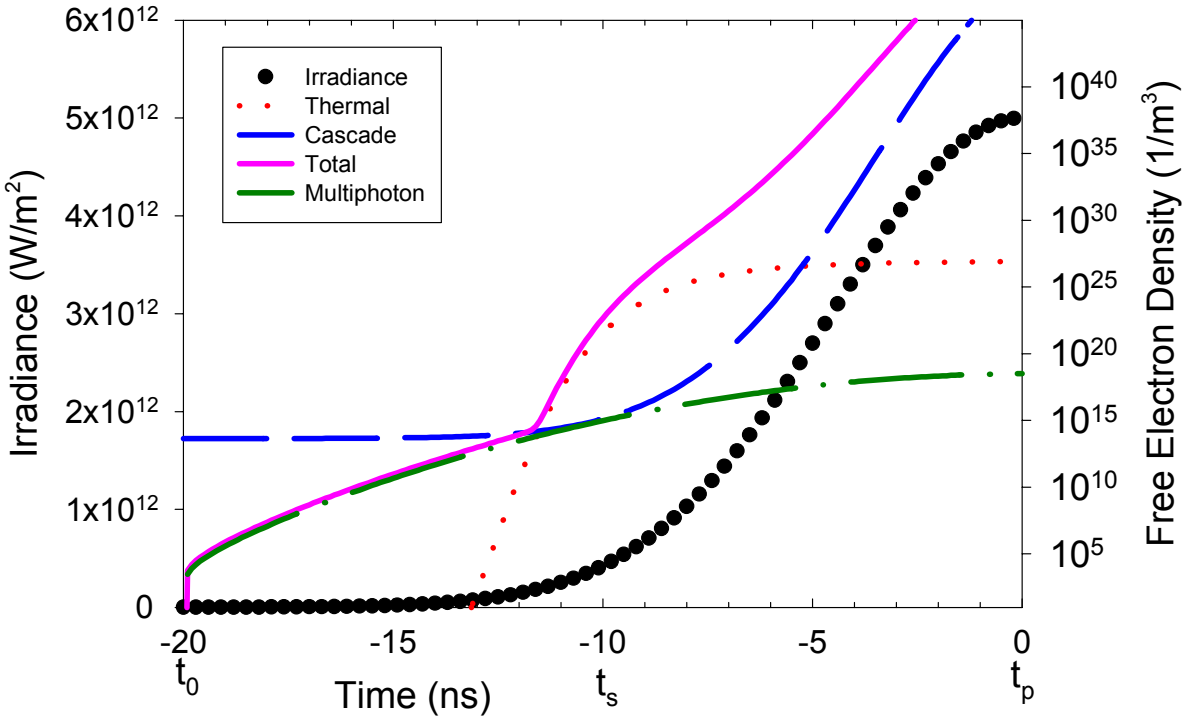

Figure 3-1 Free electron density generation through different pathways as a function of time at 532nm. Pulse duration ($1/e^2$ definition) τ_0=9ns; t_p is the peak of the Gaussian pulse; $t_0=t_p-2\tau_0$ is defined as the starting point of the pulse where the pulse irradiance is less than 1% of the peak value; t_s is the seed electron generation time. Total ionization: solid line; cascade ionization with minimum initial seed electron density: short dash line; thermal ionization: dot line; multiphoton ionization: dash-dot line; laser irradiance with Gaussian temporal profile: circle (Theory_Time.jnb.)

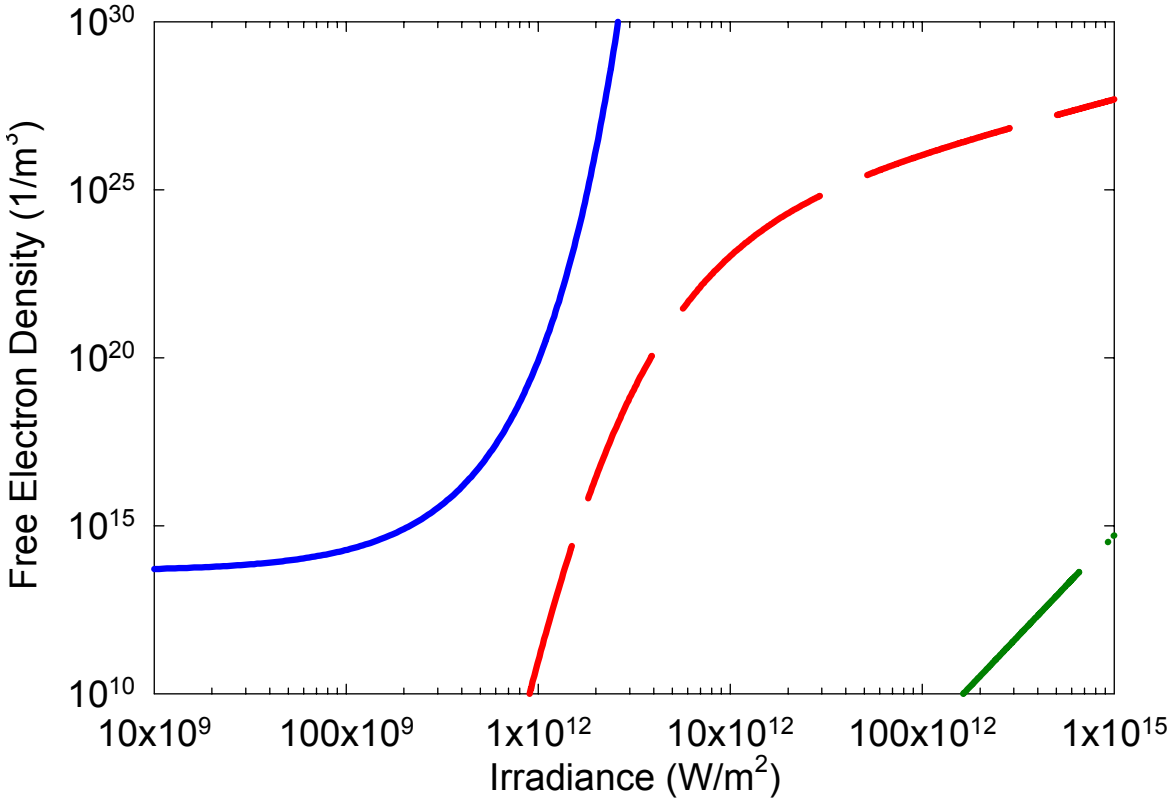

Figure 3-2 Laser irradiance dependence of free electron density at 1064nm. Solid line: Free electron density due to cascade ionization only with $\rho_0=\rho_0(\min)$; short dash line: due to thermal ionization only; dash-dot line: due to multiphoton ionization only (Theory_Figures.jnb.)

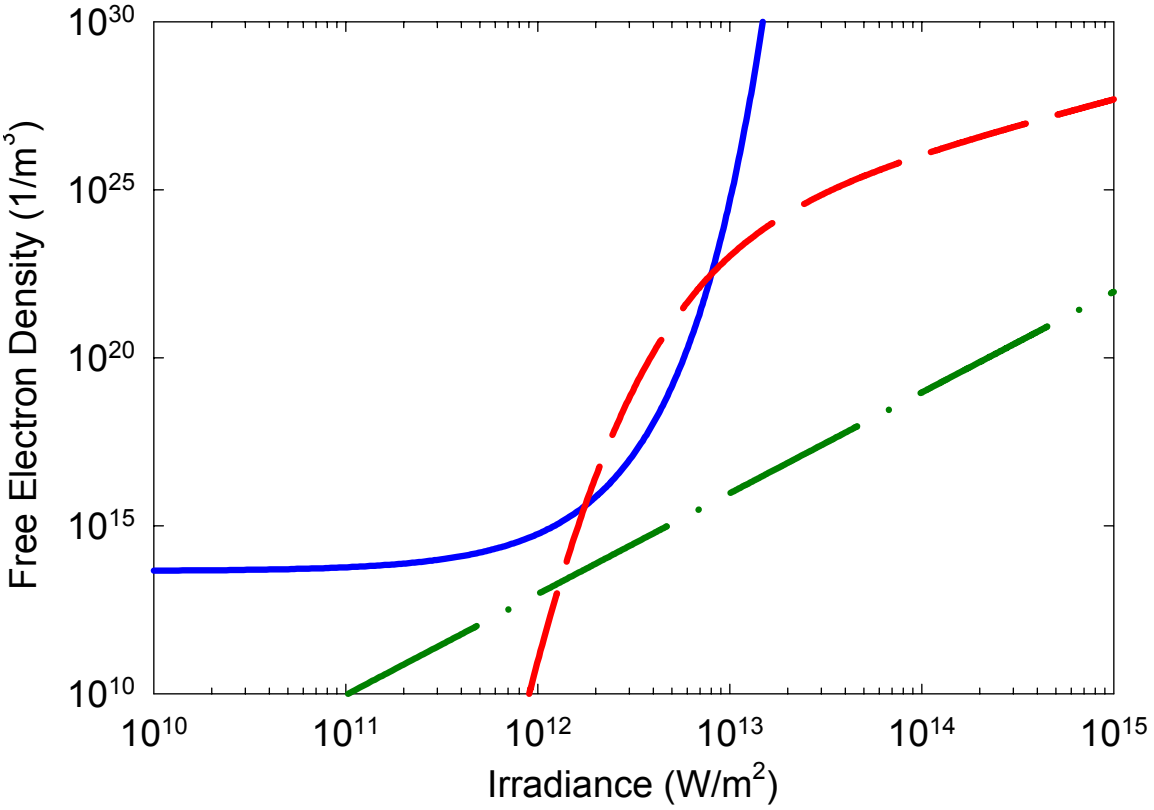

Figure 3-3 Laser irradiance dependence of free electron density at 532nm. Solid line: Free electron density due to cascade ionization only with $\rho_0=\rho_0(\min)$; short dash line: due to thermal ionization only; dash-dot line: due to multiphoton ionization only (Theory_Figures.jnb.)

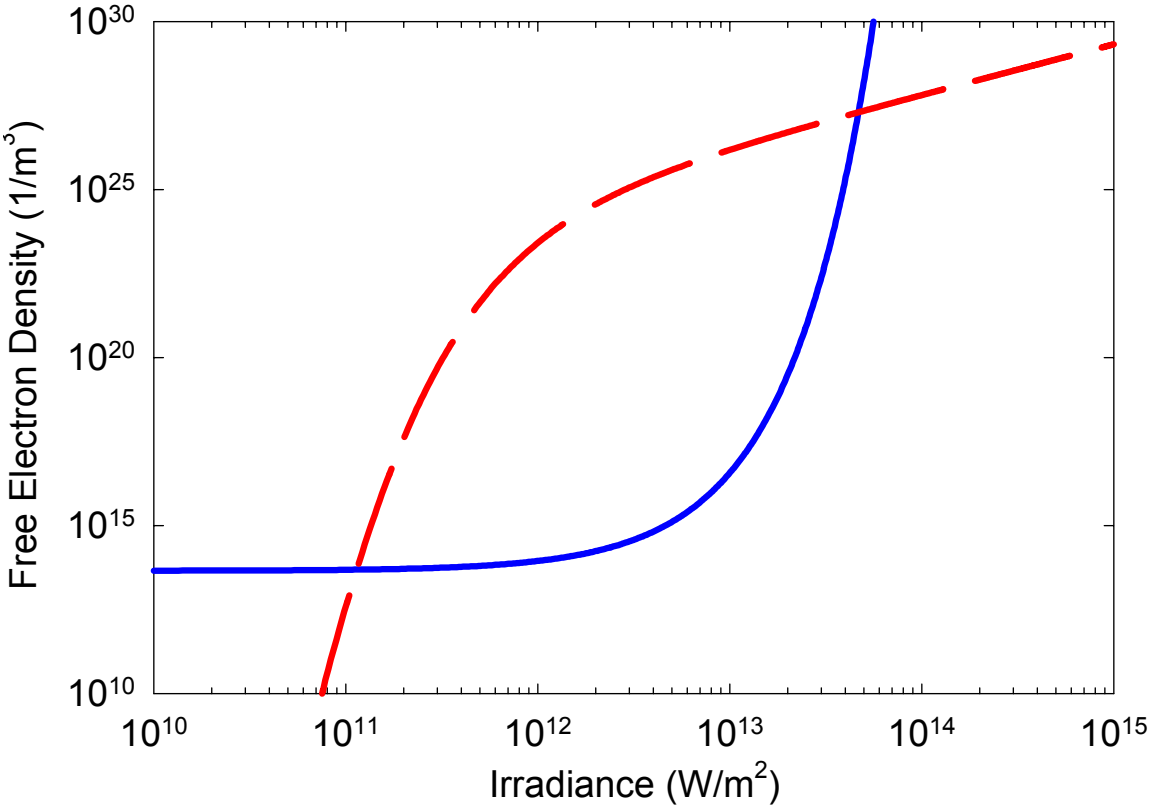

Figure 3-4 Laser irradiance dependence of free electron density at 266nm. Solid line: Free electron density due to cascade ionization only with $\rho_0=\rho_0(\min)$; short dash line: due to thermal ionization only (Theory_Figures.jnb.)

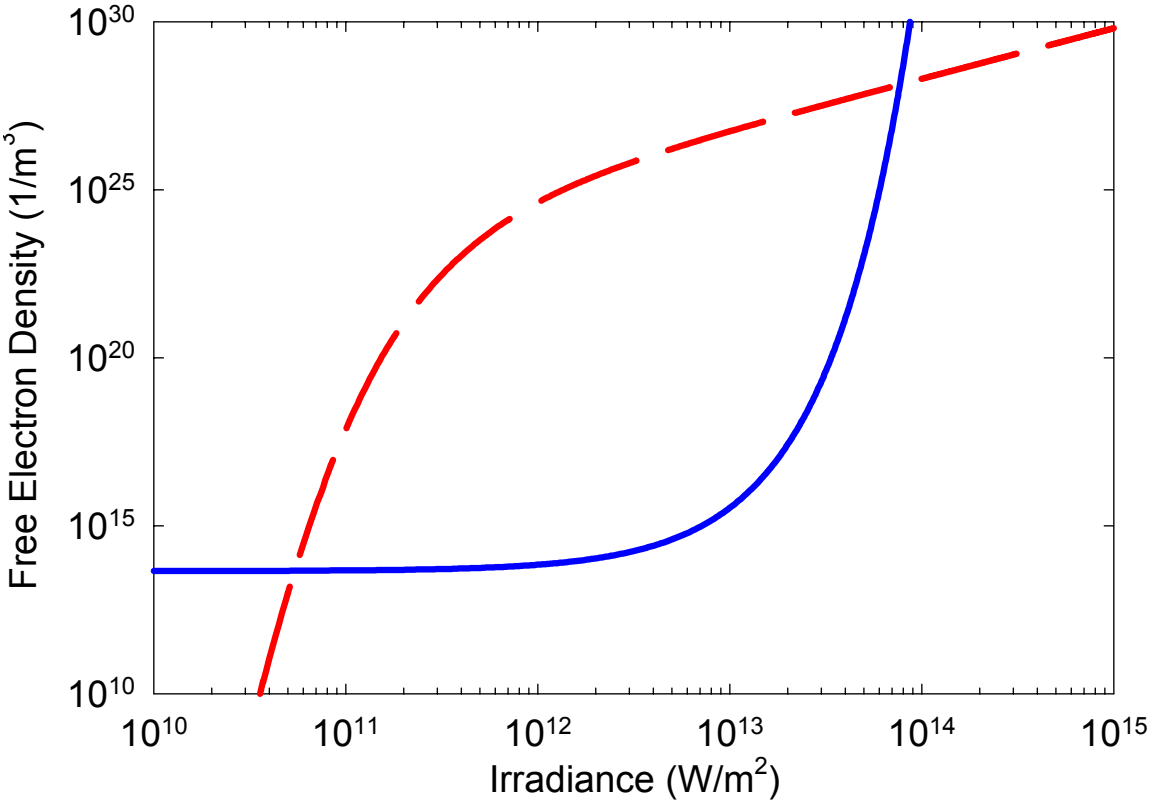

Figure 3-5 Laser irradiance dependence of free electron density at 213nm. Solid line: Free electron density due to cascade ionization only with $\rho_0=\rho_0(\min)$; short dash line: due to thermal ionization only; dash-dot line: due to multiphoton ionization only (Theory_Figures.jnb.)

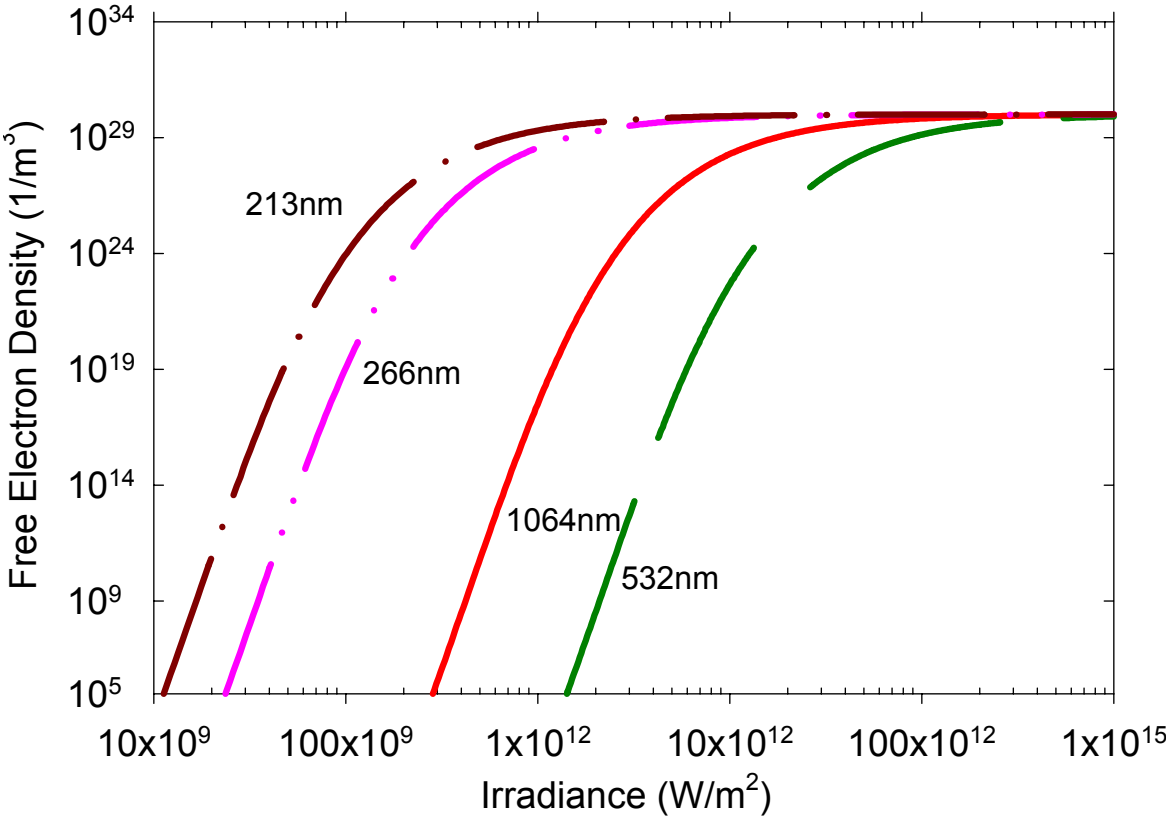

Figure 3-6 Free electron density generated by thermal ionization of the chromophores in skin at 1064nm: solid line, 532nm: long dash line, 266nm: dash-dot-dot line, and 213nm: dash-dot line (Theory_Figures.jnb.)

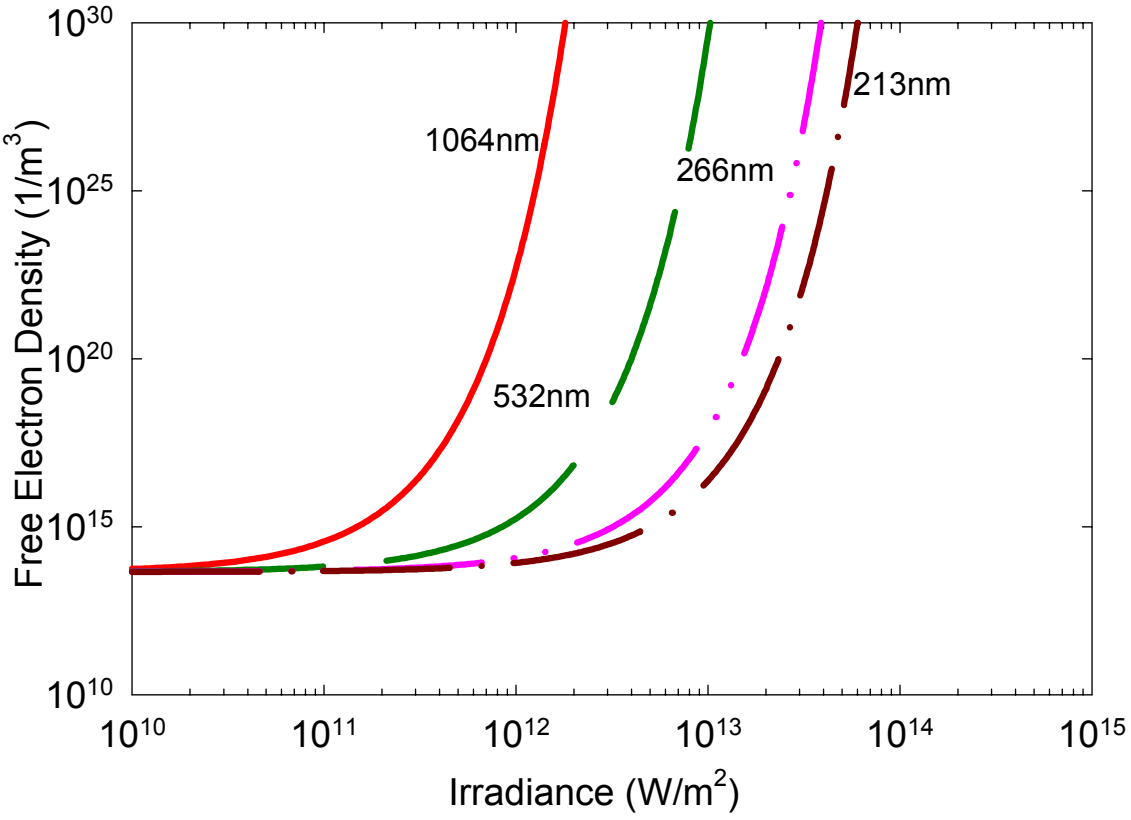

Figure 3-7 Free electron density generated by cascade ionization with minimum initial free electron density at 1064nm: solid line, 532nm: long dash line, 266nm: dash-dot-dot line, and 213nm: dash-dot line.

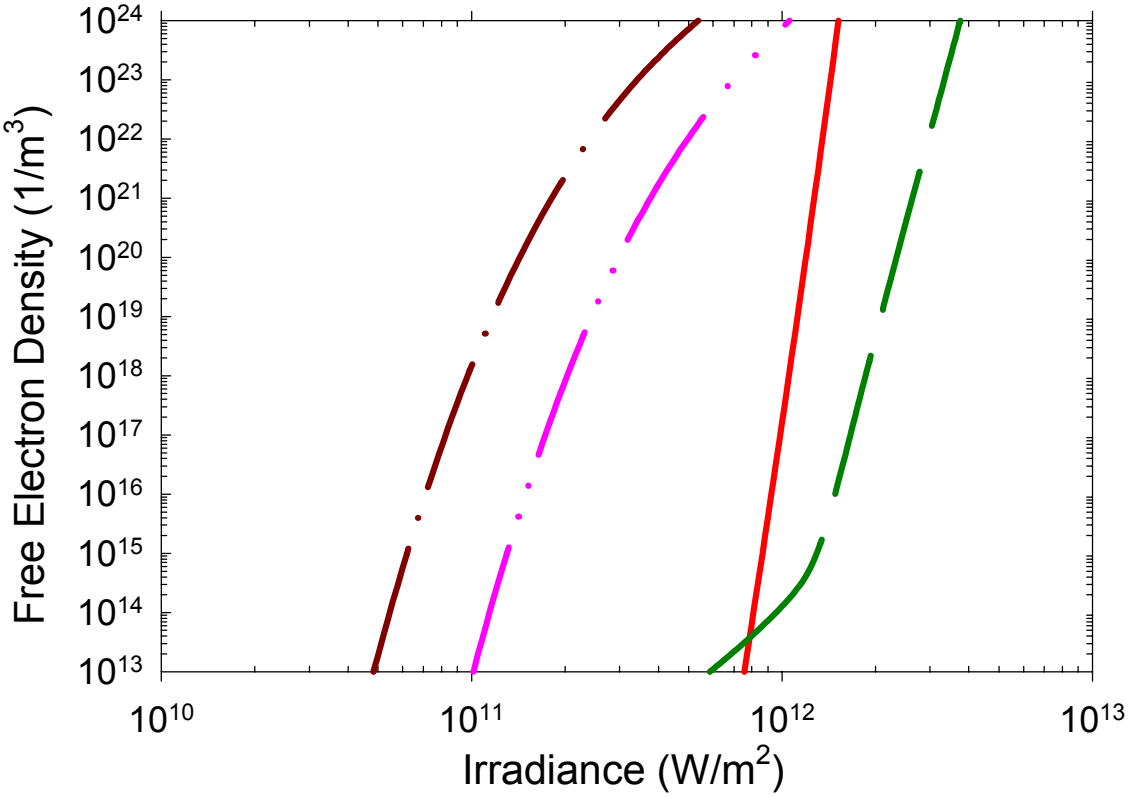

Figure 3-8 Free electron density generated by all three ionization pathways at 1064nm: solid line, 532nm: medium dash line, 266nm: dash-dot-dot line, and 213nm: dash-dot line (Theory_Figures.jnb.)

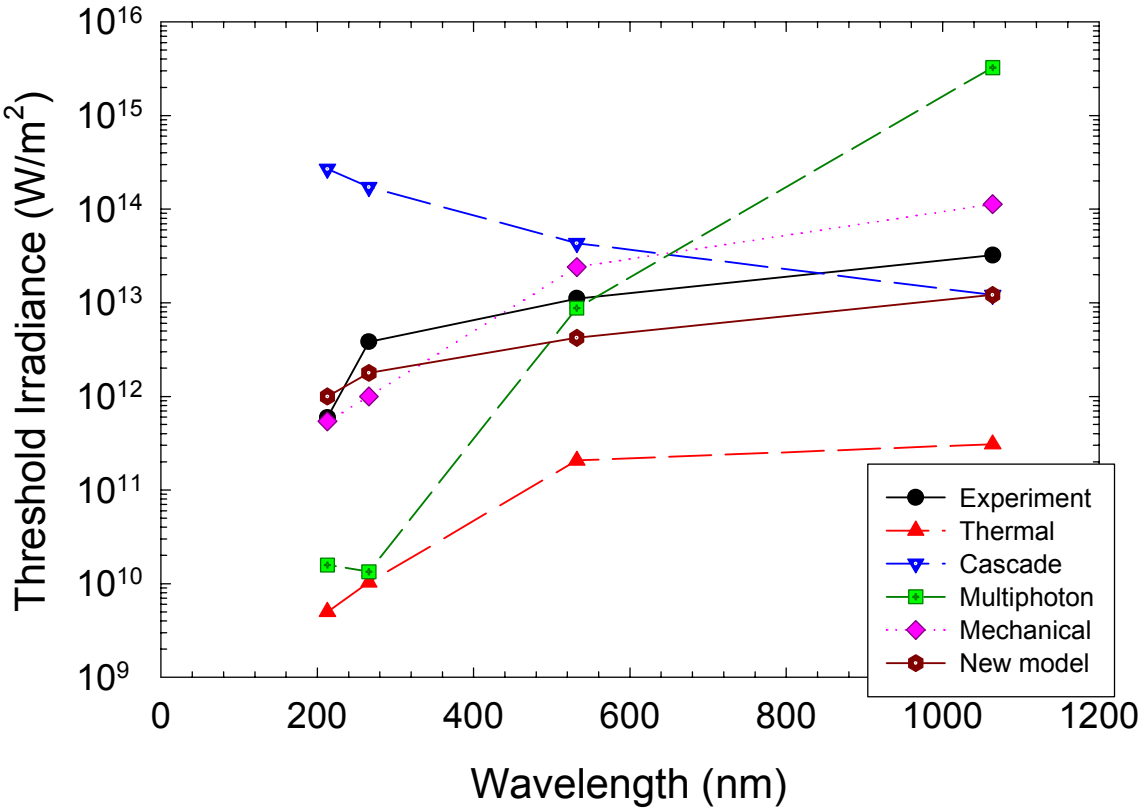

Figure 3-9 Wavelength dependence of the ablation thresholds for circle: experiment by Hu, diamond: inertial confinement model by Feld et al., triangle upside down: plasma model only considering cascade ionization Kennedy et al., square: initial seed electron generation threshold via multiphoton ionization, triangle: initial seed electron generation threshold via thermal ionization, and circle with dot: plasma model considering all three pathways (Theory_Figures.jnb.)

Chapter 4 Experimental Results I – Skin Tissue

This chapter describes experimental study of the skin tissue ablation process. First, the laser wavelength dependence of the ablation thresholds will be given in section 4.1, which is followed by the spot size dependence measurement depicted in section 4.2. In the next section, the results from two different ablation depth measurements that validate the optical methods of ablation used in the previous two sections will be shown. In order to study how tissue absorption affects the ablation process, the measurements of tissue attenuation coefficient will be depicted in section 4.4. In the last section, the experimental results will be discussed as well as compared against the theoretical model proposed in Chapter 3.

4.1 Wavelength Dependence of the Ablation Thresholds and rate

For soft biological tissue ablation by nanosecond pulses, the characteristics of the plasma-mediated ablation model need to be further elucidated and acceptance of the plasma model is far from ubiquitous, especially when tissue absorption becomes significant as the light wavelength approaches the ultraviolet region. It appears that the ambiguity of the fundamental mechanism underlying tissue ablation by nanosecond laser pulses is largely related to the lack of quantitative studies of the ablation process near the threshold. Given this fact, the ablation of fresh porcine skin *in vitro* using nanosecond laser pulses at 1064, 532, 266 and 213nm have been studied. Besides the inherent importance of studying fundamental mechanisms, a clear understanding of the ablation process of soft tissue by nanosecond laser pulses will benefit the exploration of new

approaches in surgical applications of nanosecond lasers. In this section, the spectral analysis of secondary radiation and histological analysis of ablated porcine skin samples near the ablation threshold will be present. Based on these results, a spectral signature of the tissue ablation has been established in which the measurements of the ablation probability are carried out at the four ablating wavelengths.

4.1.1 Methods

For accomplishing the goal of quantitative investigation of skin tissue ablation process, the spatial distribution of the radiation energy in the focal spot have been carefully studied to ensure that it is consistent with the Gaussian distribution assumed in the new plasma model described in Chapter 3. The system schematic is shown in Figure 4-1. A Q-switched Nd:YAG laser (Surelite I, Continuum) was used to generate pulses of 100mJ energy at the fundamental wavelength of 1064nm with the flash-lamp voltage reduced to 0.95kV from the factory-set value of 1.25kV. The maximum pulse energy could be further reduced by 50% via modifying the Q-switch delay time from at 203μs at which the pulse energy peaks to 260μs. The delay results in variations in the pulse duration from 9ns at 203μs to 15ns at 260μs. The pulse energy was continuously adjusted by a half-wave plate and a polarization cube. The pulse-to-pulse energy fluctuation was determined to be ±5% by reflecting a small portion of the beam using a BK7 glass wedge to a fast Si photodiode detector (FDS-010, Thorlabs, 1ns rise time). The beam profile was monthly optimized by adjusting the tilting of the cavity end mirror while the temporal profile was monitored by an oscilloscope (53111D, 500MHz, HP) through the

fast photodiode detector and the spatial profile was monitored by a beam profiling system (LBA-PC 300, Spiricon). For experiments requiring pulse energies less than 5mJ at 1064nm, an optical wedge and mirrors were inserted before the half-wave plate to use only the portion of the beam reflected from the front surface for reducing the excessive distortion of beam profile after the polarization cube.

A plano-convex lens of 75mm focal length was employed to focus the laser beam of 0.6mrad divergence on the skin sample surface. The f-number for a lens is defined as $N_f=f/D$, where f is the focal length and D is the smaller one of the incident beam diameter or lens aperture. The aberration function Φa for a plano-convex lens is defined as the distance between the focal points of on axis light and light parallel to axis with a distance of D/2, which is given by [Ireland, Yi 1974]:

$$\Phi_a = -\frac{D^4}{128f^3}\left[\frac{n^2}{4(n-1)^2} - \frac{n}{4(n+2)} + \frac{\left(2n^2-n-4\right)^2}{4n(n+2)(n-1)^2}\right], \tag{4.1}$$

where n=1.45846 @587.6nm is the refraction index of the fused silicon UV grade lens. Based on an f-number of 10.7, the spherical aberration of the focusing lens was estimated to be 0.037μm, which is negligible in comparison to the focal spot diameter ~10μm [Ireland, Yi 1974].

The beam quality was examined in air using the CCD beam profiling system after the focusing lens using a parameter of M^2 in reference to a Gaussian beam. The quality factor M^2, the waist size $W_0=W(z_0)$, and its location z_0 can be determined via measuring the spot size W(z) along the Z-axis (the beam propagating direction) on both sides of the

focusing spot and best fitting the results with three adjustable parameters $W_0=W(z_0)$, M^2, and z_0 [Siegman 1990] using:

$$W^2(z) = W_0^2 + \left(M^2\right)^2 \times \frac{\lambda^2}{\pi^2 \cdot W_0^2}\left(z - z_0\right)^2 . \tag{4.2}$$

The beam diameters is determined at the focal spot, defined as the full beam width at the e^{-2} of the peak irradiance, to be $2w_{0x} = 14\pm1\mu m$ horizontally and $2w_{0y} = 18\pm1\mu m$ vertically at 1064nm, which was verified by a knife-edge method [Siegman, Sasnett 1991]. The M_x^2 and M_y^2 factors in the transverse plane of the beam were determined to be 1.31 and 1.29, respectively as shown in Figure 4-2. It should be noted that for a non-Gaussian beam, the knife-edge method could not be directly used for this definition. The knife-edge method for beam spot size measurement and the M^2 definition of the beam quality is described in details in the Appendix I.

To acquire nanosecond pulses at 532, 266 and 213nm, the polarization cube was replaced with a harmonic generator unit. The unit contains an inverted telescope to produce a collimated beam with a reduced diameter of 5mm at 1064nm before entering three type I BBO crystals of $7\times7\times7mm^3$ size. The inverted telescope consists of a plano-convex lens with 100mm focusing length and a plano-concave lens with 75mm focusing length at about 25mm apart. The distance between the two lenses is fine tuned through a translator to collimate the output beam. The first BBO crystal was used to generate second harmonic pulses at 532nm, which can be reflected out of the unit by three harmonic separating mirrors to reduce the 1064nm component in the output beam to less than 0.2% in pulse energy. The first and the second BBO crystal for fourth harmonics

generation were used in ovens at a constant temperature of 80ºC. In later experiments, a KTP crystal was also used to generate the second harmonic pulse with significantly higher conversion efficiency (~50%) comparing with that of the BBO crystal (less than 20%) and simplicity of alignment since the KTP crystal does not require an oven. The 266 and 213nm pulses obtained from the 2nd and 3rd BBO crystals were separated from the 1064 and 532nm pulses using an ultraviolet prism. The measurement of the harmonic beam profiles at the focal point of an UV fused quartz plano-convex 75mm focal length lens with the CCD beam profiling system confirmed that the transverse profiles were close to Gaussian and symmetric in the x- and y-axes. Table 4-1 lists the diameter of the beam at the focal spot after the focusing lens, which is determined by the knife-edge method.

Fresh skin patches were obtained from the dorsal neck area of white domestic 6-month old pigs from the Brody School of Medicine at East Carolina University or adult pigs from a local abattoir (Washington Packing Inc., Washington, NC). The skin patches were stored within crushed ice (~4^{o}C) immediately after removal from the pig. The sample sizes of about 2×5cm^2 were prepared by removing the hair and subcutaneous tissue and warmed up to room temperature (~ 25°C) with 0.9% saline drops. The skin sample was clamped onto a holder with the epidermis facing the laser beam with translation in the horizontal direction by a stepping motor to ensure that each laser pulse was delivered on a fresh spot for experiments under a single-pulse condition. Before each experiment, the sample holder was carefully aligned along the laser beam axis with a precision translator so that the sample surface was at the beam waist. All measurements

were performed at room temperature within 30 hours of animal euthanasia. Furthermore, the skin sample surface was moistened with saline solution every 5 minutes to keep it from dehydrating during the experiment. A separate study of porcine skin samples showed that the absorption coefficient at 1064nm exhibit no change in the skin samples up to 30 hours postmortem under the identical storage conditions [Du, Hu 2001].

To quantitatively study the ablation process near the threshold, the spectrum of secondary radiation was measured between 300nm and 850nm from the ablated skin sample surface under the single-pulse condition by translating the sample during the ablation and lowering the pulse repetition rate to 0.2 to 1Hz to allow spectrum acquisition. The laser repetition rate can be lowered by selecting P25 for 0.2Hz or P5 for 1Hz, which turns the Q-switch on for every selected number of flash lamp excitations. For instance, while the flash lamp is firing at 5Hz, turning the Q-switch on for every 5 excitation will result in a 1Hz output and a 0.2Hz output requires 25 excitations. The secondary radiation was collected by a spherical lens of 100mm focal length and 38mm diameter into an optical fiber of 600μm diameter, which is connected to a spectrometer of 5nm resolution with a linear CCD array detector (S2000, Ocean Optics). The spectrometer was triggered externally, via a digital delay (DG535, Stanford Research Systems) by the Q-switched laser. The collected spectra are the result of integrating over 100ms starting 100ns before the peak of the laser pulse. The integration time of 100ms has been determined to be long enough to acquire all the possible laser induced radiation (LIR) lights while avoiding the influence from the subsequent pulse and reducing noise from ambient light. In order to reduce the influence of the ambient light to a minimum

level, all the lights has been turned off during the experiments with all windows were sealed.

Several operations have been performed sequentially for confirming the concurrence of the visually observed sparks and the spectral features from the secondary radiation spectra.

1. Set the laser repetition rate to 5Hz and then adjust the λ/2 plate to set the desired pulse energy measured through an optical power meter (AN/2, Ophire), record the energy with 30s averaging for 150 pulses.
2. Configure the QuickBasic program Step.bas/exe to run 100 steps at 50um per step.
3. Use the control software supplied by Ocean Optics to stop the CCD spectrometer and configure it to automatically save spectra on each trigger into a preset folder with names automatically given;
4. Set the laser repetition rate back to 0.2 (for early experiments that had to manually save spectra into files) or 1Hz (for later experiments with updated Ocean Optics software that can automatically save spectra with numbered file names);
5. Set the vertical position of the sample and proper horizontal moving direction of the step motor from the step motor controller;
6. Stop lasing using the external shutter push-button;
7. Start the spectrometer and step motor control program so they will run on hardware trigger from the digital delay generator;

8. Start lasing using the external shutter, count the number of sparks on the tissue surface visually using a mechanical counter;
9. Stop lasing using the external shuttle switch when the step motor controller counts 100 and beep;
10. For each pulse, compare the numbers of the visually observed sparks on the surface of the skin sample and of the spectral features of the spectrum files acquired in the PC;
11. Record the results for the pulse energy.

Two fast photodiode detectors were used to detect the time delay between the ablation pulse and the secondary radiation spectra through the digital oscilloscope. The ablation laser pulse was collected by the first photodiode detector through a beam splitter and proper neutral density filter set. A Czerny-Turner spectrophotometer of 0.05nm resolution (270MX, McPherson) replaced the CCD spectrometer and another photodiode was used to collect the secondary radiation at the 589nm line. The optical path lengths of the two detectors were maintained to be identical as well as the lengths of the BNC cables from the detectors to the oscilloscope.

4.1.2 Results

To quantitatively study the tissue ablation process near the threshold on an objective basis, the ablation was identified through spectral measurement of the secondary radiation that have been used for labeling optical breakdown in aqueous solutions [Sacchi 1991]. The secondary radiation spectra were acquired and analyzed between 300 and

800nm at each of the 4 ablating wavelengths near the ablation thresholds using the CCD spectrometer. The typical secondary radiation spectra consist of wide continuous spectra and many spectral peaks originated from the excitation of the different components inside tissue as shown in Figure 4-3. Two spectral lines at 589 and 656nm within the spectral window were initially identified as the signature of tissue ablation with 1064nm pulses because they are coincident with the weakest sparks visible to the darkroom adapted eyes. Using a Czerny-Turner spectrophotometer of 0.05nm resolution (270MX, McPherson), the peak positions of the lines were determined to be 589.0±0.5, 589.6±0.5, and 656.3±0.5nm, which can be associated with the electronic transitions in the neutral Sodium (Na) and Hydrogen atoms (H) given by NIST Standard Atomic Spectra Database (http://physics.nist.gov/cgi-bin/AtData/lines_form). The center position and line width of the lines are shown in Figure 4-6 with the Sodium double lines resolved at 589.00nm and 589.60nm. The Ocean Optics fiber optics spectrophotometer, however, only shows one line around 589nm due to its 3nm resolution. The McPherson spectrophotometer has been calibrated against Holmium lamp emission standard spectrum using a mechanical chopper and lock-in amplifier (SR810, Stanford Research Systems) as shown in Figure 4-4. The Na and H_α lines on the spectrophotometer were also calibrated using a sodium lamp and a hydrogen lamp as shown in Figure 4-5. Comparing with Figure 4-6, the uneven distributed Sodium double lines from LIR may be a result of population shift at the two Na atom energy levels due to the high temperature inside plasma.

The time-resolved LIR were also measured at 589.0nm via a photo multiplier detector at the exit window of the spectrophotometer. The LIR pulse is measured about 7ns after

the ablation pulse (peak to peak) and has pulse duration of about 18ns as shown in Figure 4-8. The 7ns delay is believed to be the plasma built-up time and the 18ns pulse duration of the LIR data is inline with the 16ns spontaneous emission lifetime.

Among the spectral lines obtained near the threshold, the narrow Na spectral lines near 589.6nm, which will be named the 589 line in later texts, was clearly distinguishable from the background when the tissue sample was ablated with 1064nm pulses, as well as at other wavelengths, and from the scattered and LIR light while the H_α line was weak and broad as shown in Figure 4-7. To determine the origin of the Na line at 589.6nm, the secondary radiation measurements was repeated with skin tissue samples moistened only with distilled water. Although the Na line became weaker as expected, the spectral line was observed clearly above the background with the same relation between the probability of line appearance and laser fluence near the ablation threshold as the one measured from saline treated skin samples. The occurrence of the 589 line has been examined to be within 5% of the occurrence of the sparks visually observed via naked eye, which is the common method to determine the probability of the plasma generation [Sacchi 1991; Kennedy, Boppart 1995]. Combining these results, the spectral line at 589nm was determined as the signature of the tissue ablation and it was found that the tissue ablation process near the threshold is of probabilistic nature at all four ablating wavelengths.

The ablation probability near the threshold was obtained by the ratio of the appearance of the secondary radiation line at 589nm to the laser pulses delivered to the sample under a single-pulse condition. In each measurement, 100 pulses were used to measure the

ablation probability P as a function of the laser fluence Φ at 1064, 532, 266 and 213nm by varying the pulse energy with a 5Hz repetition rate. To investigate the ablation mechanism operative at the four wavelengths, the ablation probability data have been studied using a statistical method of probit analysis. Figure 4-9

shows a plot of the probit of percentage probability P against the logarithm of the irradiance I. The probit Y is related to P as [Finney 1971]

$$P = \frac{1}{\sqrt{2\pi}} \int_{-\infty}^{Y} \exp\{\frac{1}{2}u^2\}du \tag{4.3}$$

and the irradiance I of the laser pulse is determined from the following equation

$$I = \frac{F}{\tau} = \frac{E}{\pi w_x w_y \tau} \tag{4.4}$$

where E is the pulse energy and τ is the pulse duration. From

it is clear that the percentage probability follows a normal distribution with respect to log(I). The experimental data at each of the four ablating wavelengths were fitted to a straight regression line to determine the slope, $\frac{dY}{d\log I}$, and ablation thresholds in pulse energy W_{th}, laser fluence Φ_{th} and electric field strength $\mathcal{E}_{th}$ at probability 10% and 90% (see Table 4-1).

To further analyze the ablation mechanism, the ablation probability P is also plotted in Figure 4-10 as a function of the inverse of the electric field of the laser pulse, $1/\mathcal{E}$, on a semi-log scale. The average rms electric field strength $\mathcal{E}$ is calculated from $\varepsilon = \sqrt{\frac{\Phi}{\tau c n \varepsilon_0}}$, where c is the speed of light and ε_0 is the permittivity in vacuum and the refractive index of the hydrated skin n is assumed to be 1.33. The dependence of the probability P on the electric field $\mathcal{E}$ was fitted to an equation $P = P_0 \exp(-K^2/\mathcal{E}^2)$, where P_0 and K are fitting parameters.

Table 4-1 Focal Spot Diameters and Ablation Thresholds

Ablation Wavelength λ	1064nm	532nm	266nm	213nm
$2w_{0x}$ (μm)	14	25	20	20
$2w_{0y}$ (μm)	18	25	20	20
$\frac{dY}{d\log I}$ {1}	5.23	9.26	6.02	7.08
F_{th} (J/cm^2) @ P =90% {1}	129	35.8	14.3	1.6
W_{th} @ P=90% {1}	0.256mJ	0.176mJ	44.9μJ	5.14μJ
E_{th} (V/m) @ P =90% {1}	1.68×10^8	7.72×10^7	5.38×10^7	1.96×10^7
F_{th} (J/cm^2) @ P =10% {1}	41.8	18.9	5.36	0.711
K (V/m)	1.06×10^9	6.58×10^8	3.88×10^8	1.43×10^8
α (cm^{-1}) {2}	5	1	~ 600	N/A

{1} obtained from the regression lines in Figure 4-10.
{2} absorption coefficients of skin epidermis are from [van Gemert and Welch 1989]

The concurrence of the secondary radiation spectral line at 589nm with the tissue ablation was verified at laser fluences near the 90% ablation threshold by the measurement of ablation depth in the porcine skin at each of the four ablating wavelength under a multiple-pulse condition. On each sample, a series of six or seven lines was

ablated at different pulse energies with a 1-mm separation between the lines translated vertically through a translator. The skin sample was translated along the x-axis at a pulse repetition rate of 10Hz. The translation speed was set to obtain the laser pulse number per spot, N, as 90 for ablation at 1064 and 532nm and as 45 for 266 and 213nm so that the ablation depth at the ultraviolet wavelengths would not exceed the full thickness of the skin at maximum laser fluence. Ablated samples were immediately fixed in Bouin's fixative for 12 hours after ablation. Preparation of the sample involves dehydration and clearing of the tissue, and infiltrating the tissue with paraffin. Each of these steps involves precise timing in order to obtain quality sections and reduce distortion of the ablation cuts [Cariveau and East Carolina University. Dept. of Biology. 2000]. Once the tissue is infiltrated with paraffin, then it is embedded in a paraffin block for sectioning purposes. For sectioning, a microtome (2030 Biocut, Reichert-Jung) is used to section 10mm sections of skin. Once the sections are obtained, they are placed on slides and stained with hemotoxylin and eosin to show better contrast between the epidermis and subsequent layers of the skin. Ablation depth of the tissue sections on slides was measured under a microscope as an average from 40 to 60 sections. The average and standard deviation of the ablation depth data were determined from histological sections prepared from the ablated tissue samples at each wavelength. One ablation curve was obtained for each sample at ablating wavelengths in which the ablation depth per pulse is plotted as a function of laser fluence, as shown in Figure 4-11.

4.2 Spot Size Dependence of the Ablation Thresholds

By combining the variations of the incident beam diameter and focal length of the lens, the focusing spot size can be changed and the spot size dependence of the ablation irradiance threshold was therefore studied. The experiment setup is similar to the ablation probability measurement using a 75mm focusing lens at 1064nm described in the previous section and shown in Figure 4-1. The Q-switched Nd:YAG laser was used to generate pulses of 100mJ energy and 12ns duration at the fundamental wavelength of 1064nm. The transverse profile of the laser beam is non-Gaussian with a 0.6mrad divergence and 95% fitting to Gaussian distribution in the far field. Different plano-convex lens of 75, 125, 175, 200, 300, 500, and 700mm focal lengths were employed to obtain different diameter at the focus for the pulses at 1064nm. An additional invert telescope with a 100mm plano-convex lens and a 50mm plano-concave lens was used to achieve a 4mm diameter collimated beam. Combining the small beam diameter and the 500mm and 700mm lens, two additional large spot sizes were obtained. The Spiricon CCD beam profiling system was used to examine the beam profiles after each of the five lenses. The M_x^2 and M_y^2 in the transverse plane of the beam [Siegman 1990] were determined from the dependence of the beam radius on the axial positions and the focal spot sizes was obtained and verified by the knife-edge method. The M^2 parameters and the diameters of the beam for each focusing lens at the focal spot are listed in Table 4-2.

Table 4-2 Ablation thresholds at different focal spot sizes.

Focal Length (mm)	Diameter D (mm)	Radius W (μm)	$F_{th}10\%$ (J/cm^2)	$F_{th}90\%$ (J/cm^2)	$\frac{dY}{d \log I}$
75	7.0	5	41.8	129	4.81
125	7.0	8	29.7	120.6	4.67
175	7.0	11	15.75	54.63	4.95
200	7.0	13	50.1	167.8	5.31
300	7.0	18	35.6	149.4	4.51
500	7.0	56	17.7	28.2	5.48
700	7.0	83	16.2	34.4	4.99
500 small D	4.0	125	13.5	20.1	17.93
700 small D	4.0	163	5.58	20.25	5.62

Fresh porcine skin patches were obtained from sacrificed pigs and the procedures of storage and preparation were similar to those outlined in the previous section. Thin skin samples with thickness ranging from 150μm to 800μm were sectioned from prepared patches with an intact epidermis by using a cryostat microtome (Ames Lab-tek) to obtain dermis sections at -18°C. After warming up to the room temperature in 0.9% saline, a sample was clamped onto a holder with the epidermis facing the incident laser beam. Special care was taken to make the sample flat on the holder without excessive stretching. A 11mm diameter in the middle of the holder behind the sample allows the measuring the transmittance to monitor the changes in the sample thickness. A continues wave He-Ne laser of 633nm wavelength was aligned to overlap coaxially with the

1064nm beam and used as a marker to indicate the ablation pulse position on the surface of the skin sample. The He-Ne beam was collimated to a different beam diameter so that the focus overlaps with that of the 1064nm beam after passing through the same focusing lens. Before each experiment, the sample holder was carefully positioned to ensure the sample surface was at the beam waist and perpendicular to the beam axis.

Figure 4-12 plots the ablation probit as a function of laser irradiance for the seven spot sizes. The ablation probabilities are plotted as a function of the reciprocal laser rms electric field as shown in Figure 4-13.

4.3 Optical Measurement of Ablation Depth

The ablation threshold determined in section 4.2 is based on the laser-induced radiation from the surface of the skin. Further experiments were conducted to determine the ablation depth per pulse to independently verify the ablation of tissue near the optically determined thresholds. The histology measurement of ablation depth is very time consuming such that it takes weeks to obtain the depth results. In addition, the histology procedures are multi-step processes and prone to artifacts for skin tissues with very shallow depths of ablation near the threshold. Therefore, an optical transmission technique was developed to measure the ablation depth per pulse that gives ablation depth results much faster. This method will also enable one to compare the ablation rate between epidermis and dermis of the skin.

For ablation depth measurements, the ablation depth per pulse was determined by dividing the thickness D of the tissue sample by the number N of pulses needed to ablated

a thin skin tissue samples though its thickness. To accurately determine N, the collimated transmission signal of the He-Ne beam was measured after each pulse to establish if the skin sample was "drilled" through the full thickness by the ablating beam. Because of the strong scattering nature of the skin tissue to the ultraviolet, visible, and infrared light, this method provides a highly sensitive approach for measuring the ablation depth. The collimated transmission of the He-Ne beam was spatially separated out from the scattering light with a collimating lens placed 200mm behind the focus and another lens to focus the beam into a 2mm pinhole before a photodiode detector. The transmitted ablating beam was filtered out by either the two BK7 lenses behind the tissue sample for their high absorption in the ultraviolet or interference filters at 532 and 1064nm. The He-Ne beam output was modulated by a chopper working at 1KHz. The transmitted signal was sent to a lock-in amplifier (SR850, Stanford Research) at the modulated frequency. The output of the lock-in amplifier was then digitized and the data acquisition by a PC was synchronized with the trigger pulses from the Nd:YAG laser controller. At each level of pulse energy, 15 measurements on two skin samples were conducted to obtain an average value in the ablation depth per pulse. A schematic of the experimental setup for ablation depth measurements is presented in Figure 4-14.

During the ablation process, the coaxial He-Ne beam was scattered by the tissue so the transmission of the beam measured by the photodiode is near zero, while there were scattered photons reaching the detector after the tissue. When the ablation beam "drilled" through the tissue to leave a clearance hole, most of the photons in the He-Ne beam reached the detector without being scattered by the tissue. Therefore, the transmission of

the He-Ne beam had a steep increase, which will be detected by the computer when sensing the output signal of the photodiode passing a preset trigger value and recorded the number of pulses needed to drill through the sample. Figure 4-15 shows a typical measurement that drills through the dermis section in 14 pulses. The laser pulse train started ablating the tissue section at the pulse number 1280. After a few pulses, the thickness at the ablation location decreased and transmission of the He-Ne beam started to increase as shown in the curve before "a". From "a" to "b", the laser drilled a clear hole on the tissue section so a significant jump in transmission could be observed. Sometimes, the first hole may be small in diameter, possible due to higher intensity in the center of the beam, so the transmitted light may be blocked again by the debris from the subsequent pulses as shown from "b" to "c". A warning signal was given and laser pulse train was stopped using the laser remote shutter at "c." A new pulse train started at "d" after translating the sample to a new location. The number of pulses needed to ablate the section was therefore defined as from the beginning of the pulse to "b." After the measurement, the tissue sections were examined under the microscope to verify that all the holes were through. The ablation depth per pulse as a function of laser irradiance at the seven spot sizes is shown in Figure 4-16. The difference ablation rates between epidermis and dermis sections are shown in Figure 4-17 at 1064, 532, 266, and 213nm, respectively.

4.4 Porcine Skin Dermis Attenuation Coefficient Measurement

The skin patches were removed from the animals immediately after death and stored in crushed ice (~4ºC) until the dermis samples are excised from the skin. The absorbance

measurements were performed within 36 hours postmortem. To prepare the skin for sectioning, the skin patches were cut into sample sizes of about 2cm by 2cm with the hair and subcutaneous tissue removed. For absorbance measurement in the UV region, the section thickness needs to be in the neighborhood of 30μm to keep the absorbance within the scale of the spectrophotometer because the dermis strongly absorbs in this spectral region. To obtain a thin contiguous dermis section of uniform thickness, a microtome-cryostat was used to section the frozen cornea at –18ºC. The skin sample patches were frozen in the cryostat for 20 minutes or longer before sectioning. The subcutaneous tissue including the fat layer was removed until a uniform section from the dermis is obtained. The dermis section was then stored in 0.9% saline solution and kept refrigerated until measuring, when it would be transferred to a sample holder.

The absorbance measurement using a spectrophotometer and the calibration procedures are described in detail by Lembares [Lembares 1997]. Two rectangular optical windows made of UV grade fused silica glass (Type 7940, Corning Inc.) were used as a sample holder to keep the thin dermis section intact and total absorbance low for the UV absorbance measurements. The sample holder has a total thickness of 12mm and a very low thermal expansion coefficient that helps to protect the dermis section in the course of thawing and transferring to the spectrophotometer. The absorbance of the sample holder increases slowly as the wavelength decreases in the far ultraviolet, which was measured to be less than 0.01 at 260nm and 0.011 at 190nm after surface reflection contribution being deducted [Lembares 1997].

Before the dermis section had been transferred to the sample holder, the optical windows were cleaned thoroughly with acetone. The cornea section were sandwiched between the two optical windows and clamped by a holder. This helps to prevent dehydration of the section during the absorbance measurement and to remove any trapped air bobbles in the section. Two blackened metal plates with an aperture of 4mm in diameter for each were used at the front and back surface of the sample holder to collimated the incident and transmitted light beams.

The absorbance measurement of the dermis sections in the ultraviolet region from 400nm to 200 nm was carried out at room temperature with a dual beam UV-VIS-IR spectrophotometer (Model Cary 17D, Varian Associates). The absorbance reading (A) obtained from the spectrophotometer is the common logarithmic ratio of the incident light on the sample I_0 (measured from the reference beam in the reference chamber) and the transmitted light through the section I (from the sample beam through the sample chamber),

$$A = \log_{10}\left(I_0 / I\right). \tag{4.5}$$

The spectrophotometer can be used to measure absorbance from 0.0 to 3.0 in 5 scales between 2600 and 190nm in wavelength. The UV absorbance reading was calibrated using a standard Neutral Density filter set from CVI Corp. at optical density of 0.1, 0.5, and 1.0. The wavelength reading was calibrated using a standard Holmium Oxide filter (CVI Laser Optics Spectrophotometer Calibration Filter Sets, Holmium Oxide Filter: CFS-HOF) as shown in Figure 4-18. Both the optical density and the wavelength calibration results were found within the manufacture's specifications. The output signal

from the spectrophotometer is an analog DC signal, which was digitized via an A/D converter (ADC500, Computer Board) and saved to a personal computer with 200 times average for each wavelength reading.

The sample holder with the dermis section was placed in the sample chamber while the reference chamber only contained the two identical apertures of 4mm in diameter. When the absorbance reading reached the about one third of the full scale for a decreasing reading or about two thirds of the full scale for an increasing reading, the scale was changed accordingly to accommodate the level of absorption with the best sensitivity. The different segments of the same absorbance measurement were overlapped to ensure accurate reading over the whole spectrum. The process was repeated until the minimum wavelength of 200nm was reached. Then the difference between the absorbance reading and the absorbance of the sample holder without the dermis sample was plotted against the wavelength.

The thickness of the dermis section was determined, after the absorbance measurement, through the measurement of the thickness difference of the sample holder with and without the dermis sample at room temperature using a micrometer of 3μm (0.0001 inch) resolution. The micrometer has a ratchet stop mechanism that enables a consistent application of measuring pressure for each measurement. Three measurements of thickness for each sample had been conducted and the average of the measurements were used as given in Figure 4-19.

In UV region, the absorption and scattering data of skin tissue are given in literature only to about 250nm from visible and inferred [van Gemert, Jacques 1989]. The tissue absorption coefficient therefore has to be estimated based on the transmittance measurements.

$$I = I_0 e^{-(\mu_a + \mu_s)d}, \tag{4.6}$$

where d is the thickness of the tissue section. If further assuming the scattering property of the tissue is only related to the wavelength through the Rayleigh scattering, the absorption coefficient μ_a can therefore been roughly estimated at 213nm to be 3400cm^{-1} from the transmittance at 213nm and 266nm with the experimentally obtained μ_a and μ_s at 266nm.

4.5 Discussion

A large body of knowledge has been obtained on tissue ablation by nanosecond laser pulses over the last two decades [Anderson and Parrish 1983; Fujimoto, Lin 1985; Srinivasan 1986; Stern, Schoenlein 1989; Kitai, Popkov 1991; Oraevsky, Esenaliev 1992; Itzkan, Albagli 1995; Kennedy 1995; Vogel, Nahen 1996]. Among the observed phenomena identified with tissue ablation by nanosecond laser pulses, the presence of an irradiance threshold and its variation as a function of laser parameters and tissue optical properties are of the most importance. The formations of shock waves, acoustic transients, and bubbles have also been documented [Oraevsky, Esenaliev 1992]. Understanding the fundamental mechanisms in laser tissue ablation is essential to improve clinical laser applications by reducing collateral damage and laser pulse energy

requirement. Numerous models have been proposed to understand the above phenomena, which may be separated into three major types according to their proposed pathways leading to tissue ablation. They are namely: the photothermal models represented by the selective photothermolysis [Anderson and Parrish 1983] and photomechanical models [Albagli, Banish 1994; Albagli, Dark 1994; Albagli, Dark 1994; Albagli, Perelman 1994]; the photochemical model [Srinivasan 1986; Srinivasan, Braren 1986; Pettit and Sauerbrey 1993; Sentrayan, Jr. 1998]; and the plasma-medicated models [Kennedy 1995; Kennedy, Boppart 1995; Vogel, Nahen 1996]. A key difference among these models is whether there is laser-induced plasma formation during the ablation. It should be note that three models are not compatible with each other.

The typical laser irradiance threshold range predicted by photochemical model is around $10^7 W/cm^2$ [Pettit and Sauerbrey 1993], which is two to three orders of magnitude less than what had been observed in the experiment at 213nm and 266nm. In addition, any appreciable quantum yields of photochemical reactions in proteins and other biopolymers can only be expected at irradiation wavelengths shorter than 250nm [Oraevsky, Esenaliev 1992]. Therefore, it has become clear that the photochemical model is of limited significance to explain the experimental data for ablation with ultraviolet pulses. Variations from the selective photothermolysis model have been proposed to understand the mechanism of soft tissue ablation by nanosecond pulses in the spectral region from ultraviolet to near-infrared [Izatt, Albagli 1991; Oraevsky, Esenaliev 1992]. It was suggested that the overheating occurs at various chromophores in tissues through radiationless relaxation of the absorbed light energy, or thermalization, which

induces acoustic transient and/or explosive boiling of the water content in tissues and significantly lowers the threshold energy of ablation calculated for homogeneous absorption. A thermoelastic model further takes into account the inertial confinement as a result of rapid heating [Izatt, Albagli 1991; Albagli, Perelman 1994]. The ablation threshold predicted in the above models shows monochromic dependence on the tissue absorption, which is correlated to the wavelength dependence measured experimentally. However, the assumption of acoustical transient and/or water boiling as the cause of tissue ablation underpinned by the above models fail to explain the experimentally observed flash and shock waves onsite as well as on the probabilistic nature of the ablation at all four wavelengths at which the skin tissue exhibits large variation in light absorption.

The experimental measurement of the probabilistic behavior of the plasma generation near the threshold requires a signature clearly identifies the occurrence of the optical breakdown. In addition to the commonly use of visual observing of the flash from the LIR of plasma [Sacchi 1991; Kennedy, Boppart 1995], the detection of the shockwaves using acoustic transducers was also been reported [Vogel, Nahen 1996]. The visual observing method is subject to human error both from the difference of observer's eyesight and exhaustion after looking at the ablation site for a long period since the probability study requiring a large number of measurements. The acoustic measurement is also subject to environment noises coming from different origins. The secondary radiation spectra from the fresh porcine skin samples (Figure 4-5) were analyzed to establish the spectral line at 589nm radiated from the ablated tissue as the signature of

tissue ablation at 1064, 532, 266 and 213nm. The narrow spectra line at 589nm from the Sodium atoms in the tissue distinguishes itself clearly from background and/or LIR light and can be enhanced by treating the tissue with 0.9% saline solution. By identifying the signature spectral line, one was able to determine unequivocally the probabilistic nature of the skin tissue ablation process and quantitatively measure the ablation probability with nanosecond laser pulses at the four wavelengths.

The concurrence of the secondary radiation spectral line at 589nm line with tissue ablation was verified at laser fluences near the 90% ablation threshold by the histology measurement of ablation depth as shown in Figure 4-11. To facilitate the comparison between the two types of experimental results, the laser fluence thresholds at P = 90% determined from the probability measurements are marked by dash and dash-dot lines in Figure 4-11. While the probability and ablation depth measurements were conducted under different conditions, single-pulse versus multi-pulse in different skin samples, it has been observed that tissue ablation occurs near the laser fluence thresholds measured at 90% probability from the secondary radiation. Moreover, non-zero ablation depth at fluence below the 90% probability line shown in Figure 4-11 also indicates ablation of tissue occurs with the occurrence of the LIR below the threshold. Hence, the ablation depth measurement directly confirms that the secondary radiation is a result of tissue ablation for all four wavelengths.

In addition to measurements performed for spot size of 10μm at 532nm, 266nm, and 213nm, the ablation probability P near the threshold was also measured as a function of the reciprocal of laser rms electrical fiels at different spot sizes from 10 to 163μm in

diameter with 12ns pulses at 1064nm, which is shown in Figure 4-13. Similar probabilistic behaviors of the ablation probability have been identified and the 90% ablation thresholds have been confirmed using a optical probe transmission measurement of ablation depth as shown in Figure 4-16.

A statistical method of probit analysis was employed to help the investigation of the ablation mechanisms operative in the ablation process of different spot sizes and compared with the results at different wavelengths. In the probit transformation, the probit Y of the proportion P is defined as the abscissa which corresponds to a probability P in a normal distribution with mean 5 and variance 1, as show in Eq. (4.3). In probit analysis, the normal sigmoid curve of the probability P is transformed into a straight line in term of probit Y. In the ablation probability measurements, if the probit can be fit into a straight line, it indicates that the probability as a function of laser irradiance is distributed normal.

Furthermore, the difference between the slops of different sets of data indicates different mechanisms governing those processes. In other words, if near parallel lines are found for different sets of data, there is the same mechanism operative in these processes but with different sensitivity indicated by the distances between the parallel lines. From the probit analysis of ablation probability data shown in Figure 4-9 and Figure 4-12, it has been shown clearly that the tissue ablation processes near the threshold at different wavelengths and spot sizes can be consistently fit into linear regression lines, which indicates that they are characterized by similar normal distributions in their ablation probability frequency. In Figure 4-9, the slopes of the regression lines fitted to the probit

data at the four wavelengths are similar but significant differences are observed: ranges from 5.63 at 1064nm to 9.26 at 532nm. This difference points out that the operative mechanism in the skin tissue ablation by nanosecond laser pulses might come from several competing processes, which contribute differently at different wavelengths.

The characteristics of the skin tissue ablation processes extracted from the quantitative measurements at four laser wavelengths is remarkable considering that the linear absorption coefficient of the skin at the ablating wavelength of 1064nm is several orders of magnitude smaller than at 266nm [van Gemert, Jacques 1989] and 213nm (estimated from the transmittance measurement). When the absorption coefficient is the same for the ablation probability measured at 1064nm for different spot sizes, however, the regression lines are relatively parallel to each other with slopes ranging from 4.81 to 5.63 as shown in Table 4-2 (the 125μm/500mmSmallD data set has been neglected due to insufficient number of measurements in this set.) Given the relatively large variation of the tissue sample, these lines are believed can be treated as parallel, which indicates the same mechanisms governing the process.

The logarithm of the breakdown probability measured at the four ablating wavelengths, shown in Figure 4-10, and at the seven different spot sizes shown in Figure 4-13, all have displayed a parabolic dependence on the reciprocal of the laser rms electric field and thus fitted into $P=P_0\exp(-K^2/\mathcal{E}^2)$. An important aspect of the optical breakdown is the probabilistic character of both the extrinsic and intrinsic mechanisms. The localized thermal ionization is called extrinsic breakdown mechanism, since its characteristics are

largely determined by the inclusions in tissue such as chromophores. Therefore, the probability should not have a systematic dependence on the input laser field as indicated by experimental results due to the random spatial distribution of the chromophores.

A plasma-mediated ablation model has been used to understand the ocular tissue ablation and water breakdown by visible and near-infrared nanosecond laser pulses to which the tissues or water has little absorption [Fujimoto, Lin 1985; Stern, Schoenlein 1989; Kennedy 1995; Vogel, Nahen 1996]. The probabilistic nature of the skin ablation process near the threshold by the nanosecond laser pulses at 1064, 532, 266 and 213nm is very typical of optical breakdown in condensed matters caused by short laser pulse [Bloembergen 1974; Docchio, Sacchi 1986; Sacchi 1991]. The breakdown process can be analyzed through a rate equation on the time dependence of the free electron density $\rho(t)$ under the influence of the optical radiation field [Bloembergen 1974; Kennedy 1995]. Cascade ionization has been shown that is the dominant mechanism governing the optical breakdown process in water and ocular solutions [Docchio, Sacchi 1986; Sacchi 1991; Kennedy 1995; Kennedy, Boppart 1995; Vogel, Nahen 1996]. Electrons gain energy during cascade ionization through either lucky ballistic or lucky drift motions, which are distinguished by the different laser electrical field dependence of the ionization probability [Ridley 1983]. Specifically, the Shockley-like lucky-ballistic mode $P\sim\exp(-K/\mathcal{E})$ dominate the ionization process at low field and the lucky-drift mode $P\sim\exp(-K^2/\mathcal{E}^2)$ dominants at high field.

Therefore, the systematic ablation probability dependence on laser electric field $P = P_0\exp(-K^2/\mathcal{E}^2)$, shown in Figure 4-10, suggests impact ionization is the dominance mechanism governing tissue ablation process in the wide spectral range from near-infrared to ultraviolet. Additionally, using the parameters that are relevant to the skin and the laser fluence threshold obtained from Table 4-1, that the cascade ionization rate $\eta\rho(t)$ was determined to be much greater than the multiphoton ionization rate $(\frac{\partial\rho(t)}{\partial t})_m$, i.e. by nearly 5 orders of magnitude, at the ablation threshold for the 14ns pulses at 1064nm because of the low irradiance required at the threshold of skin ablation. A similar conclusion was drawn to the skin tissue ablation by pulses at 532nm. Therefore, the plasma-mediated model in which the plasma is induced through cascade ionization might explain the tissue ablation processes at these two wavelengths.

For tissue ablation at 266 and 213nm where the absorption of laser radiation by the skin tissue becomes significantly large as shown in Table 4-1, the measured ablation thresholds are significantly lower than that of at 1064 and 532nm. Based on the assumption of negligible absorption, however, the existing plasma-mediated model predicts the thresholds should increase as the decrease of the ablation wavelength shown in Figure 3-9. From measurement of the absorbance of two porcine dermis samples of thickness between 50 and 100μm, obtained with a cryostat microtome as described in section 4-4, it was found that the attenuation coefficient doubles as the wavelength decreases from 260 to 220nm in comparison to a modest increase of about 40% from 400 to 260nm. These results suggest that possible tissue absorption influence on the ablation

threshold without modifying the probabilistic nature of the ablation process near the threshold.

Chapter 3 shows a new model that includes contribution from the localized thermal ionization of the chromophores in skin tissue due to absorption the ablation thresholds during plasma formation. In this theory, cascade ionization is still the dominant ionization pathway when there are sufficient seed electrons in the illuminated region. The seed electrons come from three origins: pre-existing, multiphoton ionization, and thermal ionization. In normal tissue, pre-existing electrons are very rarely found and multiphoton ionization is the commonly considered channel for seed electron generation. The localized thermal ionization has usually been neglected due to insufficient temperature rise from weak light absorption in homogeneous mediums studied in the previous plasma models. In biological tissues, i.e. skin tissue, the combination of strong and localized absorption in the chromophores leads to rapid local temperature rise that provides the seed electron necessary for the development of cascade ionization. It has been shown that under these experimental condition, the localized thermal ionization surpasses the multiphoton ionization and significantly affects the ablation thresholds. In Figure 3-9, it is shown that this model is most close to the thresholds measured in the experiments and has the same wavelength dependence. Adding the localized thermal ionization pathway to the rate equation not only successfully explained the ablation threshold dependence on the tissue absorption, it also explained the probabilistic behavior of the ablation process through the dominant of the cascade ionization once there are sufficient seed electrons in the illuminated region.

Furthermore, the localized thermal ionization model predicts that there is no significant spot size dependence, which is confirmed by both of the experimental results shown in Table 4-2 and in literature [Noack and Vogel 1999]. A weak ablation threshold dependence on the focal spot size also suggests a possibility that the ablation of pigments and/or chromorphores with a large variation in optical absorption is possible using nanosecond laser pulses at a single wavelength in a tightly focused beam.

Chapter 4 Figures

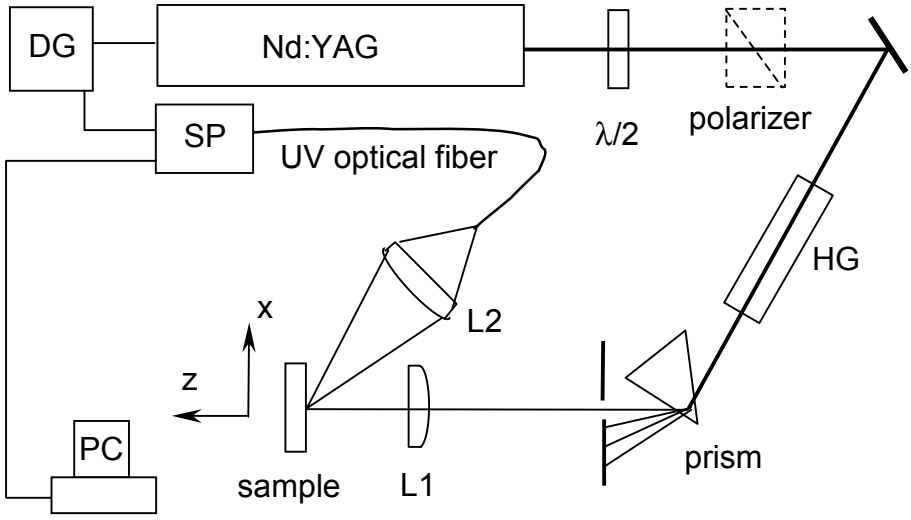

Figure 4-1 Schematics of the ablation threshold measurement system setup. DG: Digital delay and pulse generator; SP: Ocean Optics Spectrophotometer; HG: Harmonic generating assembly; L1: Plano-convex UV fused silicon focusing lens f=75mm; L2: Plano-convex BK7 lens with 50mm diameter and f=200mm used for collect laser induced secondary radiation.

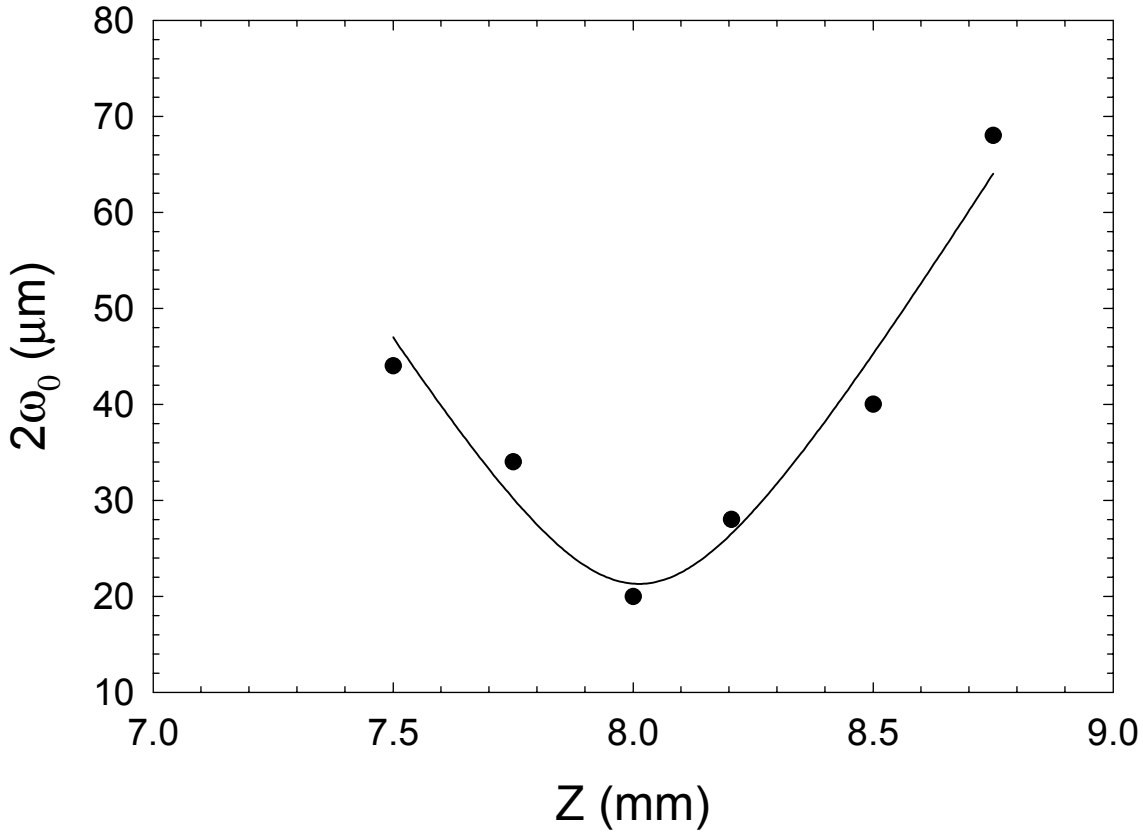

Figure 4-2 M^2 measurement of focusing spot size of a 75mm focal length plano-convex lens at 1064nm by knife-edge method. Q-switch delay: 290μs; pulse duration: 18ns; pulse energy: 0.8mJ (L75P4A.jnb.)

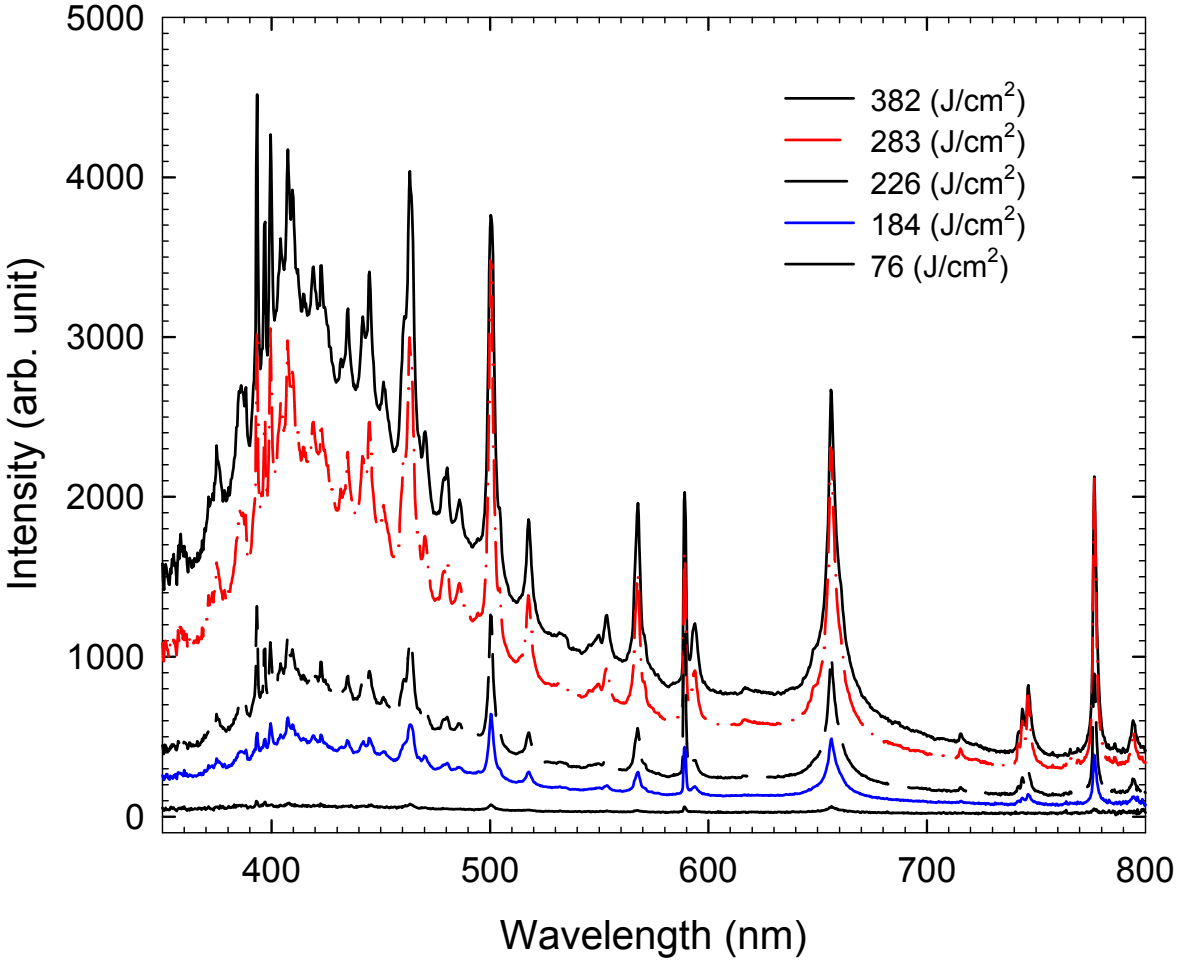

Figure 4-3 Typical secondary radiation spectra from porcine skin tissue samples ablated at 1064nm and measured by the CCD spectrophotometer at different ablation pulse energy (Fluores.jnb.)

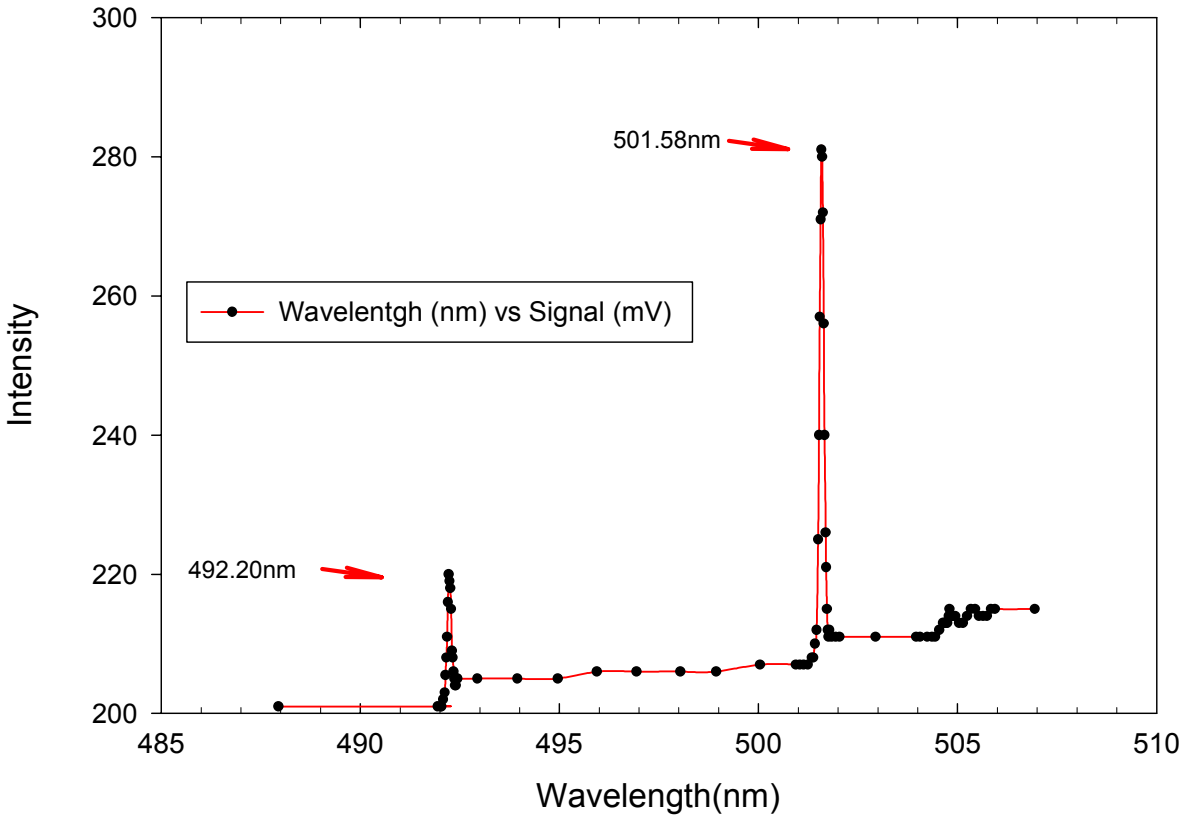

Figure 4-4 McPherson spectrophotometer wavelength calibration using Holmium lamp at 492.193nm and 501.567nm. The value on the figure is the measured value (990527_Mcpherson.jnb.)

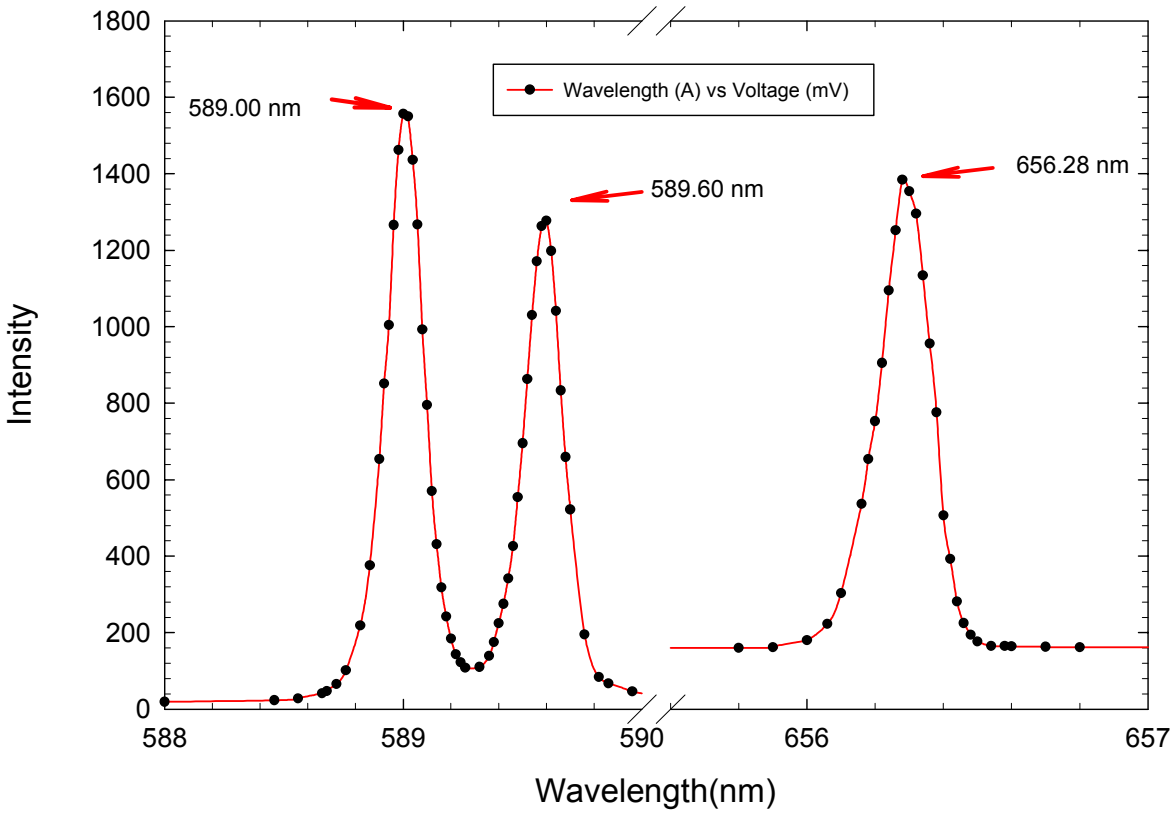

Figure 4-5 Typical spectral lines detected by the McPherson spectrophotometer for Hα at 656.282nm using a Hydrogen lamp and Na double lines at 588.995nm and 589.592nm using a Sodium lamp (990527_McPherson_Calibration.jnb.)

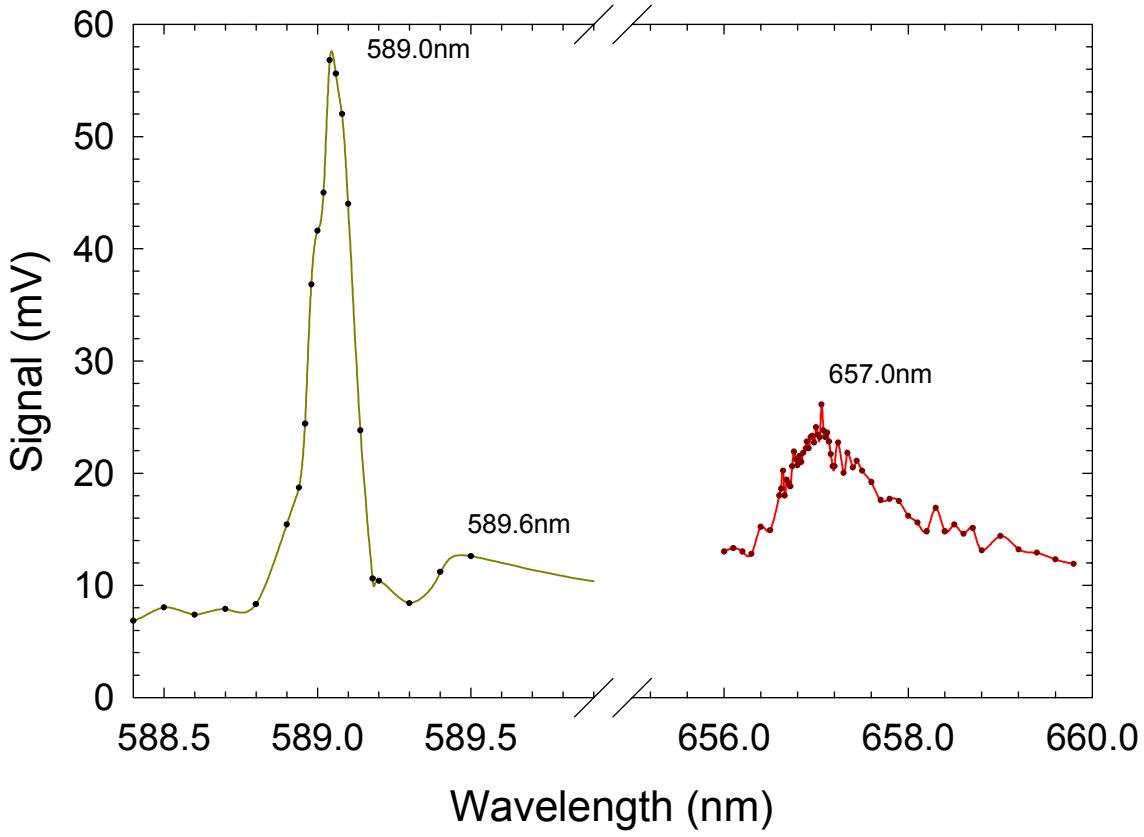

Figure 4-6 Tissue ablation secondary radiation spectra measured via the McPherson spectrophotometer at 656.8nm for hydrogen and 589.0nm and 589.6nm for sodium. A Q-switched Nd:YAG laser ablating at 1064nm with pulse duration τ_p=12ns (FWHM), pulse energy E_p=8mJ, Q-Switch delay: 260µs, f=75mm fused silicon plano-convex lens (990507.jnb 990602.jnb.)

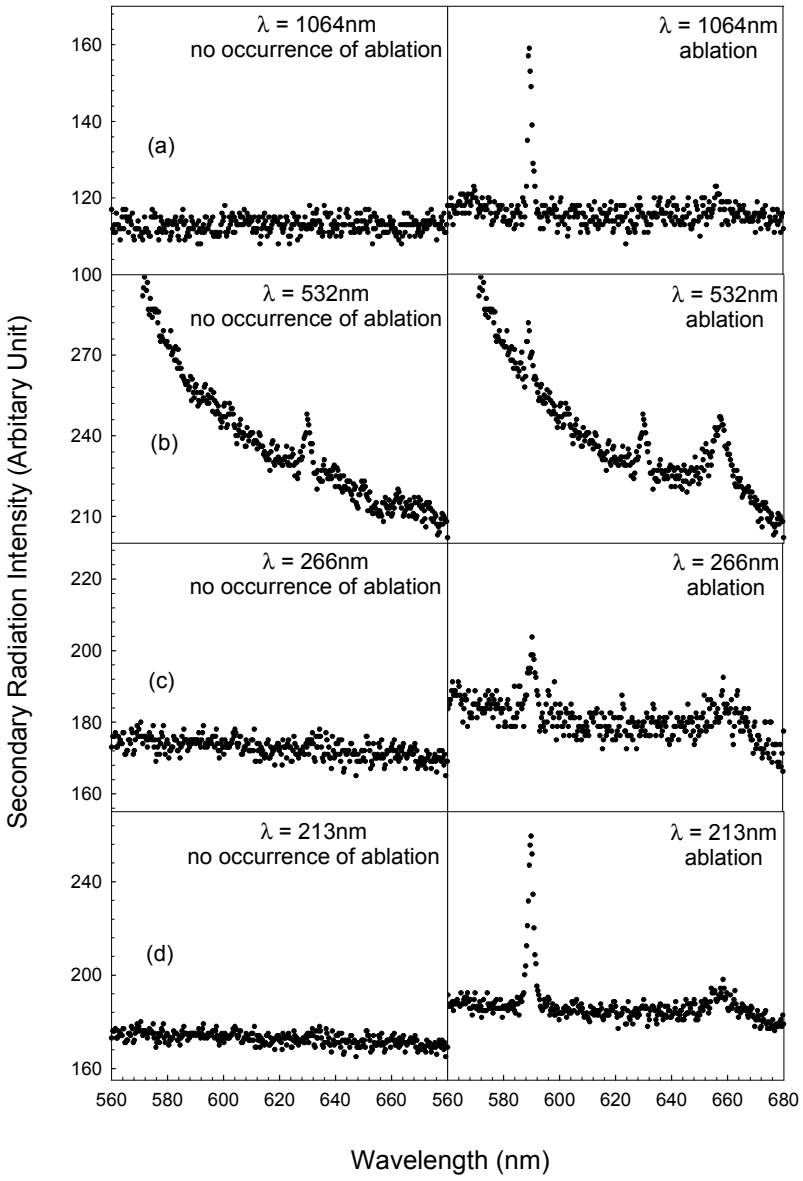

Figure 4-7 Comparison of concurrence of ablation and the spectra lines using typical secondary radiation spectra from ablated porcine skin tissue samples. Each pair of diagrams was obtained at the same laser fluence near the 90% ablation probability (ablation_spetrum.jnb.)

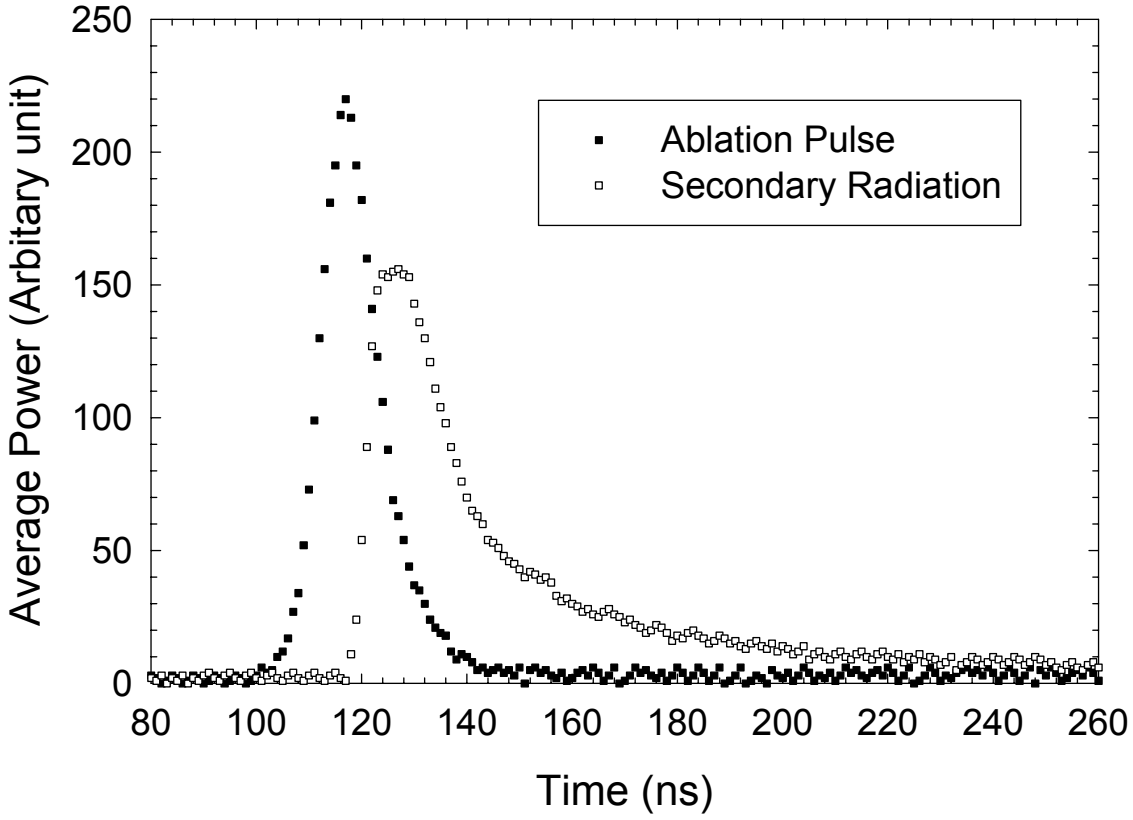

Figure 4-8 Time-resolved measurement of secondary radiation pulse with respect to the ablation pulse. Pulse duration τ_p=12ns (FWHM), pulse energy E_p=2mJ, Q-Switch delay: 260μs, f=75mm fused silicon plano-convex lens. Photodiode rise time: 1ns, digital oscilloscope bandwidth: 500MHz (Time.jnb.)

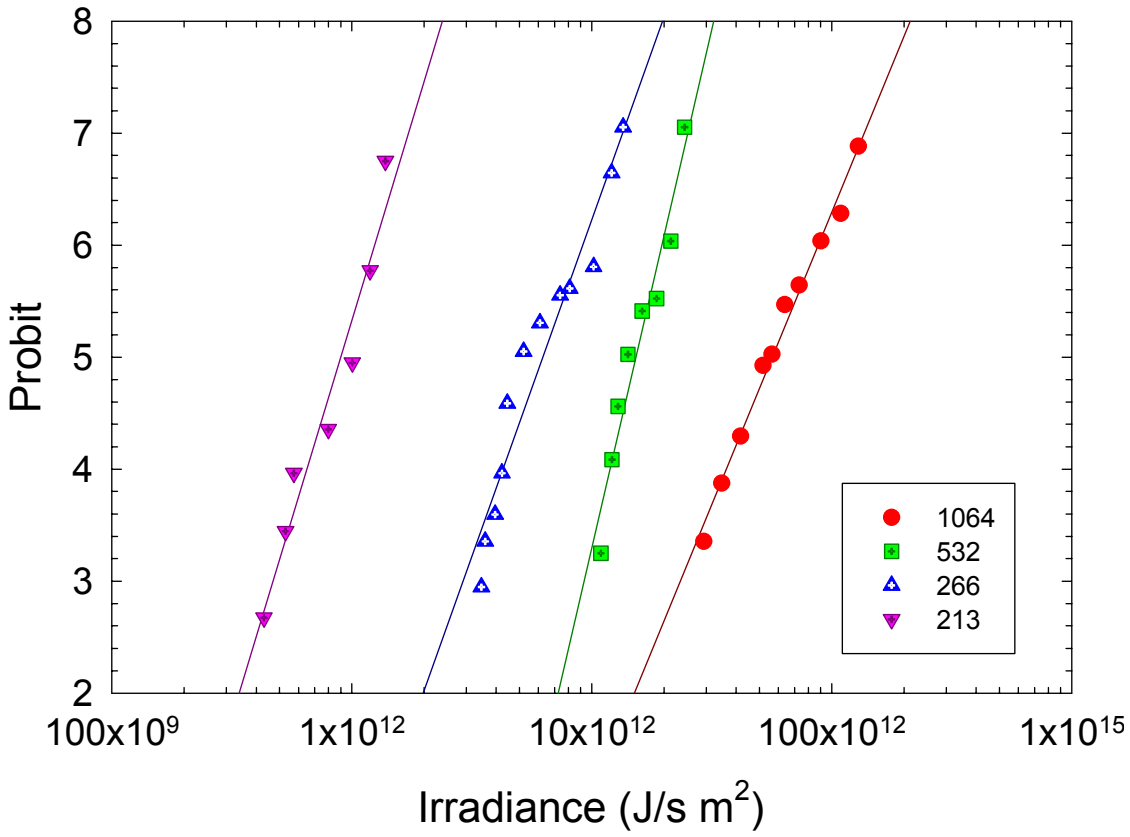

Figure 4-9 Probit of the ablation probability as a function of laser irradiance I at different ablation wavelengths. Each probability data point was obtained with 100 pulses at the same laser fluence. Straight lines are regression lines for each set of data following an equation $Y=\alpha+\beta\log(I)$, where a and b are fitting parameters (Ablation_Probability.jnb.)

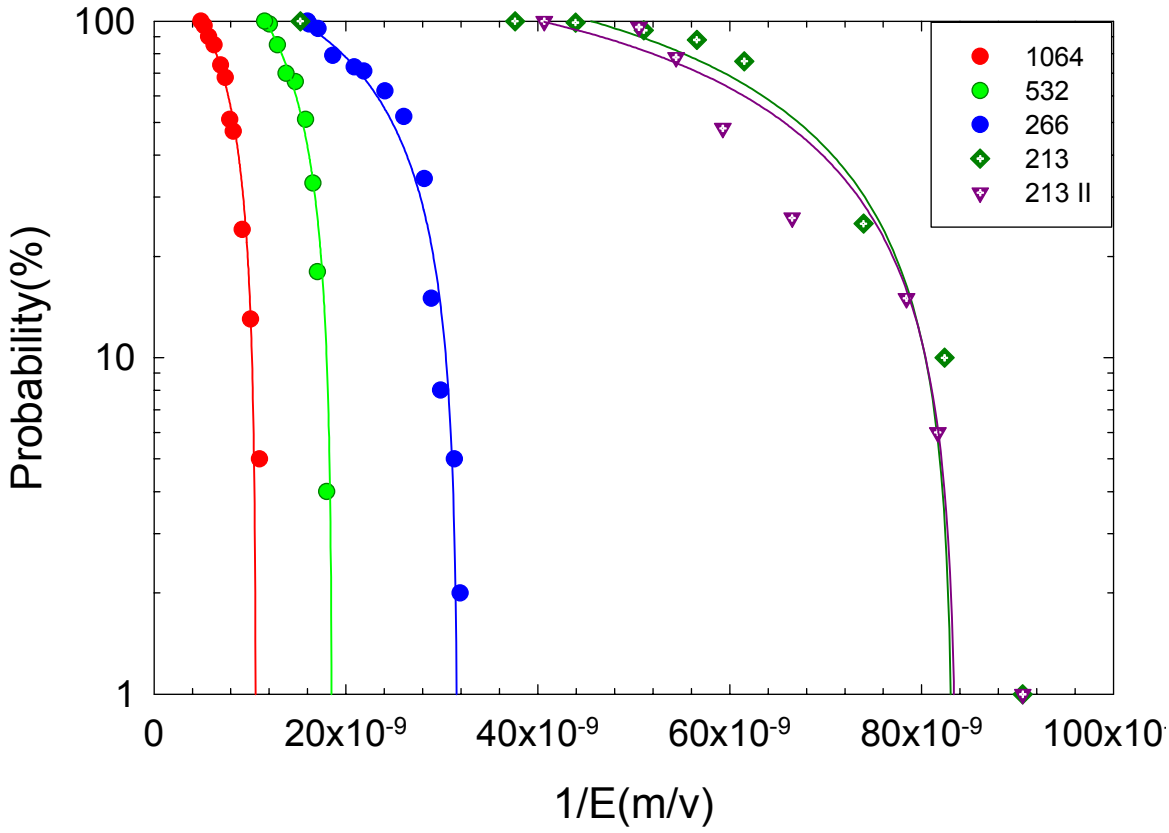

Figure 4-10 The sample data plotted with ablation probability P as a function of the reciprocal of the rms electric field $\mathcal{E}$ of the laser pulse. Solid lines are fitting curves for each set of data following an equation $P=P_0\exp(-K^2/\mathcal{E}^2)$, where P_0 and K are fitting parameters (75mm_allprob.jnb.)

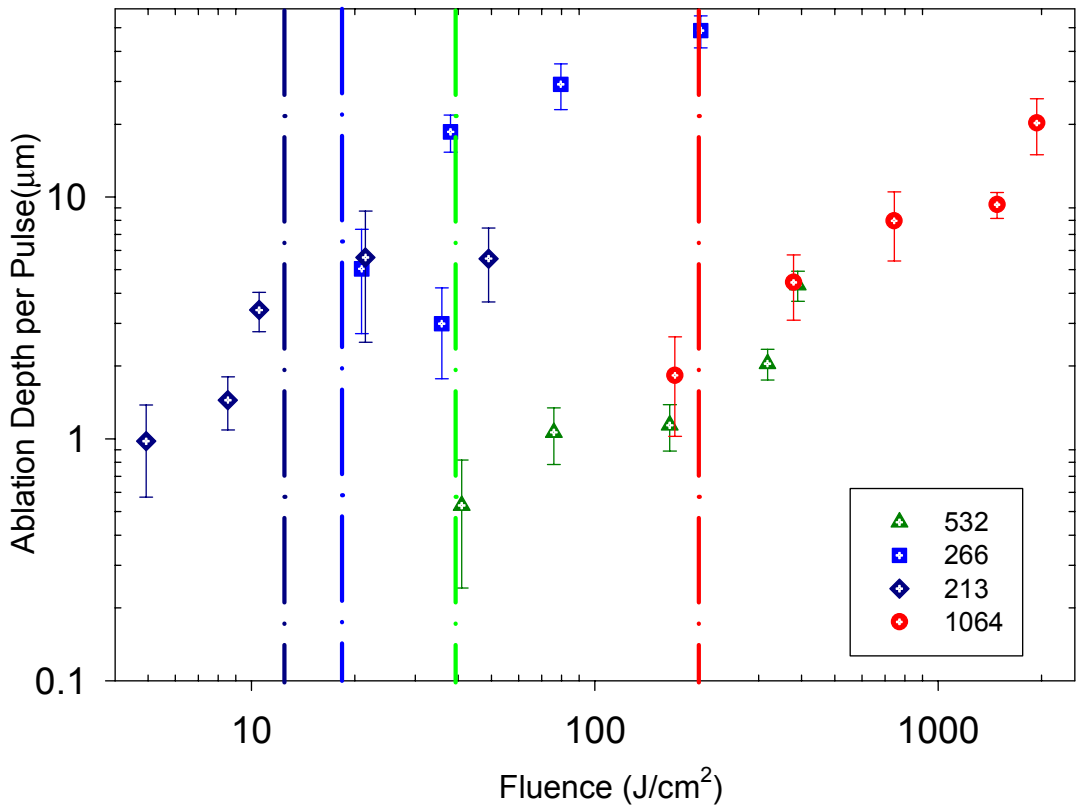

Figure 4-11 Histology measurement of ablation depth per pulse versus laser fluence at different ablation wavelength λ. The error bars indicate the fluctuation from multiple tissue sections and the vertical lines mark the position of laser fluence threshold F_{th}(@P=90%) from Table 4-1.

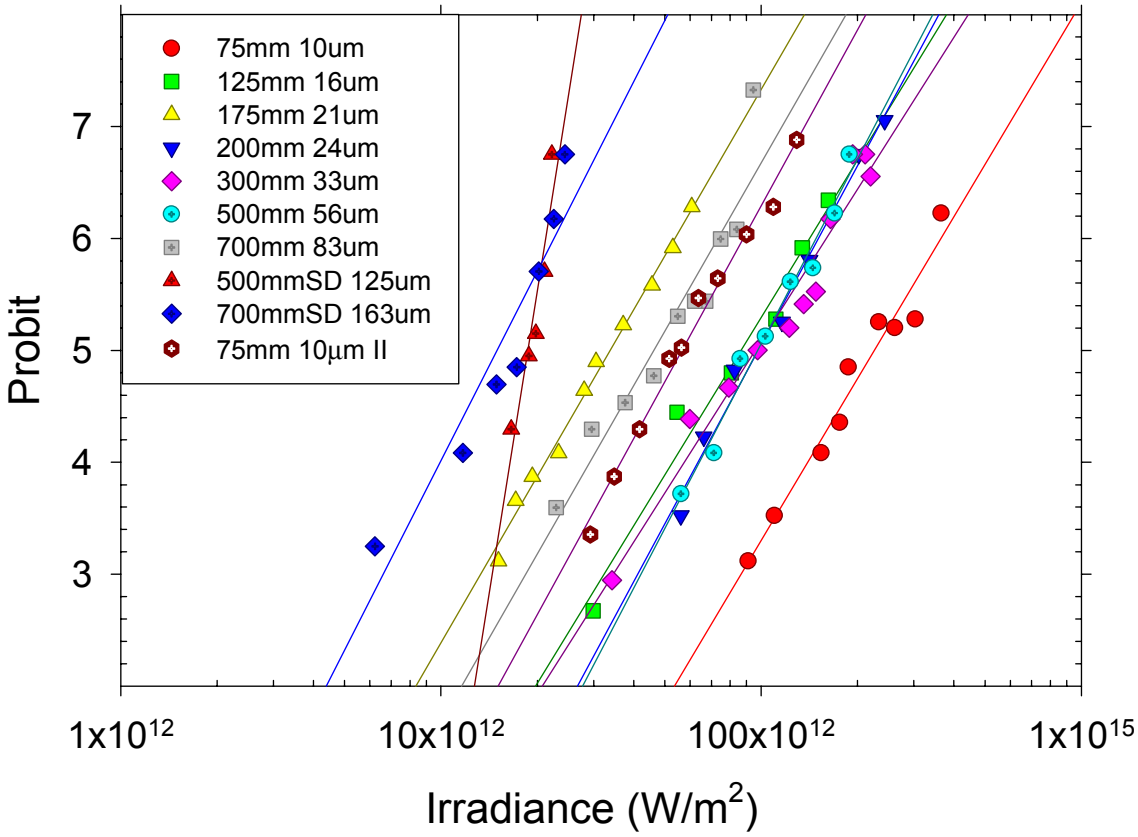

Figure 4-12 Probit of the ablation probability as a function of laser irradiance I at different ablation spot sizes (Ablation_Probability_1064_AllLens_New.jnb.)

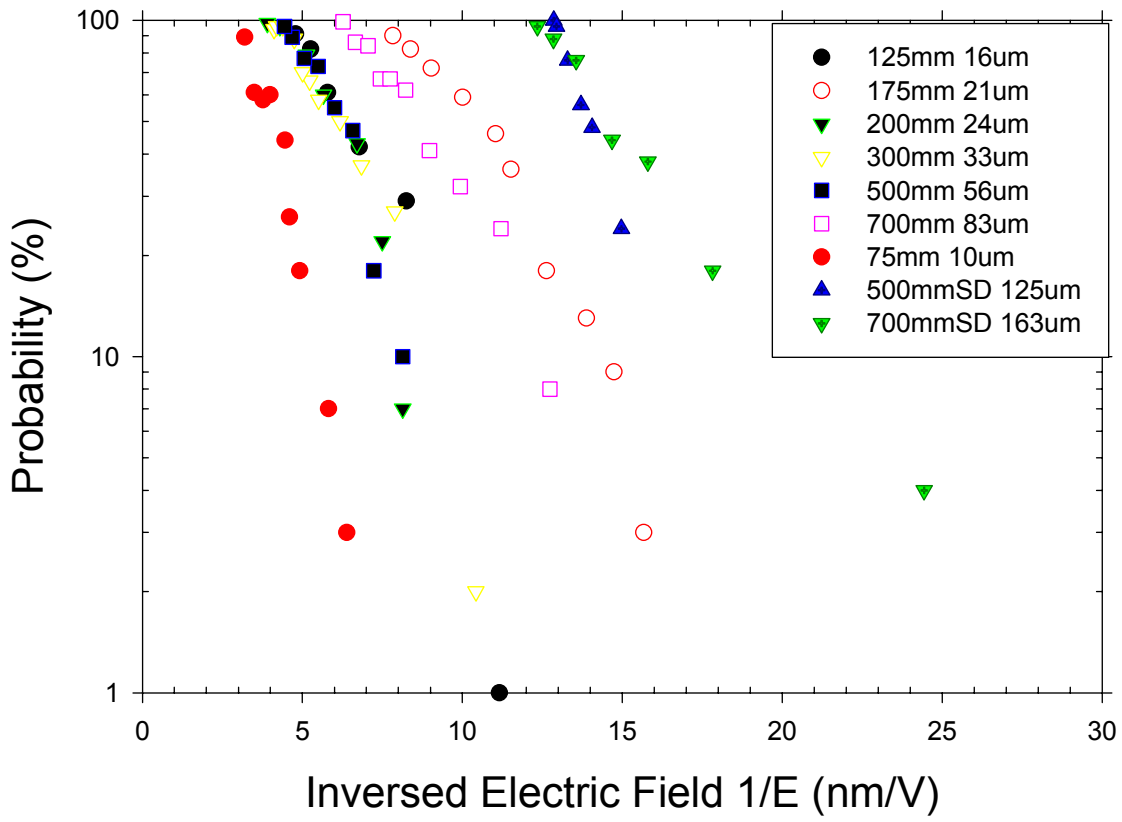

Figure 4-13 Ablation probability as a function of the laser irradiance at the seven spot sizes. Original data: ablation_probability_1064_all_lens.jnb

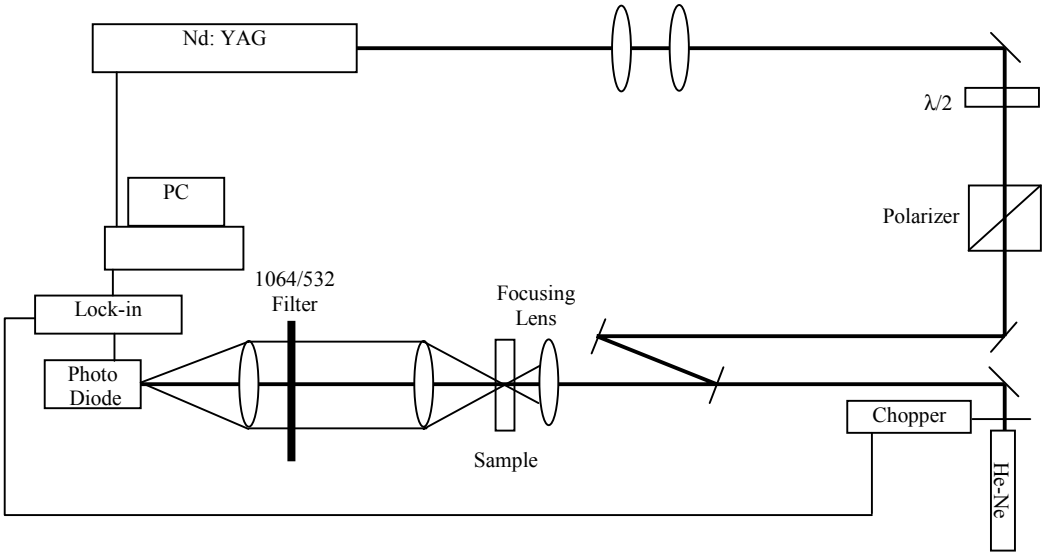

Figure 4-14 Schematic of the experimental setup for ablation depth measurements using an optical transmission measurement.

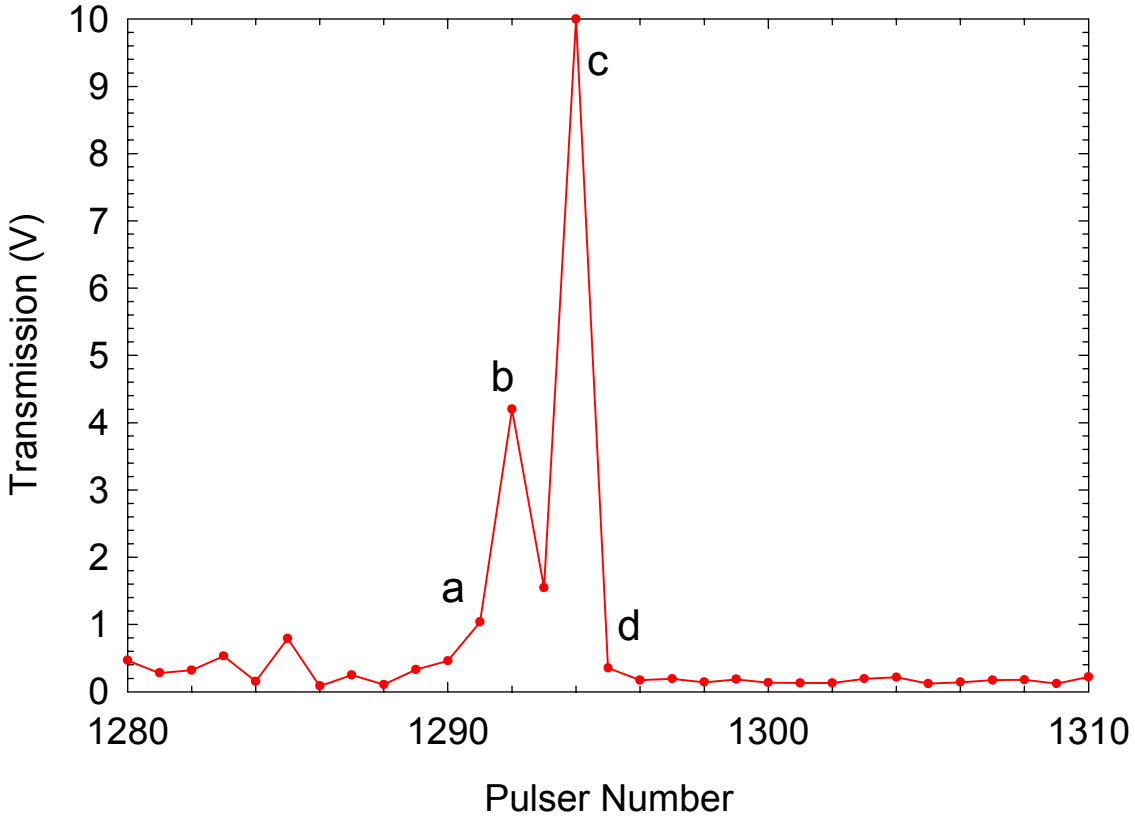

Figure 4-15 The transmitted light intensity versus the pulse number for optical transmission measurement at 1064nm with pulse duration of 12ns and pulse energy of 4mJ (000919.jnb.)

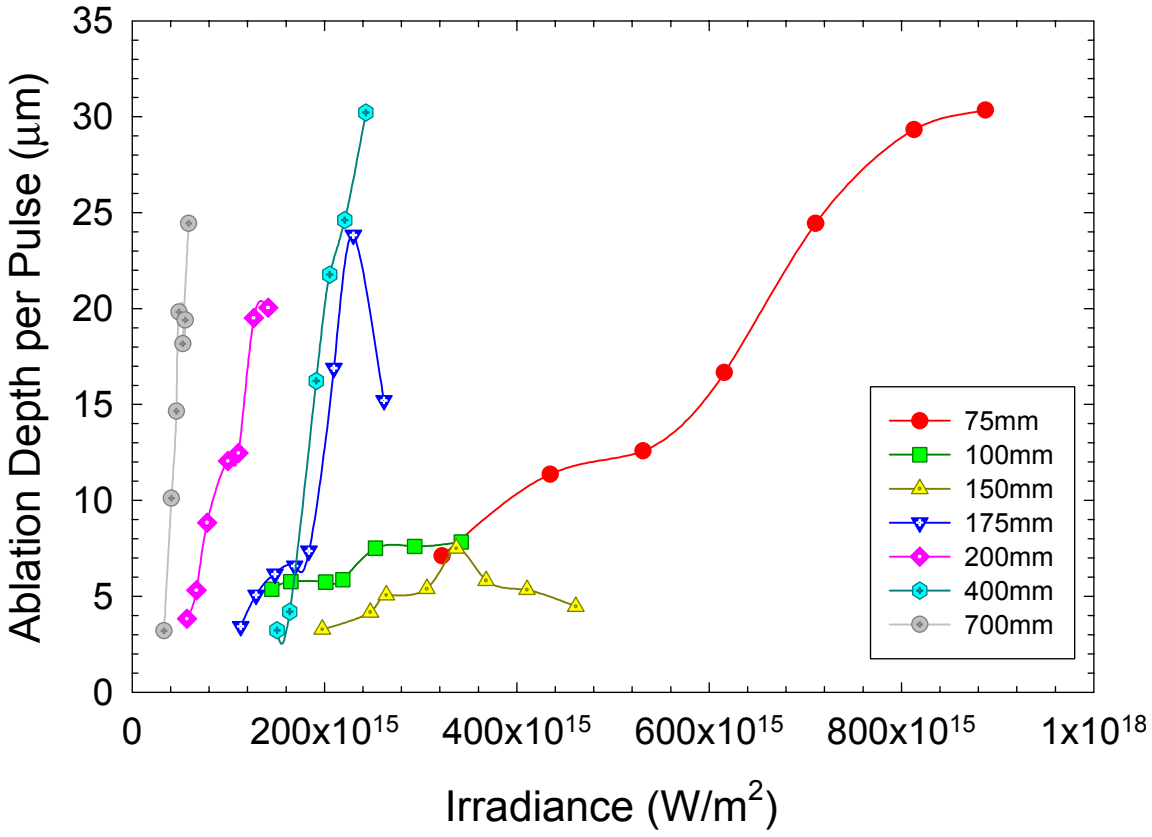

Figure 4-16 Optical probe transmission measurement of ablation depth per pulse versus laser irradiance at different ablation spot sizes at λ=1064nm (Ablation_depth_1064_drilling.jnb.)

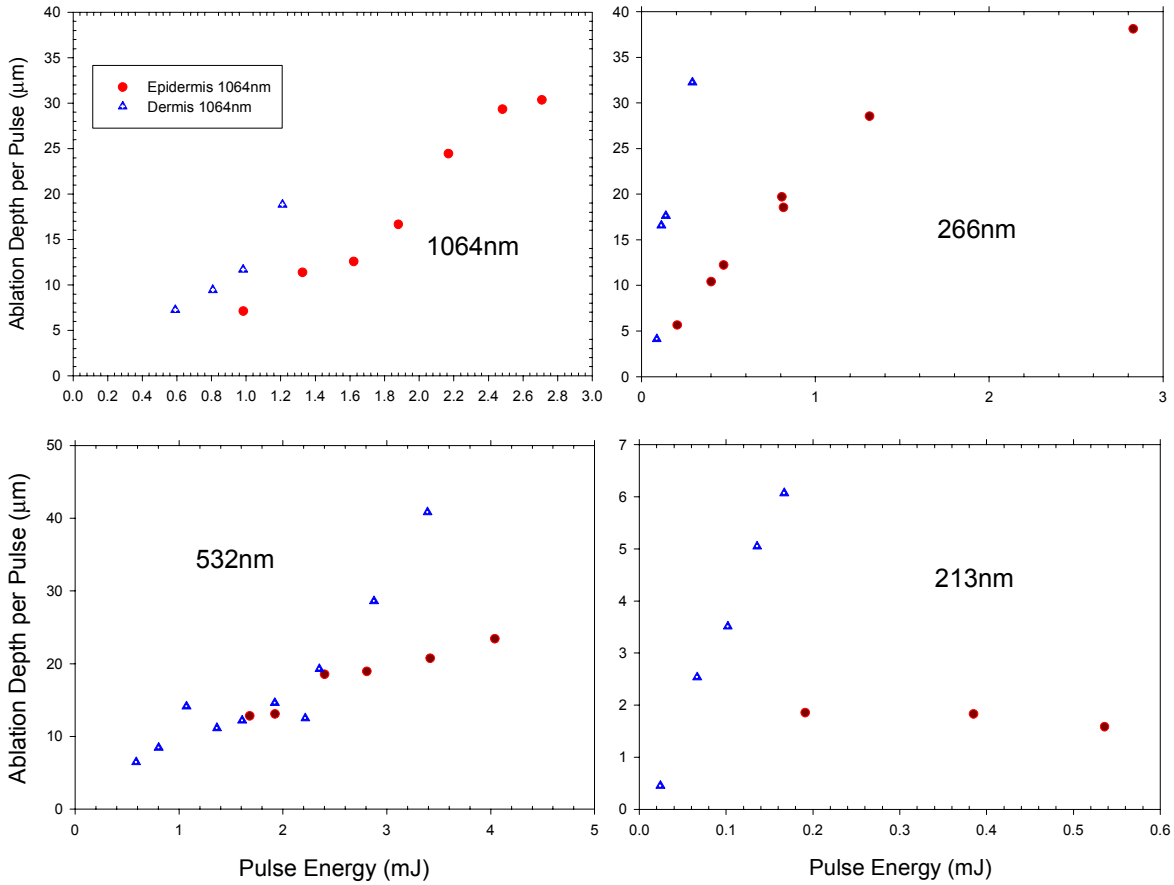

Figure 4-17 Ablation depth per pulse for epidermis and dermis at 1064, 532, 266, and 213nm (Tissue_Dermis_Absorbance.jnb.)

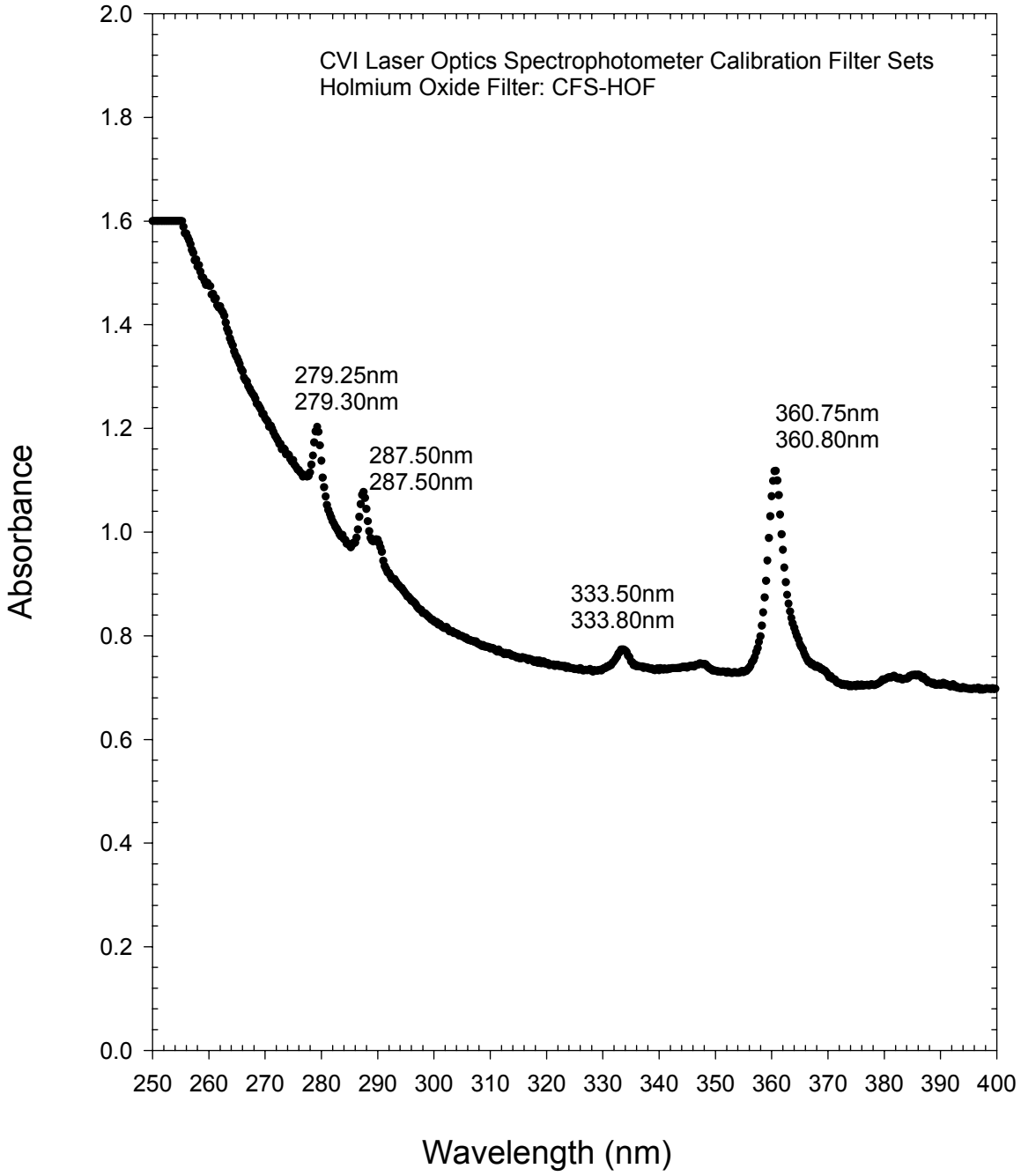

Figure 4-18 Calibration of the Cary 17D spectrophotometer using CVI Holmium Oxide filter. The reading on top at each peak is the standard Holmium Oxide absorption peaks; the reading below is the measured wavelength (Calibration.jnb.)

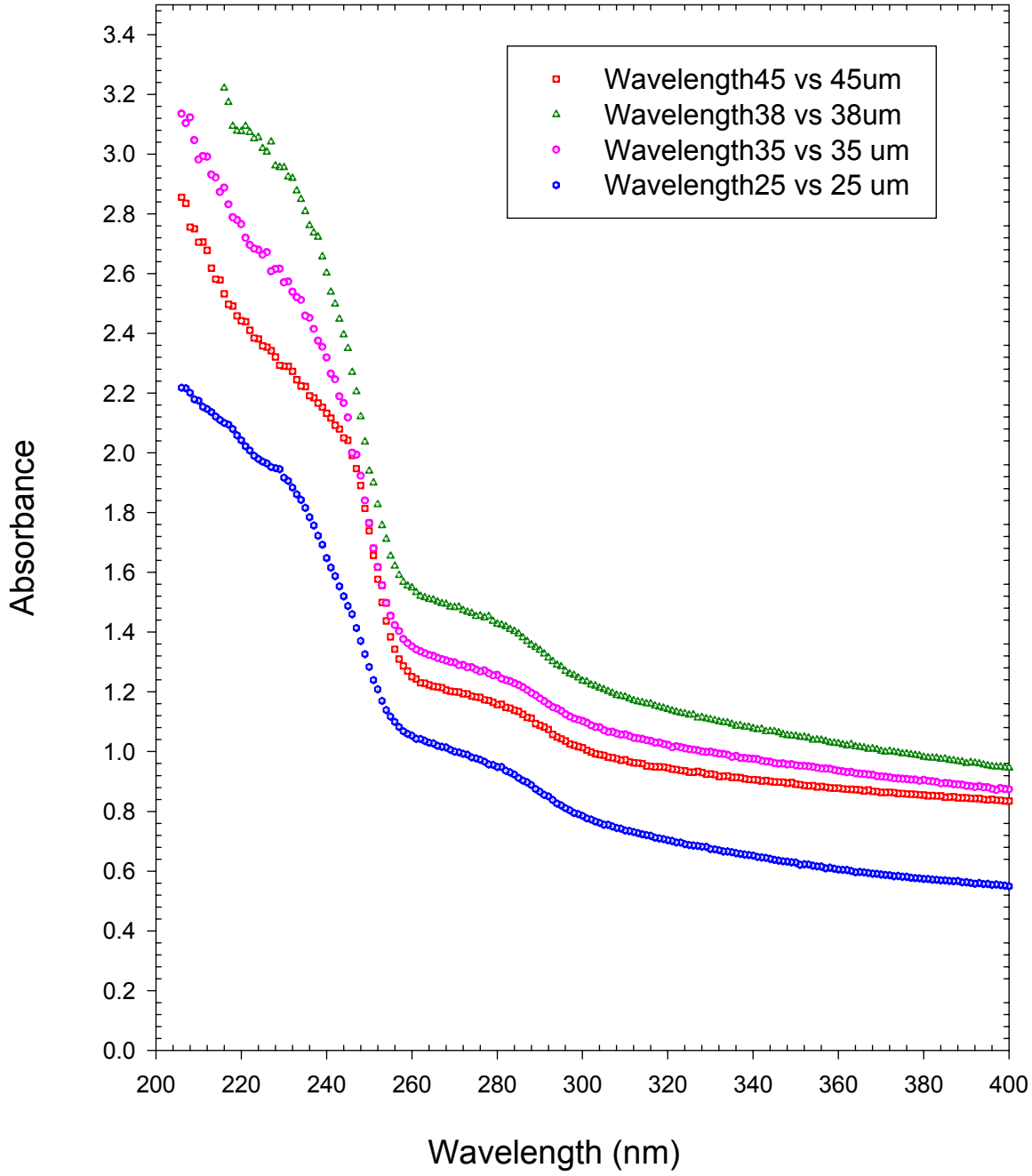

Figure 4-19 Absorbance of porcine skin dermis sections with different thickness (Tissue_Dermis_Absorbance.jnb.)

Chapter 5 Experimental Results II – Water and Gel

In this chapter, the experimental results on optical breakdown in distilled water, saline solution, and gelatin will be presented to enhance the understanding on the skin tissue ablation by nanosecond laser pulses. The backscattering of the incident laser light in water due to stimulated Brillouin scattering (SBS) will be investigated in section 5-1. Section 5-2 will depict the measurements of nonlinear refractive index n_2 of water at 1064 and 532nm using a z-scan method to determine the electronic and thermal contributions to the nonlinear index, which may be used to interpret the results on optical breakdown. Additional experimental results will be presented in section 5-3 on a preliminary study of ablation probability measurement on gelatin. These experimental results will be discussed in the last section.

5.1 Optical Breakdown and Backscattering in Water

Water consists more than 70% of tissue wet weight and serves as an important component of soft tissue. Laser-induced optical breakdown in aqueous solutions has attracted wide attention for its significance in the fundamental research on laser-matter interaction and as a baseline model for studying ablation of soft biological tissues by short laser pulses [Sacchi 1991; Juhasz, Hu 1994; Kennedy 1995; Vogel, Nahen 1996; Noack and Vogel 1999]. In all previous investigations, the LIR has been used as the signature for the occurrence of optical breakdown and determination of the threshold [Barnes and Rieckhoff 1968; Sacchi 1991; Kennedy 1995; Vogel, Nahen 1996; Noack and Vogel 1999]. The LIR spectra in water and 0.9% saline solution were measured and

presented together with that from ablated porcine skin surface and optical breakdown in air shown in Figure 5-1. The subsequent optical breakdown probability dependence on laser electrical field in water and saline were also similar to that of porcine skin tissue as shown in Figure 5-2. Recently, backscattered light due to the stimulated Brillouin scattering (SBS) was studied experimentally that provides a more sensitive signal than LIR for determining the breakdown thresholds in water through measurements of both the LIR and SBS signals at 1064 and 532nm with laser pulses around 10ns.

5.1.1 Optical and Electrical Systems Setup

The optical system setup of the experiment is shown in Figure 5-3. For experiments at 1064nm, the setup and the laser pulse characteristics before focusing are similar to that of optical measurement of tissue ablation depth described in section 4.4. The 9 to12ns laser pulses were obtained from the Q-switched Nd:YAG laser at 1064nm and its second harmonic at 532nm with a KTP crystal. The maximum pulse energy could be further reduced by 50% via modifying the Q-switch delay time from at 203μs, at which the pulse energy peaks at 9ns, to 260μs at which pulse duration increases to 12ns. The pulse energy was continuously adjusted by a half-wave plate and a polarization cube. The Q-switch delay time 203ms was used to achieve maximum energy output at the 2^{nd} harmonic generation, which yields 9ns pulses. The pulse energy at 532nm was continuously adjusted by a half-wave plate through changing the polarization direction of the beam at 1064nm incident on the KTP crystal. An inverted telescope was used to obtain a collimated incident beam of 6mm in diameter for both 1064 and 532nm. The temporal and spatial profiles of the incident beam were determined using the CCD beam

profiling system and a fast Si photodiode detector with the digital oscilloscope. Due to the higher requirement for input beam profile in the n_2 measurement, which will be described in detail in the next section, the beam was further filtered by a 2mm aperture that eliminates high order modes in the laser output to achieve a spatial profile closer to Gaussian beam. The spatial profiles of the laser beam before and after the aperture are shown in Figure 5-4 at 532nm obtained via the Spiricon CCD beam profile analyzer. Additionally for experiments at 1064nm, two partial reflection (65% and 90% @1064nm) mirrors were used to replace the high reflectance (HR) mirror used previously such that the pulse energy can be further reduced without excessive distortion of the beam spatial profile after the polarization cube. A 4° BK7 glass wedge was used to reflect a small portion (less than 4%) of the backscattering beam transmitted through the 65% reflective mirror into the photodiode PD3 (FDS 100, Thorlabs, 10ns rise time, 13mm^2 active area) to avoid damaging the detector and the neutral density filters placed before the detector. A 30cm long black tube of 10mm diameter was placed before the photodiode PD3 to allow only the collimated backscattering beam reaching the detector. A 1° wedges was used behind the 65% reflective mirror with the photodiode PD4 to monitor pulse-to-pulse fluctuation in the incident beam. The beam was focused into a 76.2mm long glass cell filled with singly distilled water using a lens of 75mm focal length. The water cell is a rectangular box made from BK7 glass. Its length along the optical path is 35.44mm with walls of 1.04mm in thickness. Its length on the other horizontal direction is 25.22mm with walls of 2.39mm in thickness. The distance between the focal spot inside the cell and the cell wall on the incident side is 17mm. By using the knife-edge method, the

radius of the focal spot in the water was determined to be 33.8μm (M^2=1.21) at 1064nm as shown in Figure 5-5 and 27.2μm (M^2=2.10) at 532nm as shown in Figure 5-6, respectively. A plano-convex lens with 200mm focal length was used to focus the transmitted beam into the CCD beam profiling system in the knife-edge measurement. Details of the measurement of focusing spot size using knife-edge and M^2 factor are given in Appendix I. In order to separate the backscattering light from the front surface reflection of the water cell, the water cell was slightly tilted to avoid the overlapping of the reflected beam with the backscattering beam. The LIR signal was measured by a fast Si photodiode detector (PD1, FDS 100, Thorlabs, 10ns rise time, 13mm^2 active area) attached to the sidewall of the water cell and filtered by a 1064 or 532nm notch filter to prevent the scattered incident light reaching the detector. A mirror was placed on the other sidewall of the water cell to increase the sensitivity of the LIR signal detection.

The electronic system setup is shown in Figure 5-7. There are four pulse signals that need to be measured simultaneously: the incident pulse as the reference (measured by PD4), transmitted pulse (by PD2), LIR pulse from the breakdown site in water (by PD1), and SBS pulse from the backscattered beam (by PD3). The laser induced optical breakdown in the water cell occurs ~~at~~ along the beam focal spot waist, so it not necessarily comes from the same location, which means that the LIR and SBS pulses are not confined to small areas on the detectors. As a result, two Si fast photodiodes with large (13mm^2) active areas and a rise time of 10ns (FDS100, Thorlabs) were chosen for PD1 and PD3 with. The PD2 and PD4 for the reference and the transmitted beam have active area of 1mm^2 with a rise time less than 1ns (FDS010, Thorlabs, 0.8mm^2 active

area). The transmitted signal and the spark signal obtained by PD 1 and PD 2 were measured with two gated boxcar integrators (SR250, Stanford Research Inc.) The digital oscilloscope was used to monitor the timing between the boxcar gates (50ns wide) and the reference and transmitted signals to ensure the 15ns (FWHM) signals being completed gated. A preamplifier (SR560 Stanford Research Inc.) was used to amplify the difference between the backscattering signal (PD3) and the reference signal (PD4) with a bandwidth of 18Hz to 100kHz such that it can be integrated and picked up by the A/D board without using another boxcar integrator. The outputs of the two boxcars (for transmitted and LIR) and the preamplifier (for SBS) were acquired by a fast A/D board on a personal computer. The electrical data acquisition system is synchronized with the laser pulse output via the digital delay and signal generator. The data acquisition control program (backs.bas) is listed in Appendix III.

5.1.2 Measurements and Results

When aligning a portion of the incident laser beam with the SBS beam, an interference pattern indicate the wavelength of the SBS signal is very close to that of the incident laser beam at 1064nm due to the overlapping of the multi-modes structures in the incident pulses and the SBS pulses. The SBS signal has been observed to have a probabilistic behavior near the breakdown threshold similar to that of LIR in water, i.e. two thresholds of 0% and 100% as well as a monochromatic increase of the SBS probability as a function of laser electrical field between the two thresholds. The probabilistic behaviors of the SBS and LIR signals have been measured and compared from the laser-induced plasma near the threshold at two wavelengths of 1064 and 532nm. Both the Stimulated

Brillouin Scattering and laser induced secondary radiation originated from the laser-induced plasma in water. They both have pulse durations about 10ns, which is similar to that of the original pulse. However, LIR is of broadband in nature, isotropic, and weak. Besides plasma, it may also come from thermal effects and is difficult to be separate from ambient light. On the contrary, SBS is coherent, quasi-monochromatic, highly directional, and intense. It also has strong irradiance that comparable to the incident laser pulse. When the laser irradiances were a few times larger than the 100% breakdown threshold, it has been found that the SBS in the backscattered direction (θ=180deg) can damage the turning mirrors with dielectric coating of nominal damage threshold 5J/cm^2 because of the highly collimated backscattered beam with a diameter much smaller than the incident beam. To avoid the damage to the mirrors, this study has been limited to irradiance below and near the 100% threshold. At each pulse energy level, 500 pulses were used at a repetition rate of 1Hz and the SBS and LIR signals were measured. At pulse energy below the 0% threshold, the fluctuation of the environmental noise picked up by the detector (PD3) is about ±5%. Any signal higher than 110% of the average reading of the background is determined to be the occurrence of the SBS signal. A program that reads the experiment data and counts the probability of the SBS and LIR was written in Visual Basic code, which is given in Appendix III. The probability of the LIR and SBS occurrence was determined by the ratio of the number of laser pulses with LIR or SBS signal to the total number of the incident pulses and is plotted against the inverse of the rms electric field of the laser pulse in Figure 5-8. Both the SBS and LIR originated from the laser-induced plasma in water and their pulse durations were

measured through the digital oscilloscope to be about 10ns (FWHM), which is similar to that of the incident pulse. The probability of SBS also increases much faster than that of LIR when laser electrical field increases.

5.2 Nonlinear Refraction Measurement using Z-Scan Technique

5.2.1 Theoretical Background

The thresholds and intensity of the SBS signal in liquids can be greatly affected by the electrical and thermal nonlinear properties of the medium [Tikhonchuk, Fuchs 2001]. To understand the SBS signal during optical breakdown in water, the nonlinear refractive index n_2 was further measured by the same 12ns pulses at the wavelengths of 1064 and 532nm using a z-scan method below the breakdown threshold. The z-scan technique is an increasingly popular method for the measurement of optical nonlinearities, i.e. refraction or absorption, since it has the advantage that it immediately indicates the sign (positive or negative) and type of nonlinearity (refractive or absorptive). A comprehensive review of the z-scan technique and recent development has been given by Chapple et. al. [Chapple, Staromlynska 1997], whose results relevant to the studies have been summarize here. In the z-scan method, a sample is scanned along the optic axis (the z-direction) through the focus of a single laser beam, while the energy transmitted through an aperture in the far field is recorded as a function of sample position, as shown in Figure 5-3. For optical absorber, the transmitted beam is completely focused into the detector instead so the variation of the total transmitted light energy can be measured. The measured transmission in the far field behind an optical aperture T is therefore a

function of z, which is the relative position between the medium and the focal plane of the lens along the z direction. Assuming a thin sample with medium only having negative nonlinear refraction, it is equivalent to a concave Kerr lens under strong light field. When the sample starts scanning from far field before the focal plane, the light is weak and the transmission T remains as a constant T_0 due to very weak nonlinear refraction change. As the sample scans closer to the focal plane, the light field becomes stronger so it induces a concave Kerr lens that makes the overall system focusing length longer. Therefore, the far field transmission T becomes larger than T_0. When the sample passes the focal plane, the concave Kerr lens behind the focal plane makes the overall system focal length shorter so T will decrease. The transmission T will go back to T_0 when the sample goes to far field when the light field is weak. Similarly, a medium with positive nonlinear refraction will form a convex Kerr lens that will decrease T before the focal plane and increase T after it. For all z-scan curves, a peak before the focal plane followed by a valley after indicates negative nonlinear refraction index while a valley followed by a peak gives positive nonlinear refraction index. In the case of the presence of nonlinear absorption, it will bring down the peak and strengthen the valley when there is a far field aperture. When the aperture is eliminated and total transmission is measured, the nonlinear absorption can be given by a z-scan curve with only a valley. For a thick sample, the positions of the peak and valley in the z-scan curve roughly identify the position of the cell walls.

For a Kerr nonlinearity [Shen 1984], the refraction index n of the medium are usually a polynomial function of the intensity of the incident light:

$$n = n_0 + n_I I + n_{II} I^2 + \cdots = n_0 + \frac{1}{2} n_2 \left|\mathcal{E}\right|^2 + \cdots, \tag{5.1}$$

in which n_0 is the linear refraction index; n_I or n_2 is the first order nonlinear refraction index; n_{II} or n_3 is the second order refraction index, and so forth; I is the irradiance of the incident laser light; and $\mathcal{E}$ is the electric field of the incident laser light. n_I is related with n_2 by:

$$n_I \left(m^2 W^{-1}\right) = \frac{40\pi n_2 \left(esu\right)}{n_0 c \left(ms^{-1}\right)}, \tag{5.2}$$

where c is the speed of the light in vacuum. The nonlinear phase change $\Delta\Phi_0$ is given by:

$$\Delta\Phi_{0R} = k n_I I_0 n_0 Z_R = \left(\frac{2\pi}{\lambda}\right) n_I \left(\frac{E_0}{\pi w_0^2 \tau}\right) n_0 \left(\frac{\pi w_0^2}{\lambda}\right) \tag{5.3}$$

in which,

$$\begin{aligned} k &= \frac{2\pi}{\lambda} \\ I_0 &= \frac{E_0}{\pi w_0^2 \tau} \\ Z_R &= \frac{\pi w_0^2}{\lambda} \\ w_0 &= \frac{f \cdot \lambda}{D_0} \end{aligned}, \tag{5.4}$$

where λ is the laser wavelength; I_0 is the axial irradiance at the waist; E_0 is the pulse energy, w_0 is the focusing volume diameter; Z_R is the Reyleigh length; and D_0 is the length of the focusing region along z axis defined as $D=2Z_R$.

The nonlinear phase change $\Delta\Phi$ can often be evaluated from ΔT, which is defined as the difference between the maximum and minimum values of the normalized transmittance. For a thick optical Kerr medium, i.e. where the refractive index varies linearly with irradiance, the normalized transmittance can be related to the nonlinear phase shift by:

$$\Delta T = \frac{\left|\Delta\Phi_{0R}\right|}{2} \ln\left[\frac{9+\Omega-\Gamma}{1+\Omega-\Gamma}\cdot\frac{1+\Omega+\Gamma}{9+\Omega+\Gamma}\right], \tag{5.5}$$

where

$$\begin{aligned}
\Omega &= \eta + \frac{1}{3}\zeta_m^2 \\
\Gamma &= \zeta_m\left(\eta + \frac{1}{12}\zeta_m^2\right)^{\frac{1}{2}} \\
\eta &= -\frac{5}{3} + \left[3 + \frac{1}{9}\left(5 + \frac{1}{2}\zeta_m^2\right)^2\right]^{\frac{1}{2}}
\end{aligned} \tag{5.6}$$

and

$$\zeta_m = \frac{L}{n_0 Z_R}, \tag{5.7}$$

where L is the length of the water cell. The normalized ΔT can be obtained through experimental results and the nonlinear phase change $\Delta\Phi$ can be determined by using Eq. (5.5). The nonlinear refraction index n_2 was therefore calculated via Eqs. (5.3) and (5.2) as:

$$n_I = \frac{2}{\left(\frac{2\pi}{\lambda}\right)\left(\frac{E_0}{\pi w_0^2 \tau}\right) n_0 \left(\frac{\pi w_0^2}{\lambda}\right) \cdot \Delta T \cdot \ln\left[\frac{9+\Omega-\Gamma}{1+\Omega-\Gamma} \cdot \frac{1+\Omega+\Gamma}{9+\Omega+\Gamma}\right]}. \tag{5.8}$$

5.2.2 Experimental Setup and Results

The optical system setup of the backscattering measurement is shown in Figure 5-3. In order to compare the nonlinear refraction index with the results obtained in the SBS measurements, identical optical system setup was maintained before the water cell. It was found that the damaging irradiance threshold of the glass slide used for water cell wall is less than 10% of that of water. Since both water cell walls will be pass the focal plane of the laser beam, incident pulse energy less than 5% of the water breakdown threshold was used in the n_2 measurements.

A 1° BK7 glass wedge replaced the 65% reflective mirror in the SBS measurement to further reduce the beam energy. The water cell was translated by a step motor along the z-axis for 40cm that both water cell walls will pass the focal plane of the beam. A photodiode with a 0.8mm^2 active area was placed after the water cell in the center of the transmitted beam to measure the transmitted signal change at far field, while the small active area of the photodiode also served as an aperture. In the nonlinear absorption measurement, a photodiode with 13mm^2 active area was used to collect the entire transmitted beam. Both the reference signal and the transmitted signal were collected by two photodiodes with gated integrators and processed by a PC. The system operated at a

repetition rate of 1Hz and 50μm per step. The translation of the step motor and data acquisition was controlled by a PC with the code given in Appendix III.

The accuracy of the z-scan measurement is very sensitive to the beam quality, system stability, and linearity of the measurement. The stability and linearity of the n_2 measurement was verified at 1064nm by measuring the response of the reference and transmittance detectors at different pulse energies adjusted via rotating the $\lambda/2$ wave plate. The results are shown in Figure 5-9, while each point represents averaging over 100 pulses.

From the z-scan results at 532nm shown in Figure 5-10, the measured values are: L = 0.036m, $\Delta T = 0.354$, $E_0 = 0.242$mJ, $\tau = 12$ns, $\alpha_0 = 3.5\times10^{-2}m^{-1}$. Therefore, by using Eqs. (5.2) to (5.8), the nonlinear refraction index is found to be $n_I = 5.38\times10^{-19}m^2W^{-1}$, or $n_2 = 1.72\times10^{-12}$esu. At 1064nm, as shown in Figure 5-11 the measured values are: L = 0.038m, $\Delta T = 0.579$, $E_0 = 0.402$mJ, $\tau = 10$ns, $\alpha_0 = 100m^{-1}$. Then it yields $n_I = -1.77\times10^{-18}m^2W^{-1}$, and $n_2 = -5.68\times10^{-12}$esu. The opposite signs of the n_2 at the two wavelengths suggest that the electronic and ionic contributions to the optical breakdown are different on the nanosecond time scales [Chapple, Staromlynska 1997].

5.3 Optical Breakdown Probability Measurement on Gelatin

In Chapter 3, a new plasma model was proposed that introduces the localized thermal ionization contribution into the ionization process in which the bound electrons are ionized in the confined chromophores inside tissue. Although the ablation thresholds predicted from the hypothesis agree well with the experimental results on ablation of

porcine skin tissue, it is not quantitatively validated due to the fact that the optical characteristics of the chromophores are still unknown. In addition, the heterogeneity and complexity of the skin tissue have been greatly simplified in the model as optically transparent homogeneous medium doped with uniformly distributed absorbers. Recently, gelatin based tissue phantoms have been studied as an effective tool for tissue ablation [Paltauf and Schmidtkloiber 1995; Paltauf and SchmidtKloiber 1996; Sathyam, Shearin 1996]. It is usually doped with Indian ink of known concentration, which is considered to be composed by sub-micron spherical absorbers. The total absorption and/or scattering property of this kind of tissue phantoms can be determined by the combination of transmittance measurement and integrating sphere method. Therefore, it would be an ideal material for quantitatively validating the localized thermal ionization contribution. In this section, a preliminary study of gelatin ablated by laser pulses at 1064nm will be reported.

5.3.1 Materials and Methods

Agar solution was obtained by dissolving chemical grade agar powder into 0.9% saline solution at a ratio of 1:100 by weight. The solution is stirred and then heated to about 80°C until the agar power completely dissolved when the solution is clear and transparent. The solution is then put into a sample holder and cools down naturally to solidify at room temperature. The sample holder is made from transparent plastic square boxes of 1×2×⅜ inches. A hole of ⅜ inch in diameter was drilled on one side of the

sample holder to allow transmitted ablation beam passing through without inducing breakdown of the holder due to its lower threshold.

The optical and electronic system setup of gelatin ablation measurement is similar to that of porcine skin tissue ablation at 1064nm described in section 4.1. A step motor was applied to translate the sample holder horizontally (X direction as shown in Figure 5-12) at the waist of the focusing beam to assure each pulse ablating at a different location on the surface of the gelatin. The sample was also manually translated in the vertical direction (Y direction as shown in Figure 5-12) for the same purpose. Due to the much lower ablation threshold, the pulse energy was further reduced by a partial reflective mirror (80% @ 1064nm.) The secondary radiation spectra from the plasma generated on the surface of the sample was collected by the fiber optics spectrophotometer system. The digital delay and pulse generator was applied to synchronize the spectrophotometer and the step motor driving system on the external triggering signal of the laser.

The secondary radiation from the optical breakdown on the surface of the gelatin was first collected and compared with that from the porcine skin tissue ablation as shown in Figure 5-13. Similar spectral lines at 589nm and 656nm were identified as signatures of optical breakdown. By using this signature, the ablation probability at different energy levels (0.16mJ to 0.88mJ) was measured by counting the occurrence of breakdown for each 100 pulses. The results are show in Figure 5-14 and the probit analysis of the result is shown in Figure 5-15. The ablation probability dependence on the laser electrical dependence has been found to be similar to that of in porcine skin tissue ablation

described in section 4.1. The ablation thresholds, however, are found to be significantly smaller than that of skin tissue.

In order to increase the absorption the gelatin, Indian ink was doped into the agar solution at different concentration of 0.1%, 0.2%, 0.4%, and 1.0%. While trying to repeat the ablation probability measurement described above, the concurrence of the flash/spark from plasma generation and the collected secondary spectral lines could not be established for any ink doped samples. The LIR signal from the gelatin surface was at or below the observation thresholds of either naked eye or the CCD spectrophotometer. A correlation between the reading of the power meter behind the 4º wedge and the pulse energy after the focusing lens was established to measure the low pulse energy. Although there is no observable flash/spark or secondary radiation spectra, a line of craters on the surface of the 0.1% doped gelatin was found under a 4X optical microscope at pulse energy as low as 0.004mJ after ablating the tissue by 400 pulses at 50μm per step per pulse. It is clearly shown that the doping of absorber in gelatin significantly lowers the ablation threshold. This is predicted by both the new thermal ionization model proposed in Chapter 3 and the photo-thermal models reviewed in Chapter 2. Further quantitative measurement of the absorption coefficient and size of the absorber in this experiment are required to determine the fundamental mechanisms that governing the ablation processes. The experiment results will be further discussed in the last section of this chapter along with other experiment results.

5.4 Summary

Both the stimulated Brillouin scattering (SBS) and laser-induced secondary radiation (LIR) originate from the laser-induced plasma in water with pulse duration similar to that of the incident pulse. They also exhibited similar probabilistic behaviors as a function of laser rms field strength. The probability of SBS signal, however, increases much faster than that of LIR as demonstrated in this study at 1064 and 532nm with 10ns pulses. Therefore, the backscattering measurement provides a more sensitive signature than LIR for determining the breakdown thresholds in water. In addition, the coherent, quasi-monochromatic, and highly intense SBS signal is a more substantial signature than the broadband isotropic and weak LIR signal, which may also be a result of ambient light or thermal effects. The measurements of nonlinear refractive index n_2 of water at 1064 and 532nm using the z-scan method determine the electronic and thermal contributions to the nonlinear index, which may be used to interpret these results on optical breakdown.

The preliminary results on measurement of the ablation probability of gelatin samples has demonstrated that the secondary radiation signature for porcine skin tissue established in Chapter 4 are not suitable for gelatin based tissue phantom studies. The craters observed on the surface of the ink doped gelatin samples may result from two possible origins: optical breakdown on the gelatin surface with very low intensity secondary radiation that the fiber optics spectrophotometer could not pick up; or thermal damage due to thermal effects and the low structural strength of the gelatin.

Chapter 5 Figures

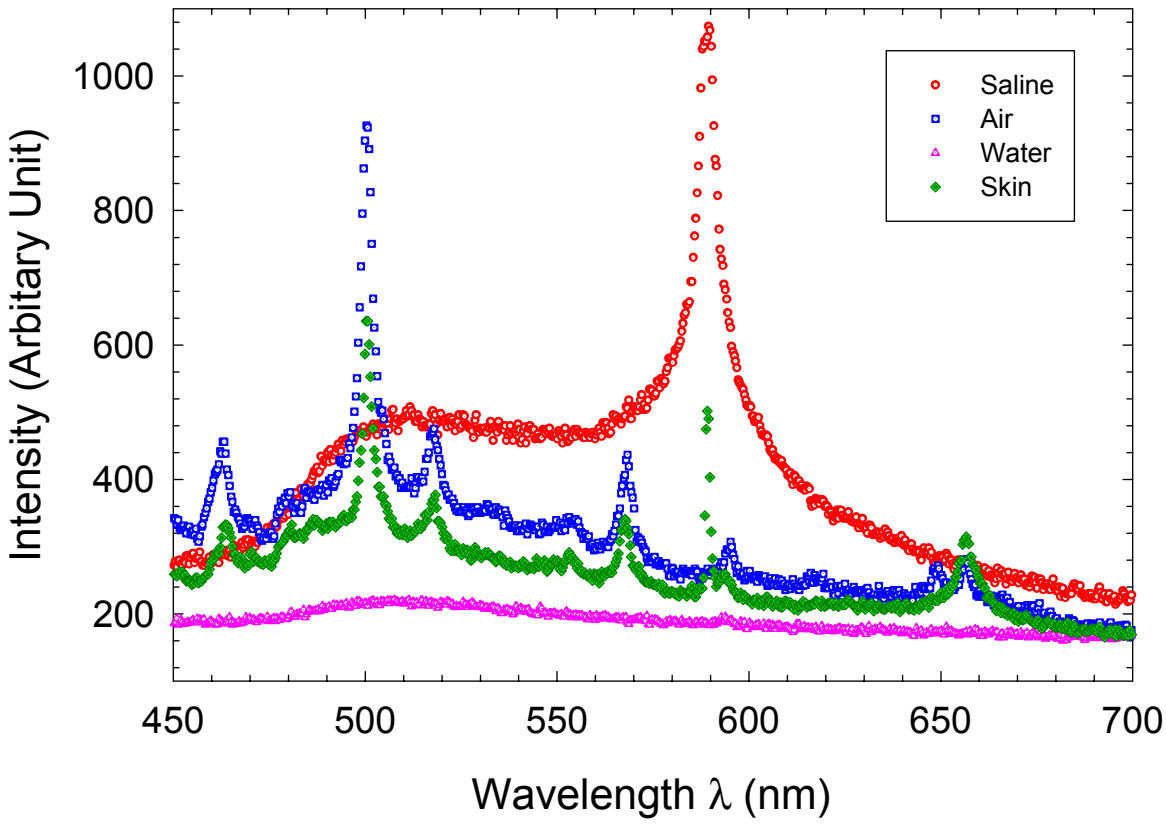

Figure 5-1 Laser induced fluorescence spectra from circle: 0.9% saline solution; square: air; triangle: distilled water; and diamond: skin tissue. Q-switch delay time: 203μs, focal lens f=75mm, wavelength λ=1064nm (ablation_spectra.jnb.)

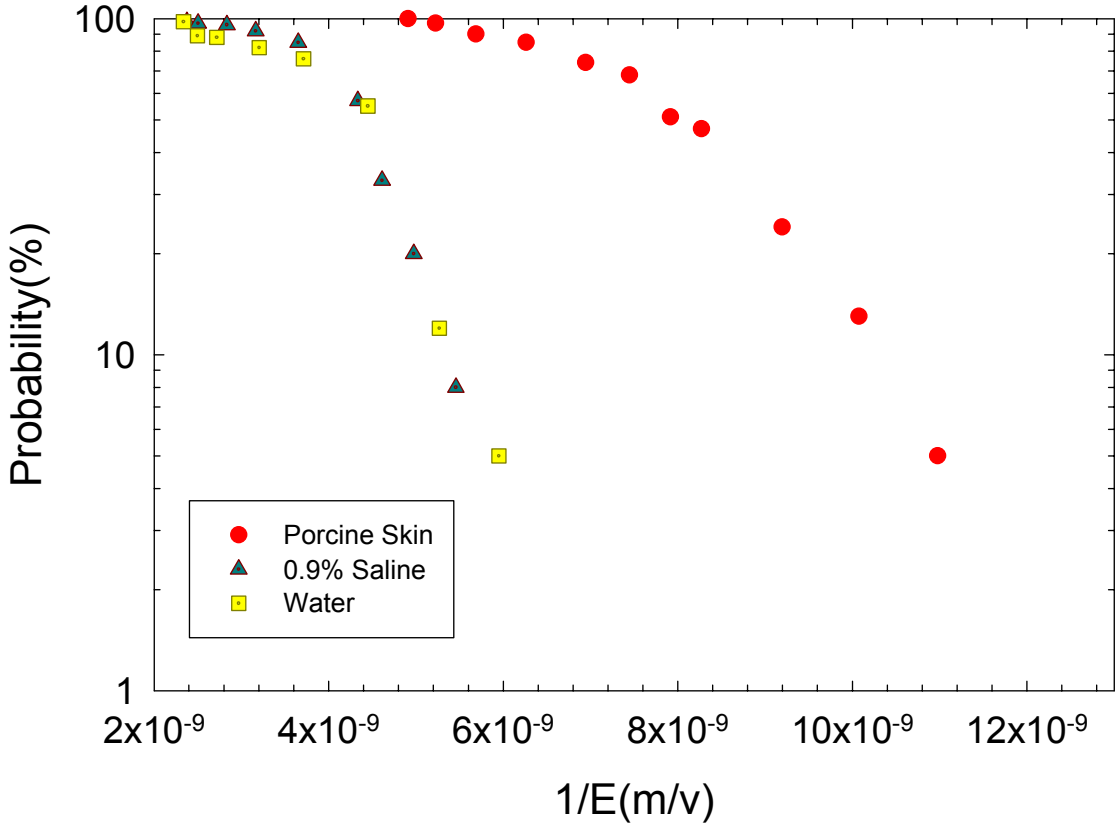

Figure 5-2 Optical breakdown probability vs. laser electric field at 1064nm for circle: on porcine skin tissue; triangle: 0.9% saline solution; square: distilled water. Q-switch delay time: 203μs, focal lens f=75mm, wavelength λ=1064nm (75AllProb.jnb.)

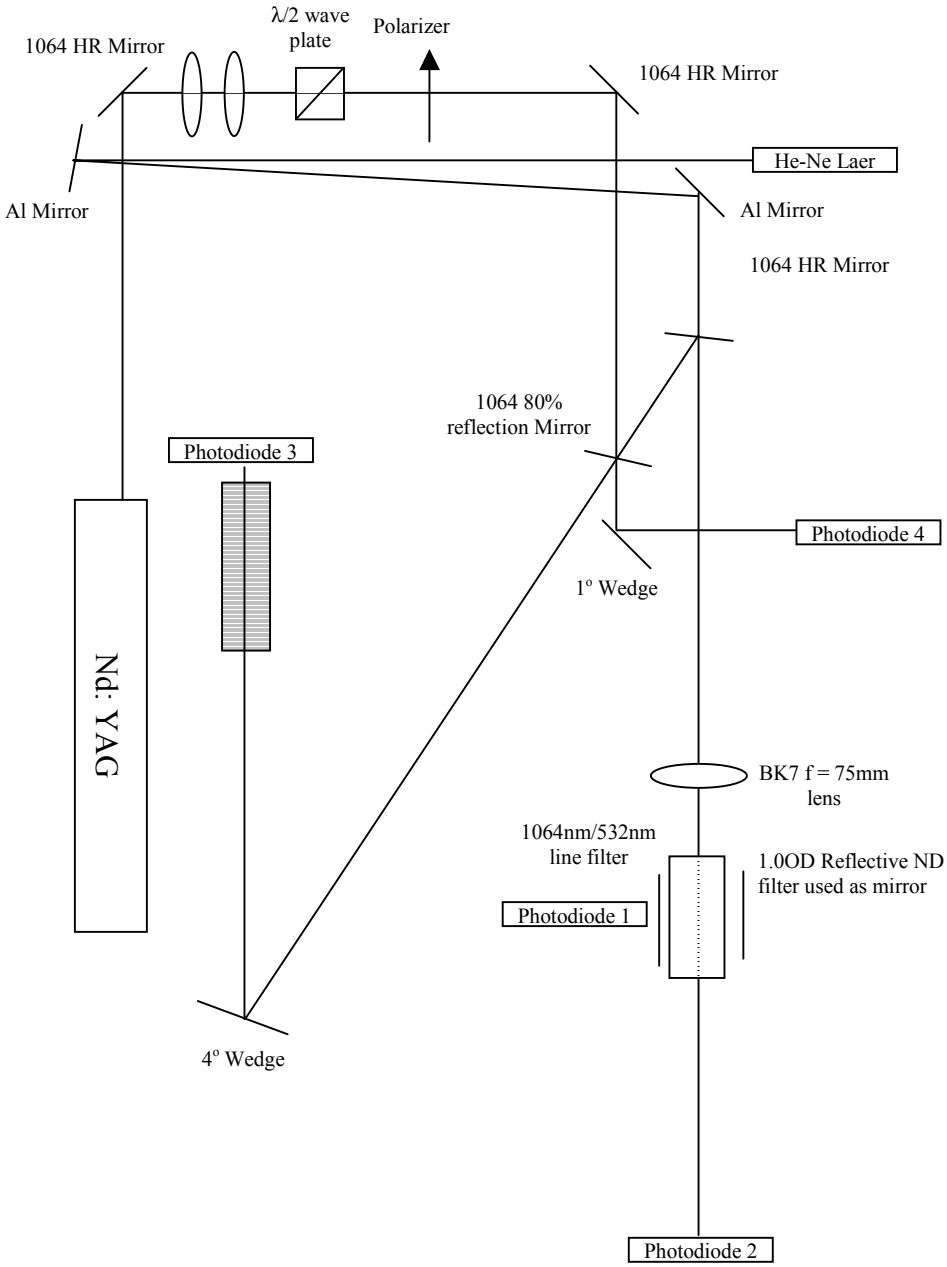

Figure 5-3 Optical system setup of the n_2 and backscattering measurement;

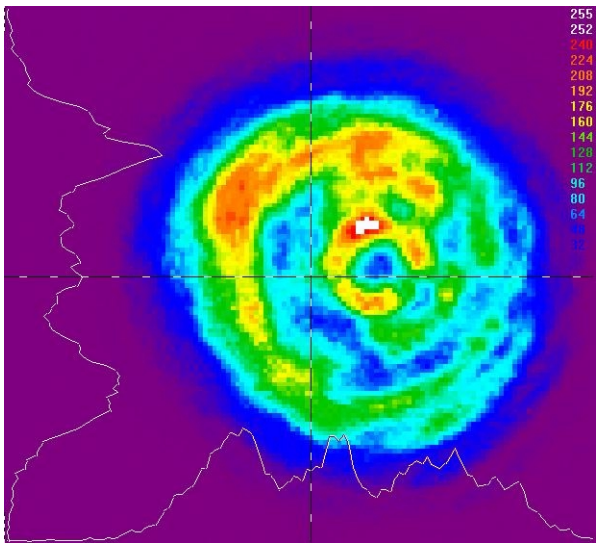

(a)

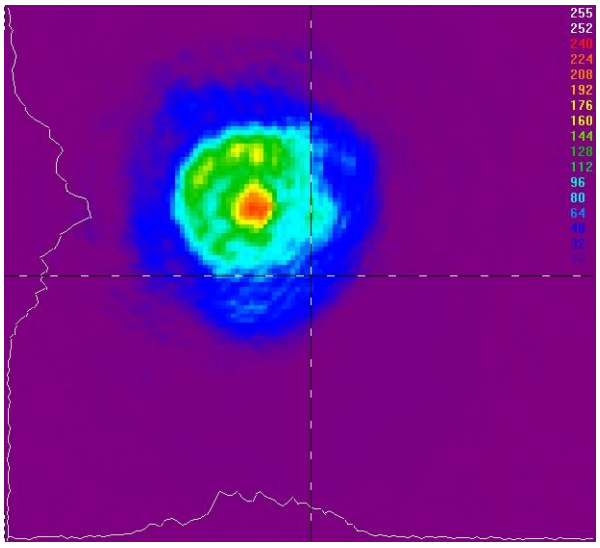

(b)

Figure 5-4 Spatial beam profiles for a) before the 2mm aperture, b) after the aperture measured @532nm. Pulse energy: less than 0.5mJ (011129a/b_532.lb3.)

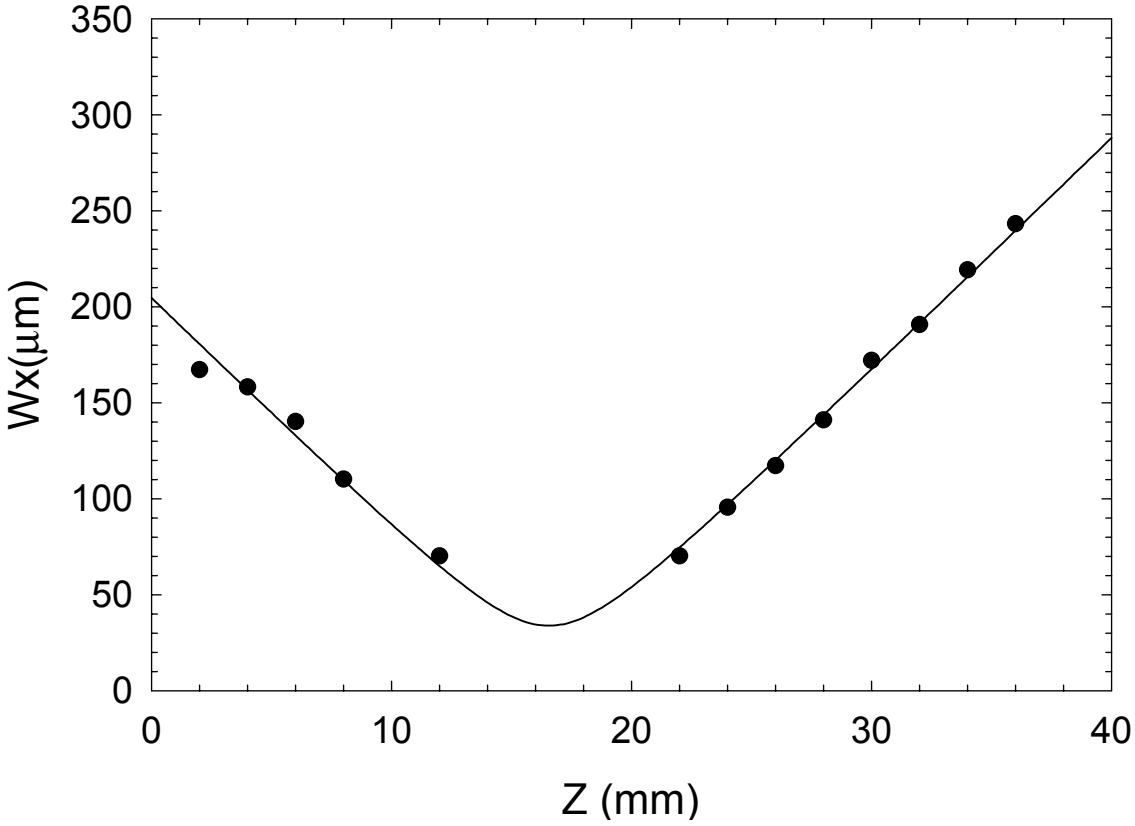

Figure 5-5 Knife-edge measurement of laser beam focusing spot size at 1064nm inside water using a M^2 factor method. Focal spot diameter: 33.8μm; M^2=1.21. A 3mm diameter collimated beam was focused through an f=75mm plano-convex bk7 glass lens in the middle of the water cell. The Spiricon CCD beam profiler was used to observe the transmitted beam. Two 1º bk7 glass wedges were used to reduce pulse energy. Pulse energy: less than 0.5mJ; Q-switch delay 207μs; pulse duration: 9ns (011128.jnb.)

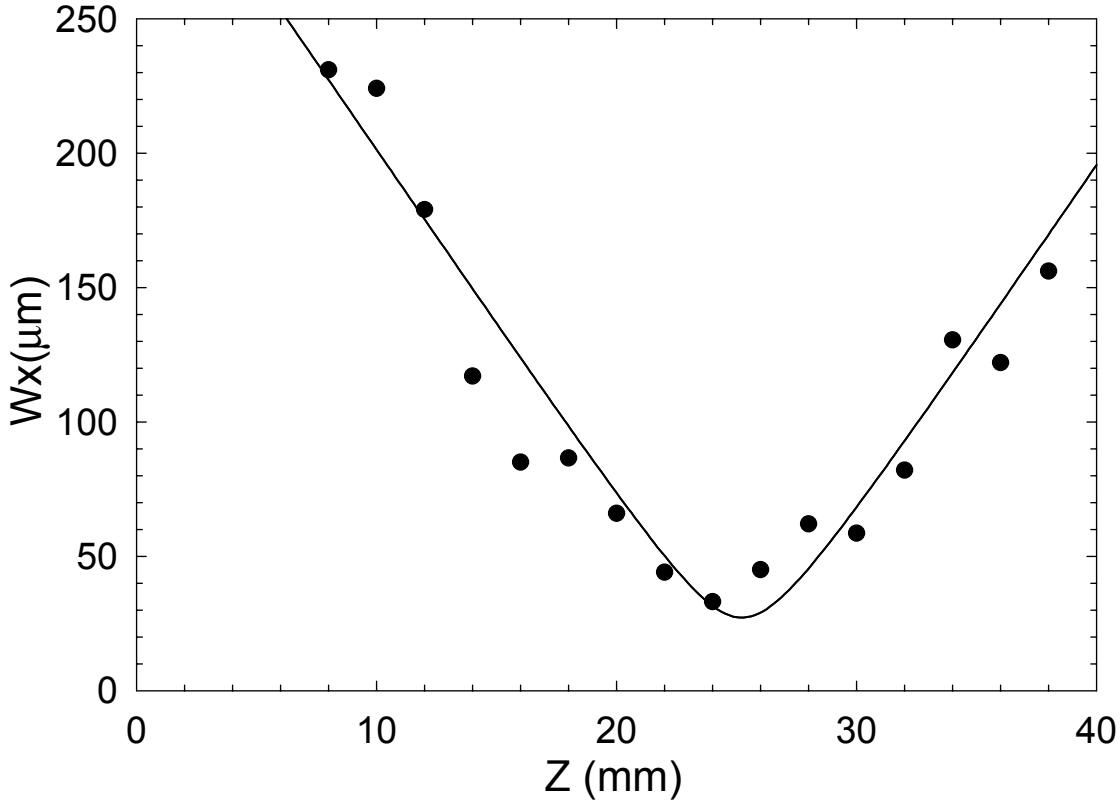

Figure 5-6 Knife-edge measurement of laser beam focusing spot size at 532nm inside water using a M^2 factor method. Focal spot diameter: 27.2μm; M^2=2.10. A 3mm diameter collimated beam was focused through an f=75mm plano-convex BK7 glass lens in the middle of the water cell. Two 1º BK7 glass wedges were used to reduce pulse energy. Pulse energy: less than 0.5mJ; Q-switch delay 207μs; pulse duration: 9ns (011128.jnb.)

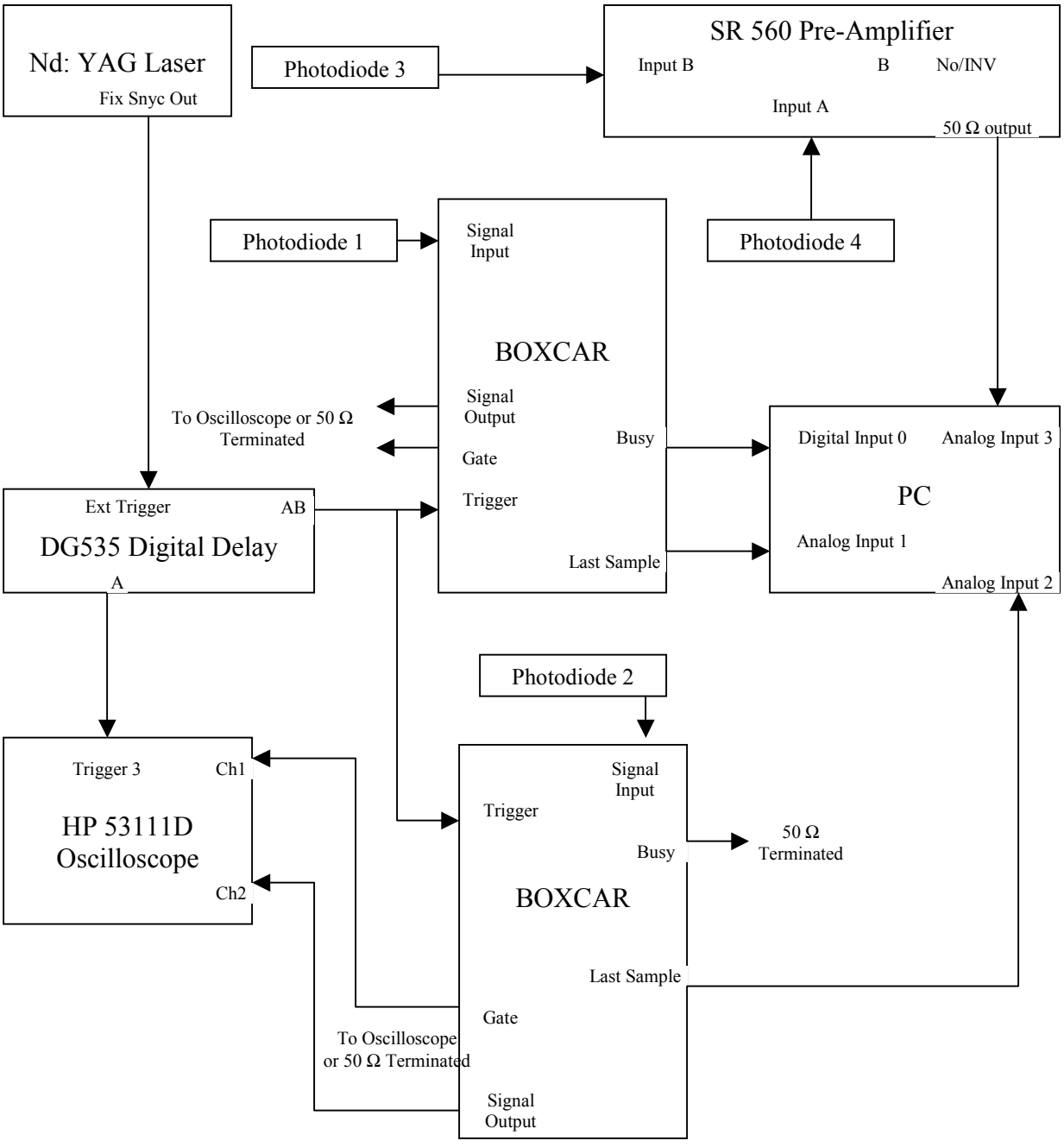

Figure 5-7 Electrical system setup of the backscattering measurement;

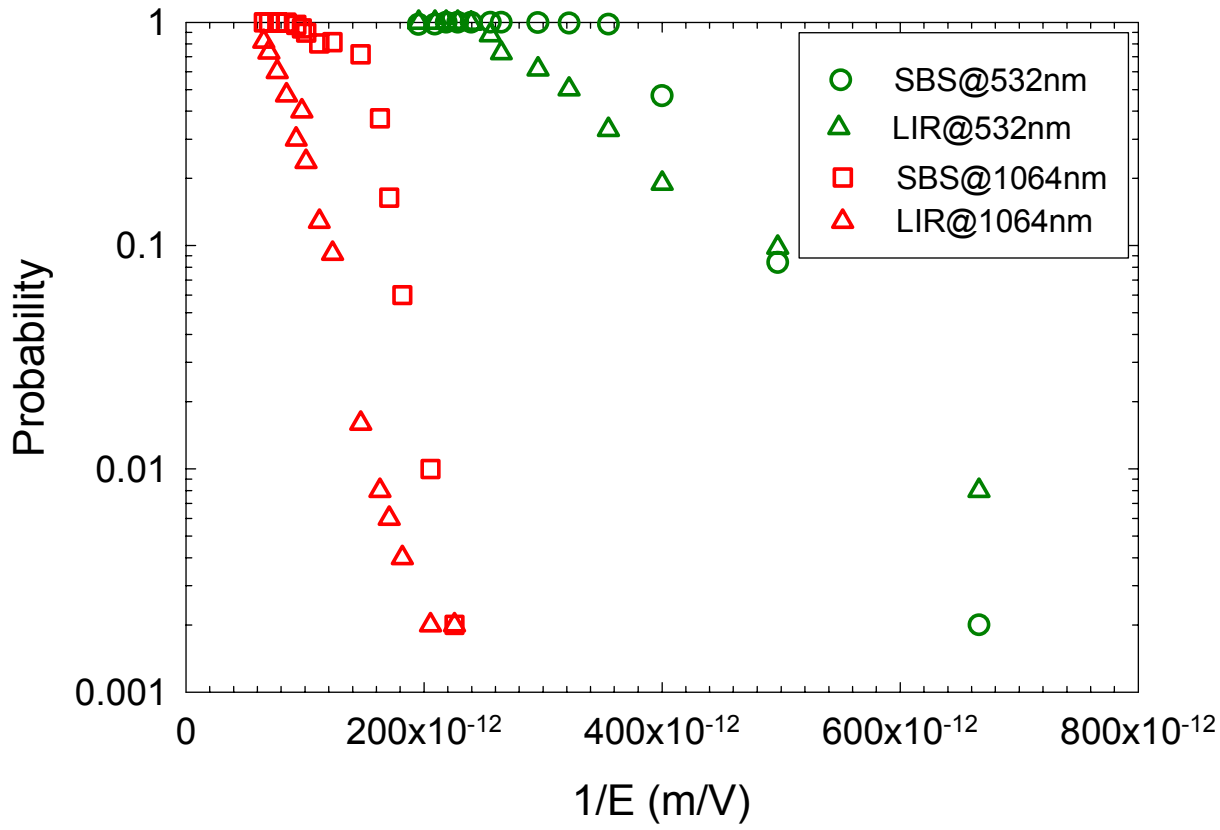

Figure 5-8 Comparison of SBS and LIR probability vs. laser electric field at 532nm;

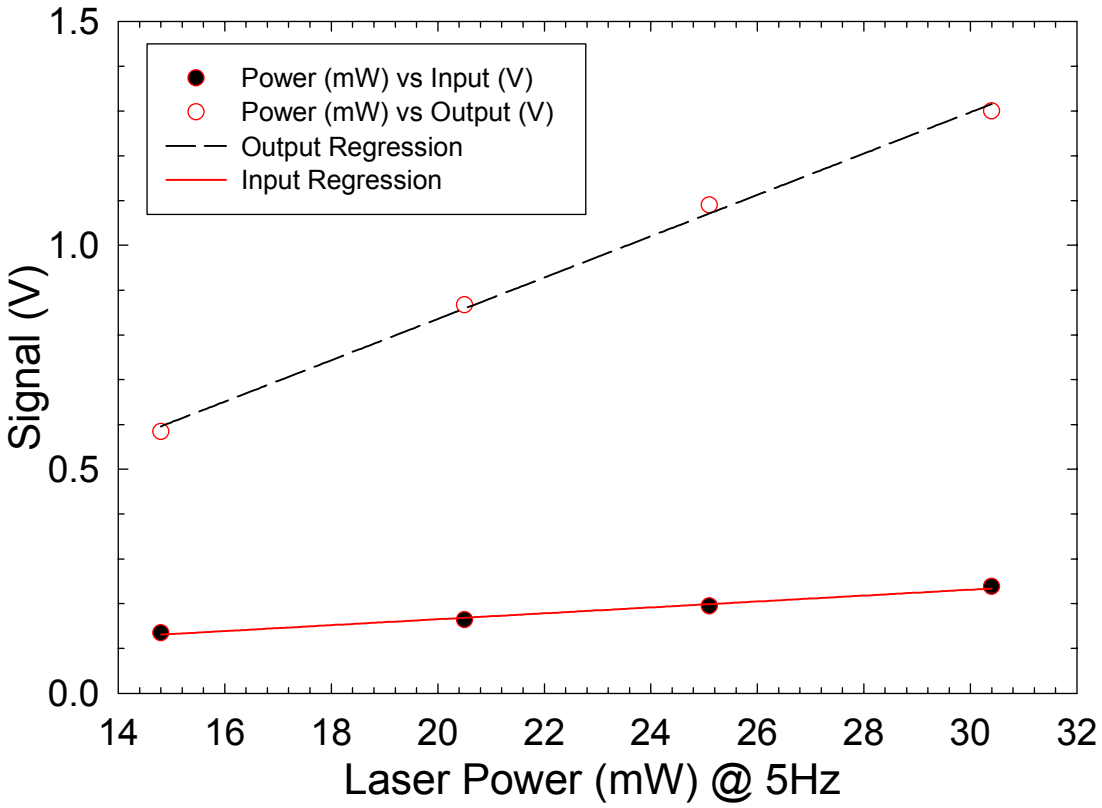

Figure 5-9 Verifying the linearity of the n_2 measurement at 1064nm;

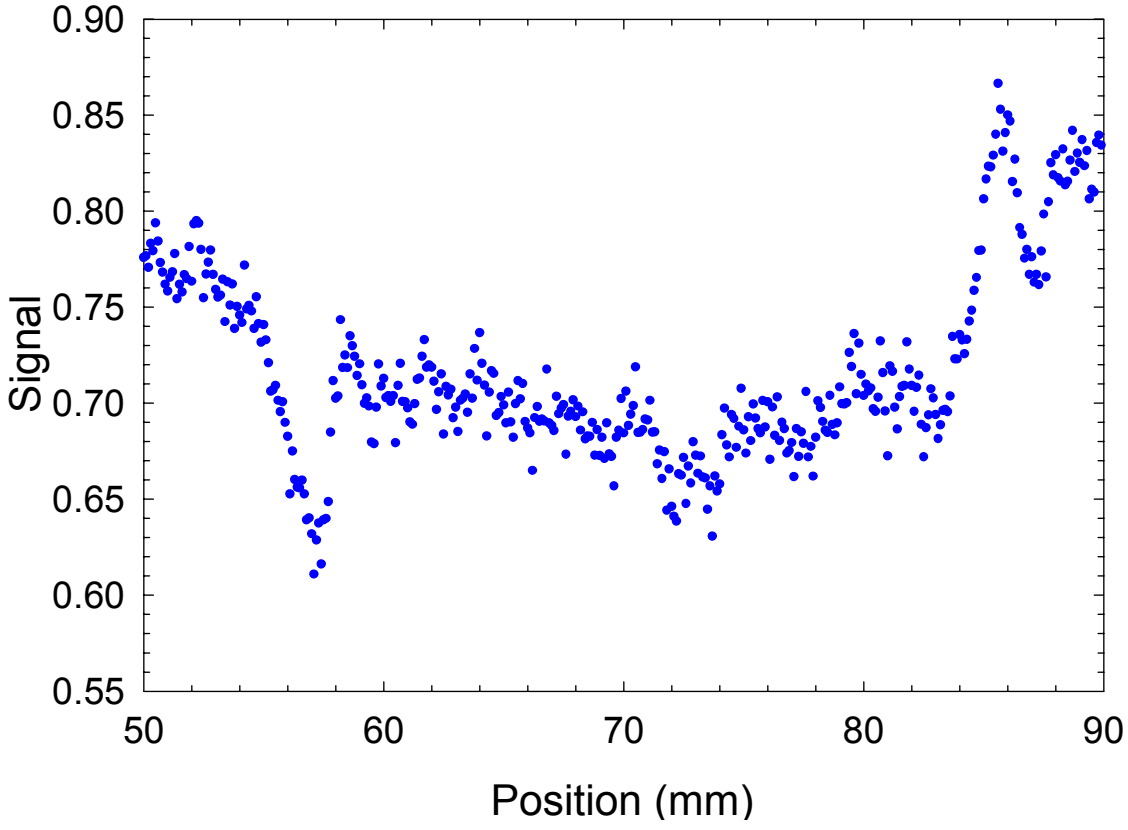

Figure 5-10 z-scan measurement of n_2 at 532nm, pulse energy was 0.24mJ; Q-switch delay was 270μs (010531.jnb.)

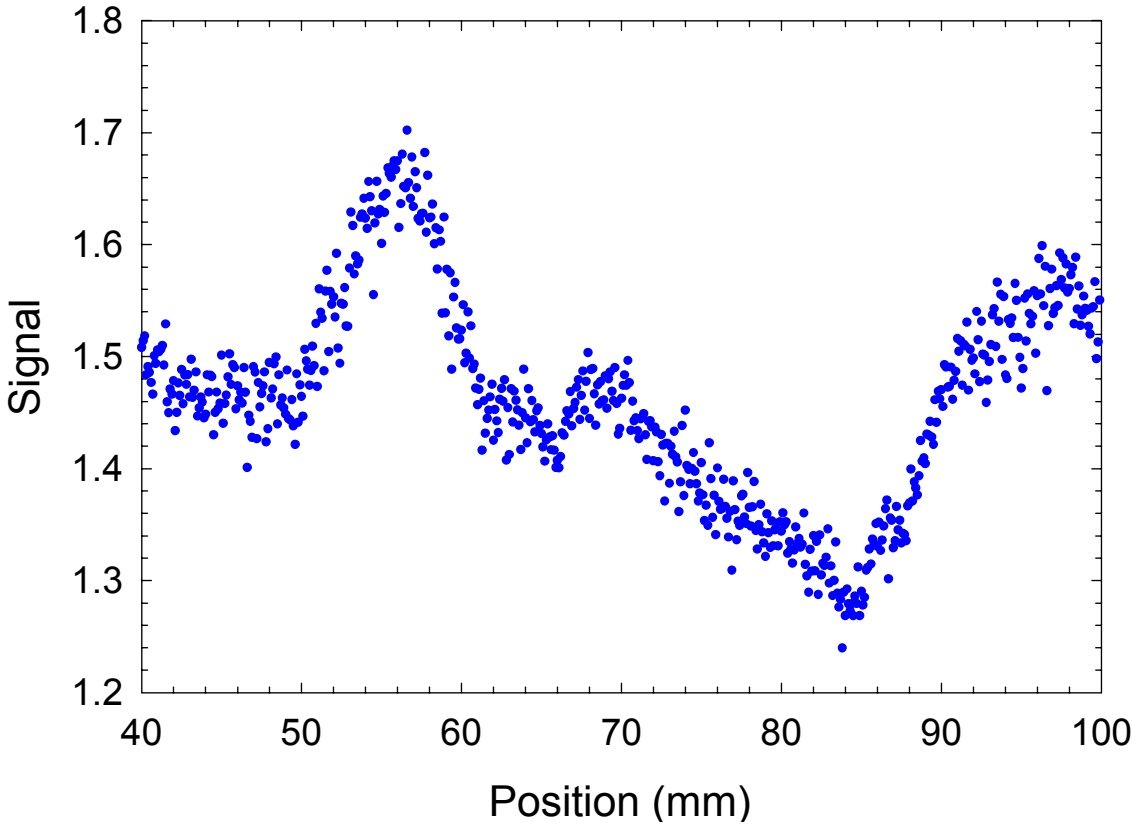

Figure 5-11 z-scan measurement of n_2 at 1064nm, pulse energy was 0.50mJ; Q-switch delay was 270μs (010528.jnb.)

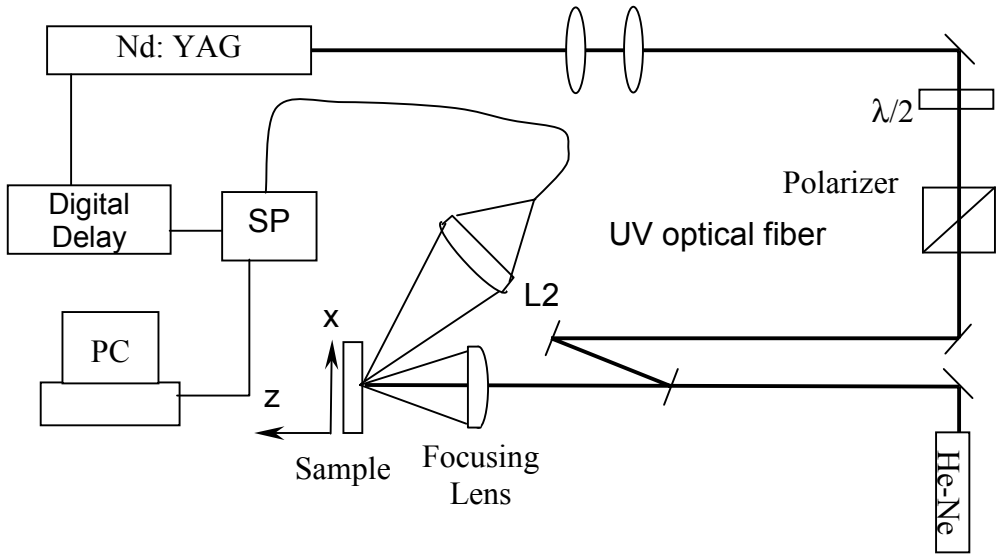

Figure 5-12 Schematic of the gelatin ablation probability measurement. SP: fiber optics spectrophotometer;

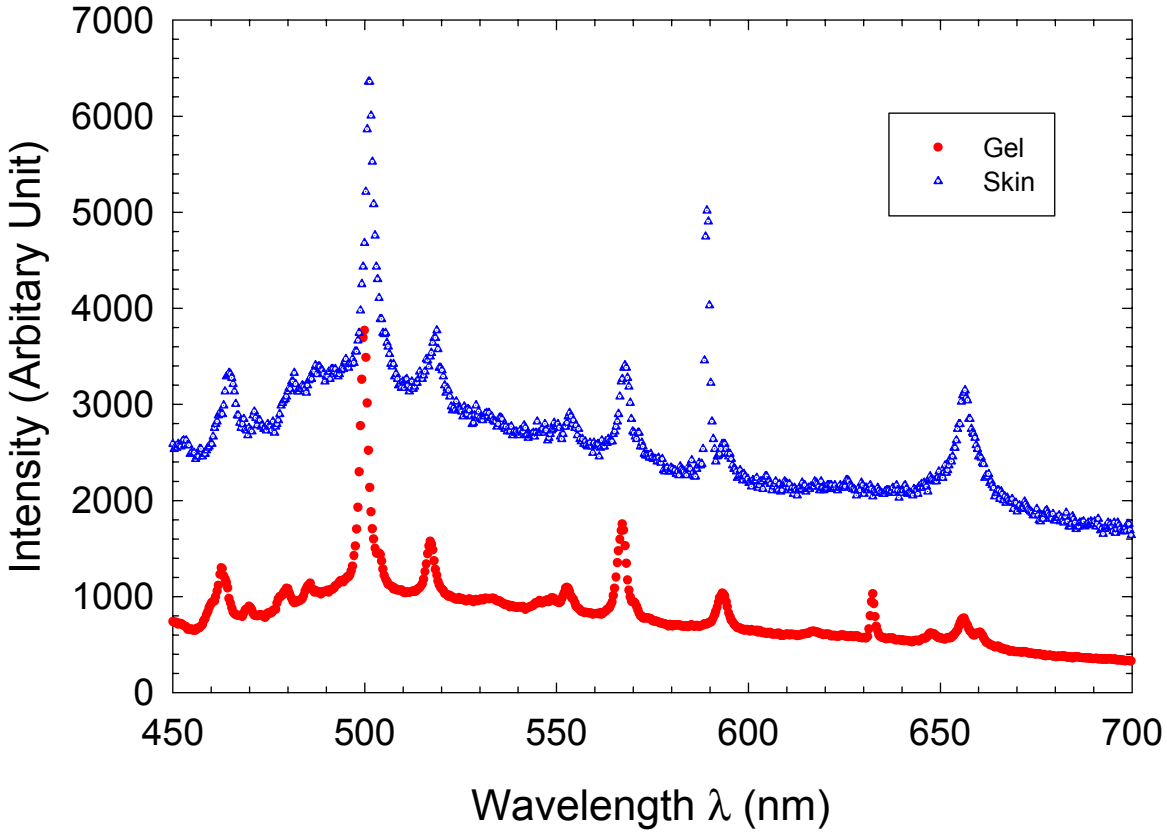

Figure 5-13 Secondary radiation spectra from the optical breakdown of the gelatin surface;

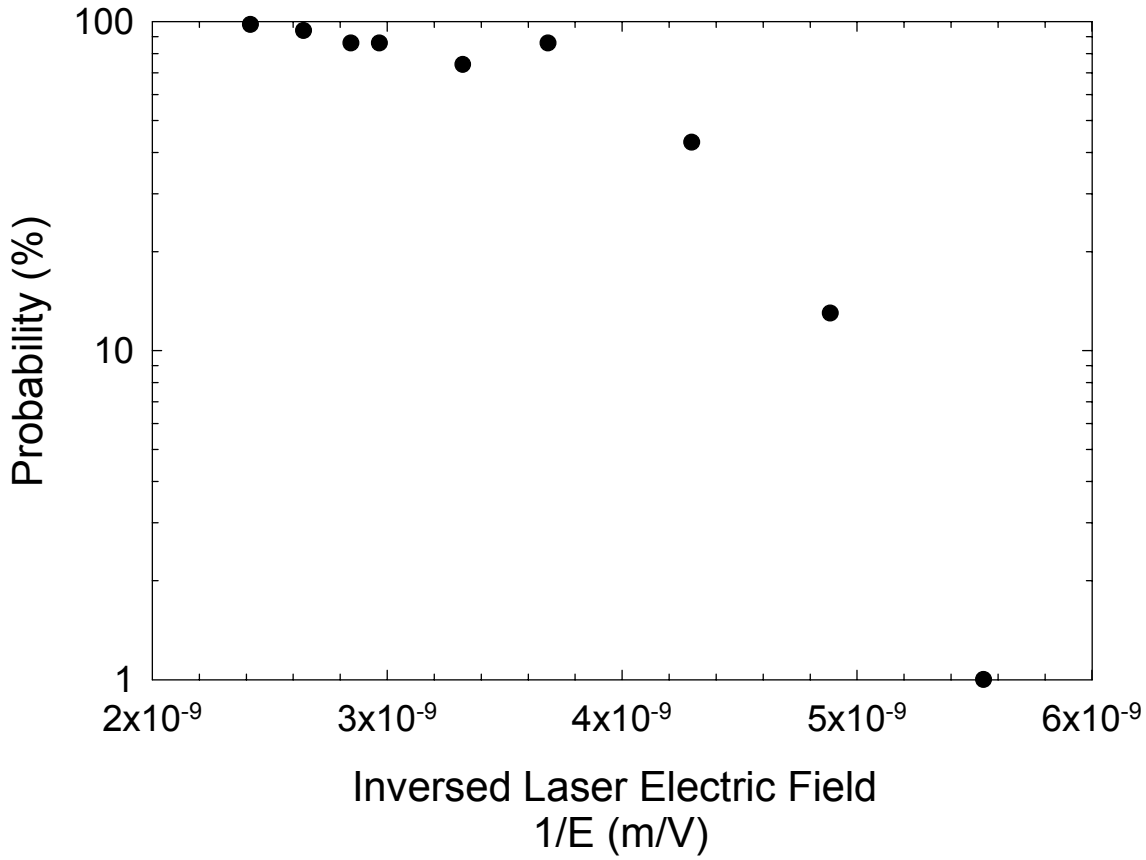

Figure 5-14 Probability of optical breakdown of plain gelatin (not doped) as a function of the laser electrical field;

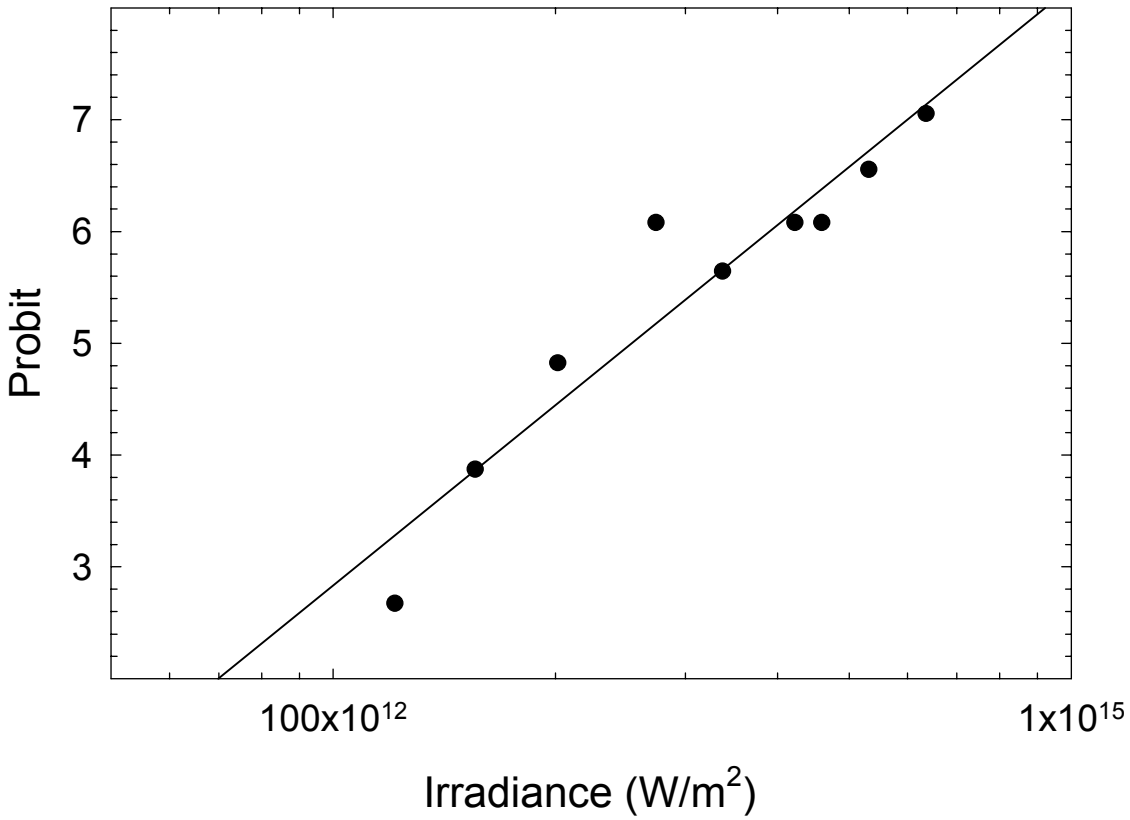

Figure 5-15 Probit analysis of the plain gelatin (not doped) ablation probability as a function of laser electrical field.

Chapter 6 Summary

In this dissertation, a quantitative study of soft tissue ablation by nanosecond laser pulses is presented. This study is a part of ongoing research effort in the Biomedical Laser Laboratory at East Carolina University to investigate major pathways and parameters of energy transfer, which are fundamental to the understanding of interaction mechanisms both experimentally and theoretically. As a result of this investigation, it is identified that the ambiguity of the fundamental mechanism underlying tissue ablation by nanosecond laser pulses is, to a large extent, related to the lack of quantitative studies of the ablation process near the threshold. The ablation of fresh porcine skin tissue has been studied experimentally *in vitro*. Based on these experimental results, a new plasma model was developed to model the observed phenomena and experimental data.

Early studies of tissue ablation have led to three major models: the photothermolysis model and its variations, the photochemical model, and the plasma mediated model. The selective photothermolysis model has been advanced and widely used to explain the ablation of soft tissue and pigments by laser pulses in terms of photothermal damage and relaxation. The photothermal mechanism was further investigated in the inertial confinement model ~~that~~ considering the thermoelastic deformation within the illuminated tissue resulted from nonuniform temperature distribution. The photochemical model, on the other hand, conjectures that the pressure increase is a result of photochemical dissociation of the macromolecular bonds due the large photon energy of deep ultraviolet light. Both models consider the absorption of laser light energy by the tissue is necessary

to initiate the ablation and they take into account the various thermal and mechanical effects. None of these models takes into account of the possible contribution from nanosecond laser induced plasma and thus cannot explain ablation of weakly absorbing tissues. In contrast, plasma formation or optical breakdown in tissue caused by the strong electromagnetic field of the short laser pulses has been assumed, in the plasma-mediated ablation model, to induce tissue ablation. Light absorption can be accomplished by the induced plasma and therefore, ablation of nonabsorbing tissue becomes possible. The limitations of the plasma-mediated model, however, lies in the negligence of the tissue absorption, which prevents its application in skin tissue ablation by nanosecond laser pulses at wavelengths of significant tissue or pigment absorption.

Consequently, a new plasma ablation models is developed to combine the concepts from the existing photothermal models and the plasma-mediated model. Specifically, the rate equation approach in the plasma-mediated model has been adopted as the framework of this new model. Considering the complexity of skin tissue components, the strong absorption from chromophores proposed by the selective photothermolysis and the confinement of the mechanical and thermal response by the inertial confinement model, the laser-induced localized thermal ionization rate is calculated from the sudden rise in temperature confined within the chromophores. The modified theoretical model is then evaluated with the experiment conditions for ablation of skin tissue by nanosecond laser pulses. It is found that the localized thermal ionization plays a significant role during plasma formation and greatly affects the optical breakdown thresholds.

In the experimental study of porcine skin tissue ablation by nanosecond laser pulse, the spectral line at 589nm from sodium atoms was identified as the signature of tissue ablation by nanosecond laser pulses at 1064, 532, 266 and 213nm. With this optical signature, the probabilistic nature of the ablation process near the thresholds was determined and measured the ablation probability as a function of laser rms electric field $\mathcal{E}$ by $P \sim \exp(-K^2/\mathcal{E}^2)$, at the four ablating wavelengths, which indicates the dominance ablation mechanism is cascade ionization. The ablation thresholds were obtained from the probability measurements and a monochromatic dependence on the ablation wavelength was found to be consistence with the prediction of the localized thermal ionization model.

It have been established experimentally that backscattered light due to stimulated Brillouin scattering (SBS) provides a more sensitive signature than laser induced secondary radiation (LIR) for determining the breakdown thresholds in water through simultaneous measurement of both the SBS and LIR signals at 1064 and 532nm with 10ns pulses. Furthermore, the nonlinear refraction index n_2 of water was measured at 1064 and 532nm using a z-scan technique to determine the electric and thermal contributions to the nonlinear index which may be used to interpret the results on optical breakdown in water.

In the new plasma ablation model, the physical and optical properties of the chromophores in skin tissue such as their density, absorption coefficients etc. are not available and rough approximations have been made. Consequently, studying ablation

process using a tissue phantom that has chromophores with known concentration, absorption and scattering properties is desired to enable establishing quantitatively the contribution of different chromophores in real tissue. It is for this purpose a preliminary study on a gelatin based tissue phantom was conducted. The experimental results on gelatin samples without doping of the chromophores show probabilistic behaviors similar to that from skin tissue. It was also found that doping of different concentrations of Indian ink as chromophores can decrease the ablation threshold by at least one order of magnitude. Future studies on tissue phantoms with absorption and/or scattering properties similar to skin are consequently planned. Numerical simulation of the localized thermal ionization process is also desired.

Bibliography

D. Albagli, B. Banish, M. Dark, G. S. Janes, C. Vonrosenberg, L. Perelman, I. Itzkan and M. S. Feld (1994). "Interferometric Surface Monitoring of Biological Tissue to Study Inertially Confined Ablation." Lasers in Surgery and Medicine **14**(4): 374-385.

D. Albagli, M. Dark, L. T. Perelman, C. Vonrosenberg, I. Itzkan and M. S. Feld (1994). "Photomechanical Basis of Laser-Ablation of Biological Tissue." Optics Letters **19**(21): 1684-1686.

D. Albagli, M. Dark, C. Vonrosenberg, L. Perelman, I. Itzkan and M. S. Feld (1994). "Laser-Induced Thermoelastic Deformation - a 3-Dimensional Solution and Its Application to the Ablation of Biological Tissue." Medical Physics **21**(8): 1323-1331.

D. Albagli, L. T. Perelman, G. S. Janes, c. Von Rosenberg, I. Itzkan and M. S. Feld (1994). "Inertially confined ablation of biological tissue." Lasers in the Life Sciences **6**(1): 55-68.

R. Rox Anderson and John A. Parrish (1981). "The Optics of Human Skin." Journal of Investigative Dermatology **77**(1): 13-19.

R. Rox; Anderson and John A. Parrish (1983). "Selective Photothermolysis: Precise Microsurgery by Selective Absorption of Pulsed Radiation." Science **220**: 524-527.

Neil W. Ashcroft and N. David Mermin (1976). Solid state physics. New York,, Holt Rinehart and Winston.

Peter A.; Barnes and K. E. Rieckhoff (1968). "Laser Induced Underwater Sparks." Applied Physics Letters **13**(8): 282-284.

Thomas H. Bartell and Thomas A. Mustoe (1987). "Animal Models of Human Tissue Expansion." Plastic and Reconstructive Surgery **83**(4): 681-686.

Nicolaas Bloembergen (1974). "Laser-Induced Electric Breakdown in Solids." IEEE Journal of Quantum Electronics **10**(3): 375-386.

Mickael J. Cariveau and East Carolina University. Dept. of Biology. (2000). The interaction of laser radiation with epithelial and dermal tissue.

P. B. Chapple, J. Staromlynska, J. A. Hermann, T. J. Mckay and R. G. Mcduff (1997). "Single-beam Z-scan: measurement techniques and analysis." Journal of Nonlinear Optical Physics and Materials **6**(3): 251-293.

Wai-Fung Cheong, Scott A. Prahl and Ashley J. Welch (1990). "A Review of the Optical Properties of Biological Tissues." IEEE Journal of Quantum Electronics **26**(12): 2166-2185.

Claudio DeMichelis (1969). "Laser Induced Gas Breakdown: A Bibliographical Review." IEEE Journal of Quantum Electronics **5**(4): 188-202.

Thomas F. Deutsch (1991). IR-Laser Ablation in Medicine: Mechanisms and Applications. Laser Ablation Mechanisms and Applications, Oak Ridge, TN, Springer-Verlag.

F. Docchio, C. A. Sacchi and J. Marcshall (1986). "Experimental Investigation of Optical Breakdown in Ocular Media under Single Pulse Irradiation with different Pulse Durations." Lasers in Ophthalmology **1**(2): 83-93.

Y. Du, X. H. Hu, M. Cariveau, X. Ma, G. W. Kalmus and J. Q. Lu (2001). "Optical properties of porcine skin dermis between 900 nm and 1500 nm." Physics in Medicine and Biology **46**(1): 167-181.

D. J. Finney (1971). Probit analysis. Cambridge [Eng.], University Press.

J. G. Fujimoto, W. Z. Lin, E. P. Ippen, C. A. Puliafito and R. F. Steinert (1985). "Time-resolved studies of Nd:YAG laser-induced breakdown. Plasma formation, acoustic wave generation, and cavitation." Investigative Ophthalmology & Visual Science **26**(12): 1771-1777.

R. Van Hillegersberg (1997). "Fundamentals of Laser Surgery." European Journal of Surgery **163**: 3-12.

X. H. Hu, Q. Y. Fang, M. J. Cariveau, X. N. Pan and G. W. Kalmus (2001). "Mechanism study of porcine skin ablation by nanosecond laser pulses at 1064, 532, 266, and 213 nm." Ieee Journal of Quantum Electronics **37**(3): 322-328.

X. H. Hu and T. Juhasz (1996). "Study of corneal ablation with picosecond laser pulses at 211 nm and 263 nm." Lasers in Surgery and Medicine **18**(4): 373-380.

William Hughes (1979). Aspects of biophysics. New York, Wiley.

C. L. M.; Ireland, A.; Yi, J. M.; Aaron and C. Grey Morgan (1974). "Focal-length dependence of air breakdown by a 20-psec laser pulse." Applied Physics Letters **24**(4): 175-177.

Akira Ishimaru (1978). Wave propagation and scattering in random media. New York, Academic Press.

I. Itzkan, D. Albagli, M. L. Dark, L. T. Perelman, C. Vonrosenberg and M. S. Feld (1995). "The Thermoelastic Basis of Short Pulsed-Laser Ablation of Biological Tissue." Proceedings of the National Academy of Sciences of the United States of America **92**(6): 1960-1964.

Joseph A. Izatt, Douglas Albagli, Matthew Britton, Jay M. Jubas, Irving Itzkan and Michael S. Feld (1991). "Wavelength Dependence of Pulsed Laser Ablation of Calcified Tissue." Lasers in Surgery and Medicine **11**: 238-249.

Steven L. Jacques and Daniel J. McAuliffe (1991). "The Melanosome: Threshold Temperature for Explosive Vaporization and Internal absorption Coefficient During Pulsed Laser Irradiation." Photochemistry and Photobiology **53**(6): 769-775.

T. Juhasz, H. Frieder, R. M. Kurtz, C. Horvath, J. F. Bille and G. Mourou (1999). "Corneal refractive surgery with femtosecond lasers." Ieee Journal of Selected Topics in Quantum Electronics **5**(4): 902-910.

T. Juhasz, X. H. Hu, L. Turi and Z. Bor (1994). "Dynamics of Shock-Waves and Cavitation Bubbles Generated By Picosecond Laser-Pulses in Corneal Tissue and Water." Lasers in Surgery and Medicine **15**(1): 91-98.

L. V. Keldysh (1965). "Ionization in the Field of a Strong Electromagnetic Wave." Soviet Physics JETP **20**(5): 1307-1314.

P. K. Kennedy (1995). "A First-Order Model For Computation of Laser-Induced Breakdown Thresholds in Ocular and Aqueous-Media .1. Theory." IEEE Journal of Quantum Electronics **31**(12): 2241-2249.

P. K. Kennedy, S. A. Boppart, D. X. Hammer, B. A. Rockwell, G. D. Noojin and W. P. Roach (1995). "A First-Order Model For Computation of Laser-Induced Breakdown Thresholds in Ocular and Aqueous-Media .2. Comparison to Experiment." IEEE Journal of Quantum Electronics **31**(12): 2250-2257.

Moishe S. Kitai, Valery L. Popkov, Vladimir A. Semchishen and Alexei A. Kharizov (1991). "The Physics of UV Laser Cornea Ablation." IEEE Journal of Quantum Electronics **27**(2): 302-307.

N. Kollias, R. M. Sayre, L. Zeise and M. R. Chedekel (1991). "Photoprotection by melanin." Journal of Photochemistry & Photobiology. B - Biology **9**(2): 135-60.

Robert M. Lavker, Gang Dong, Peishu Zheng and George F. Murphy (1990). "Hairless Micropig Skin." American Journal of pathology **138**(3): 687-697.

Shun Lee and Apostolos G. Doukas (1999). "Laser-Generated Stress Waves and Their Effects on the Cell Membrane." IEEE Journal of Selected Topics in Quantum Electronics **5**(4): 997-1003.

Annamarie Lembares (1997). Study of Soft Tissue Interaction with Optical Radiation. Physics. Greenville, NC, East Carolina University**:** xiii, 80 leaves.

Frieder H.; Loesel, Markolf H.; Niemz, Josef F.; Bille and Tibor Juhasz (1996). "Laser-Induced Optical Breakdown on Hard and Soft Tissues and Its Dependence on the Pulse Duration: Experiment and Model." IEEE Journal of Quantum Electronics **32**(10): 1717-1722.

Kazuo Morigaki (1999). Physics of amorphous semiconductors. London, Imperial College Press.

Essam Nasser (1971). Fundamentals of gaseous ionization and plasma electronics. New York,, Wiley-Interscience.

Mark H. Niemz, Edward G. Klancnik and Josef F. Bille (1991). "Plasma-Mediated Ablation of Corneal Tissue at 1053nm Using a Nd:YLF Oscillator/Regenerative Amplifier Laser." Lasers in Surgery and Medicine **11**: 426-431.

J. Noack and A. Vogel (1999). "Laser-induced plasma formation in water at nanosecond to femtosecond time scales: Calculation of thresholds, absorption coefficients, and energy density." Ieee Journal of Quantum Electronics **35**(8): 1156-1167.

Lars; Ojamae, Jorgen; Tegenfeldt, Jan; Lindgren and Kersti Hermansson (1992). "Simulation of Band Widths in Liquid Water Spectra. The Breakdown of the Frozen-Field Approximation." Chemical Physics Letters **195**(1): 97-103.

Alexander A.; Oraevsky, Rinat O.; Esenaliev and Vladilen S. Letokhov (1992). Pulsed Laser Ablation of Biological Tissue: Review of the Mechanisms. Laser Ablation: Mechanisms and Applications, Oak Ridge, Tennessee, Springer-Verlag.

Alexander A. Oraevsky, Steven L. Jacques and Frank K. Tittel (1995). "Mechanism of Laser Ablation for Aqueous Media Irradiated Under Confined-Stress Conditions." Journal of Applied Physics **78**(2): 1281-1290.

Daniel Palanker, Igor Turovets and Aaron Lewis (1997). "Electrical alternative to pulsed fiber-delivered lasers in microsurgery." Journal of Applied Physics **81**(11): 7673-7680.

G. Paltauf and H. Schmidtkloiber (1995). "Model Study to Investigate the Contribution of Spallation to Pulsed-Laser Ablation of Tissue." Lasers in Surgery and Medicine **16**(3): 277-287.

G. Paltauf and H. SchmidtKloiber (1996). "Microcavity dynamics during laser-induced spallation of liquids and gels." Applied Physics a-Materials Science & Processing **62**(4): 303-311.

John A. Parrish and Thomas F. Deutsch (1984). "Laser Photomedicine." IEEE Journal of Quantum Electronics **20**(12): 1386-1396.

G. H. Pettit and M. N. Ediger (1993). "Pump/Probe Transmission Measurement of Corneal Tissue During Excimer Laser Ablation." Lasers in Surgery and Medicine **13**: 363-367.

G. H. Pettit and R. Sauerbrey (1993). "Pulsed Ultraviolet Laser Ablation." Applied Physics A. **56**: 51-63.

E.; Reichel, H.; Schmidt-Kloiber, H.; Schoffmann, G.; Dohr and A. Eherer (1987). "Interaction of Short Laser Puleses with Biological Strutures." Optics and laser Technology **19**(1): 40-44.

B. K. Ridley (1983). "Lucky-drift mechanism for impact ionisation in semiconductors." Journal of Physics C. Solid State Physics **16**: 3373-3388.

C. A. Sacchi (1991). "Laser-Induced Electric Breakdown in Water." Journal of Optical Society of America B **8**(2): 337-345.

Ujwal S. Sathyam, Alan Shearin, Edward A. Chasteney and Scott A. Prahl (1996). "Threshold and ablation efficiency studies of microsecond ablation of gelatin under water." Lasers in surgery and Medicine **19**: 397-406.

K. Sentrayan, A. Thorpe Jr. and C. O. Trouth (1998). "Non-thermal Laser Ablation Model for Micro-Surgical Applications." Spectroscopy Letters **3**(13): 559-572.

Y. R. Shen (1984). The Principles of Nonlinear Optics. New York, Wiley.

A. E. Siegman (1990). "New developments in laser resonator." SPIE Proceedings **1224**: 2-14.

A. E. Siegman, M. W. Sasnett and T. F. Johnston (1991). "Choice of clip levels for beam width measurements using knife-edge techniques." IEEE Journal of Quantum Electronics **27**(4): 1098-1104.

W. Lee Smith (1978). "Laser-Induced Breakdown in Optical Materials." Optical Engineering **17**(5): 489-503.

R. Srinivasan (1986). "Ablation of polymers and biological tissue by ultraviolet lasers." Science **234**(31, October): 559-565.

R. Srinivasan, B. Braren, R. W. Dreyfus, L. Hadel and D. E. Seeger (1986). "Mechanism of the Ultraviolet Laser Ablation of Polymethyl Methacrylate at 193 and 248nm: Laser-induced Fluorescence Analysis, Chemical Analysis, and Doping Studies." Journal of Optical Society of America B **3**(5): 785-791.

David Stern, robert W. Schoenlein, Carmen A. Puliafito, Ernest T. Dobi, Reginald Birngruber and James G. Fujimoto (1989). "Corneal Ablation by Nanosecond, Picosecond, and femtosecond Lasers at 532 and 625nm." Arch Ophthalmol **107**(April): 587-592.

J. Tauc (1974). Amorphous and liquid semiconductors. London, New York,, Plenum.

V. T. Tikhonchuk, J. Fuchs, C. Labaune, S. Depierreux, S. Huller, J. Myatt and H. A. Baldis (2001). "Stimulated Brillouin and Raman scattering from a randomized laser beam in large inhomogeneous collisional plasmas. II. Model description and comparison with experiments." Physics of Plasmas **8**(5): 1636-1649.

M. J. C. van Gemert, Steven L. Jacques, H. J. C. M. Sterenborg and W. M. Star (1989). "Skin Optics." IEEE Transactions on Biomedical Engineering **36**(12): 1146-1154.

Martin J. C. van Gemert, Gerald W. Lucassen and A. J. Welch (1996). "Time Constants in Thermal Laser Medicine: II. Distributions of Time Constants and Thermal Relaxation of Tissue." Physics in Medicine and Biology **41**: 1381-1399.

Martin J. C. van Gemert and A. J. Welch (1989). "Time Constants in Thermal Laser Medicine." Lasers in Surgery and Medicine **9**: 405-421.

A. Vogel, K. Nahen, D. Theisen and J. Noack (1996). "Plasma formation in water by picosecond and nanosecond Nd:YAC laser pulses .1. Optical breakdown at threshold and superthreshold irradiance." Ieee Journal of Selected Topics in Quantum Electronics **2**(4): 847-860.

Ashley J. Welch and Martin J. C. van Gemert (1995). Optical-thermal response of laser-irradiated tissue. New York, Plenum Press.

A. J.; Welch, Massoud; Motamedi, sohi; Rastegar, Gerald L.; LeCarpentier and Duco Jansen (1991). “Laser Thermal Ablation.” Photochemistry and Photobiology **53**(6): 815-823.

Appendices

A.1 Laser Beam Spot Size

To determine the laser beam focusing spot size is critical in the experiments for calculating the correct laser fluence threshold or laser rms electric field. A single parameter standard called M^2 factor has been used in this dissertation research to determine the spot size. Details of the definition of the M^2 factor and its applications can be found in many literatures, and a brief description is given here mainly follows the work from A. E. Sigman [Siegman 1990].

The term "beam quality" is generally taken to mean some measure of the relationship between the near-field beam size and the far-field beam spread of a laser beam. The propagation of Gaussian beam in free space can be described as:

$$\tilde{u}(x,y,z) = \sqrt{\frac{2}{\pi}} \frac{e^{-j[kz-\psi(z)]}}{w(z)} e^{-\frac{x^2+y^2}{w^2(z)} - jk\frac{x^2+y^2}{2R(z)}} \tag{A.1}$$

where the irradiance I is:

$$I(x,y,z) = \left|\tilde{u}(x,y,z)\right|^2 . \tag{A.2}$$

The beam radius w along the optical axis z is:

$$w(z) = w_0\sqrt{1+(\frac{z}{z_R})^2} , \tag{A.3}$$

and the radius of the wave front curvature R(z) is given by:

$$R = z + \frac{z_R}{z} \tag{A.4}$$

It also gives

$$\psi(z) = \tan^{-1}(\frac{z}{z_R}), \tag{A.5}$$

and the wave vector k

$$k = \frac{\omega}{c} = \frac{2\pi}{\lambda}. \tag{A.6}$$

The e^{-2} definition of the Gaussian beam spot size is the pulse radius that includes 85.6% of the total energy as shown in. If the irradiance of the laser pulse at r with pulse width w and power P can be given from Eqs. (A.1) and (A.2) as:

$$I(r) = \frac{2P}{\pi w^2} e^{-2\frac{r^2}{w^2}}, \tag{A.7}$$

The total power inside a radius a is

$$\begin{aligned} P_t(a) &= \tfrac{2P}{\pi w^2} \int_0^a 2\pi r e^{-2\frac{r^2}{w^2}} dr \\ &= P(1 - e^{-2\frac{a^2}{w^2}}) \end{aligned}. \tag{A.8}$$

Hence, the total power inside spot size with radius w is

$$P_t = P(1 - e^{-2}) \approx 0.865P. \tag{A.9}$$

Another way to determine the spot size is to use a 90%-10% knife-edge method. The spot size under this definition is the distance between the knife-edge positions at 10% and 90% of the total power:

$$P_t(a) = \frac{2}{\pi w^2}\int_{-\infty}^{\infty} e^{-2\frac{y^2}{w^2}}dy\int_{-\infty}^{a} e^{-2\frac{x^2}{w^2}}dx$$
$$= \sqrt{\frac{2}{\pi}}\int_{-\infty}^{a} e^{-2\frac{x^2}{w^2}}dx \quad . \tag{A.10}$$
$$= \frac{1}{2}[1 - Erf(x_0\sqrt{2})]$$

Consequently, the difference between the two definitions is

$$w_{90\%-10\%} \approx 0.64 w_{1/e^{-2}} . \tag{A.11}$$

The laser beam variances in spatial space and in spatial-frequency space are

$$\sigma_x{}^2(z) = \frac{\iint (x-\bar{x})^2 I(x,y,z)dxdy}{\iint I(x,y,z)dxdy}$$
$$\sigma_{s_x}{}^2 = \frac{\iint (s_x-\bar{s}_x)^2 \hat{I}(s_x,s_y)ds_x ds_y}{\iint \hat{I}(s_x,s_y)ds_x ds_y} \quad . \tag{A.12}$$

$\sigma_x{}^2$ obeys the free space propagation rule:

$$\sigma_x{}^2(z) = \sigma_{x0}{}^2 + \lambda^2\sigma_{sx}{}^2(z-z_{0x})^2 , \tag{A.13}$$

where $\sigma_{x0}{}^2 = \sigma_x{}^2(z_x)$ is the spatial variance at beam waist $z_x = z_{x0}$. From uncertainty principle, for any laser beam it has been given:

$$\sigma_{x0}\sigma_{sx} = \frac{M_x{}^2}{4\pi} . \tag{A.14}$$

For Gaussian beam $M_x{}^2 = 1$,

$$I(x,y,z) = \frac{2P}{\pi w^2}e^{-2\frac{x^2+y^2}{w^2}}$$
$$I(s) = \frac{P}{2\pi}e^{-2\pi^2 w_0^2 s^2} \quad , \tag{A.15}$$

and

$$w_x^2(z) = w_{x0}^2 + \frac{\lambda^2}{\pi^2 w_{x0}^2}(z - z_{0x})^2 \tag{A.16}$$

where

$$\begin{aligned} w_x(z) &= 2\sigma_x(z) \\ w_{x0}(z = z_{0x}) &= 2\sigma_{x0}(z = z_{0x}) \end{aligned}. \tag{A.17}$$

For Non-Gaussian beam, $M_x^2>1$, where $M^2<1.5$ is considered as good beam quality. If non-Gaussian beam waist is defined using Eq. (A.17), the far field beam spot size is given by

$$W_x{}^2(z) = W_{x0}{}^2 + \frac{\lambda^2 M_x^2}{\pi^2 W_{x0}^2}(z - z_{0x})^2. \tag{A.18}$$

Therefore, if the far field beam waist w(z) is obtained through experiment, the beam quality M^2, waist position z and focal spot size $w_0(z)$ can be determined through fitting w(z) with z using Eq. (A.18).

A.2 Probit Analysis

The probit analysis is a commonly used statistical technique analyzing the measurement of the probabilities of certain events in response to some stimulus. A detail description of the probit analysis can be found in Finney's book [Finney 1971]. In probability measurement, there are two components to be considered, the stimulus and the response to it. If the characteristic response is quantal, its occurrence or non-occurrence will depend upon the intensity of the stimulus or dose applied. If a dose x0 is applied, the proportion of the occurrence P is given by:

$$P = \int_0^{x_0} f(x)\,dx, \tag{B.1}$$

where f(x) is called the distribution function of x. The measure of x is here assumed to be a quantity with a range from 0 to ∞, so that

$$\int_0^{\infty} f(x)\,dx = 1. \tag{B.2}$$

When a normal distribution of the x is available, the distribution function f can be characterized by two parameters, the mean μ and variance σ through

$$f(x) = \frac{1}{\sigma\sqrt{2\pi}} e^{-\left(\frac{x-\mu}{\sqrt{2}\sigma}\right)^2}, \tag{B.3}$$

where σ^2 is called the standard deviation. It is a bell shaped symmetry curve, which peaks at μ., as shown in Figure A-0-1. The corresponding probability P of the response to the dose x is then given by:

$$P(x) = \frac{1}{\sigma\sqrt{2\pi}} \int_{-\infty}^{x} e^{-\left(\frac{x-\mu}{\sqrt{2}\sigma}\right)^2} dx\,, \tag{B.4}$$

which is shown as the sigmoid curve in Figure A-0-1.

The probability of a response on a transformed scale is given by the normal equivalent deviate (N.E.D.). This response metameter is Y, defined by:

$$P = \frac{1}{\sqrt{2\pi}} \int_{-\infty}^{Y} \exp\{\frac{1}{2}u^2\}du \tag{B.5}$$

Hence, the N.E.D. of any value of P between 0 and 1 is defined as the abscissa corresponding to a probability P in a normal distribution with mean 0 and variance 1. Eq. (B.5) determines either of P and Y uniquely from the other. In order to eliminate the negative Y values, a slightly different definition of Y is used and called the probit of P, in which probit means the probability unit:

$$P = \frac{1}{\sqrt{2\pi}} \int_{-\infty}^{Y-5} \exp\{\frac{1}{2}u^2\}du\,. \tag{B.6}$$

The relation between the probit of the expected proportion of responses and the dose, corresponding to Eq. (B.6), is a linear equation as shown in Figure A-0-1:

$$Y = 5 + \frac{1}{\sigma}(x - \mu)\,. \tag{B.7}$$

For experimental results fit to the linear probit curve, the slop of the curves is the reciprocal of the variance, in which indicates different mechanisms that result in different normal distributions with different standard deviation. The distant between different parallel linear curves is determined by the mean value of the Gaussian distribution.

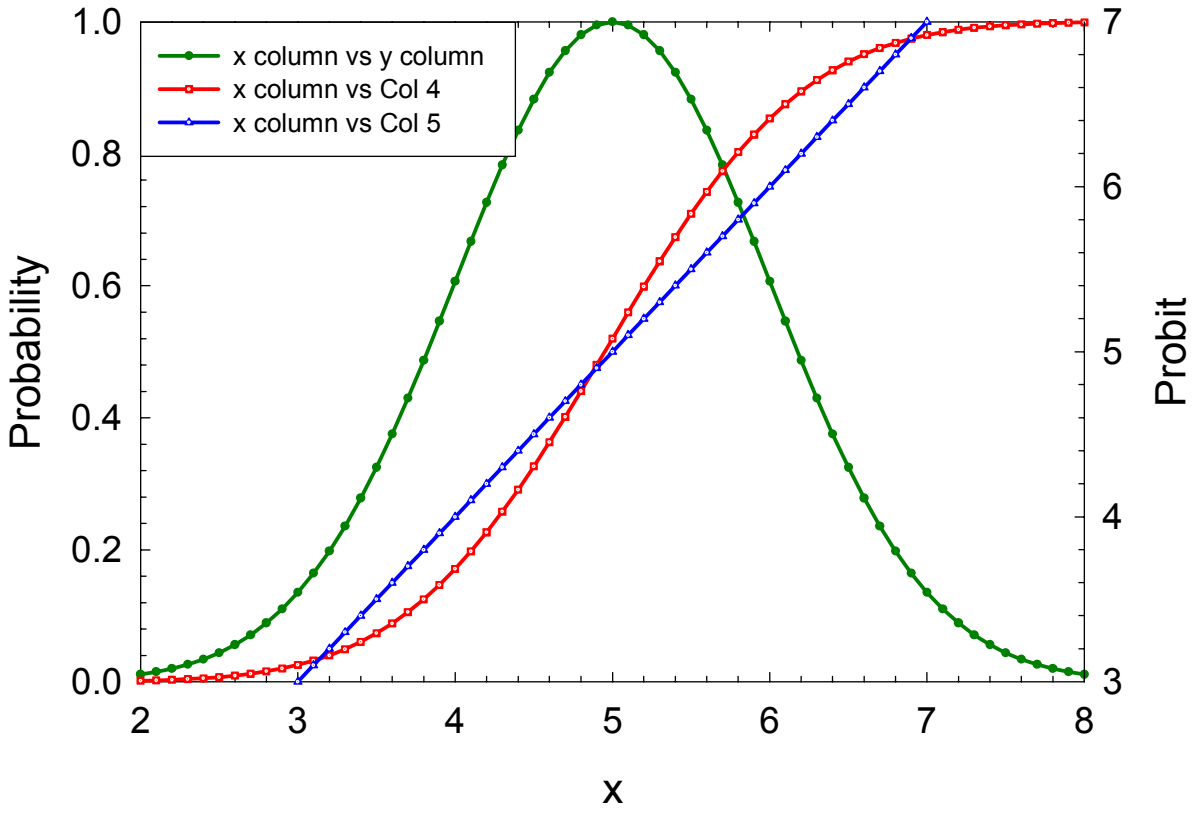

Figure A-0-1 Effect of the probit transformation. Mean m=5, variance s=1 (probit.jnb.)

A.3 Computer Programming Code

A.3.1 List of computer programs

Table A-1 List of computer programs used in this dissertation research

Name	Description	Original	Author	Date
Step5.bas	For experiments controlling two step motors (via DAS1602 board) to scan a photodiode in a plane perpendicular to the laser beam and read one signal from the A/D board per step of motor motion (via DAS1602 board).		Hu / Fang	9/98
Lockin.bas	Lock-in GBIP DAQ. For reading signal from Lock-in via GPIB488 board and draw data on screen at real time to monitoring. Function 4.	Step6.bas	Fang	7/00
backs3.bas	Backscattering & Flash DAQ with two Boxcar & Pre-Amplifier. Three A/D channels input for backscattering and N2 measurement. Function 9 for n2 z-scan measurement. Two A/D is falling edge triggered through the SRS 250 Boxcar integrator. Digital Output 1 is used for step motor output.	N2.bas	Fang	6/00
N2.bas	N2 DAQ with two Boxcar channel. Function 9 for n2 z-scan measurement. Two A/D is falling edge triggered through the SRS 250 Boxcar integrator. Digital Output 1 is used for step motor output.	Step.bas	Fang	6/00
DiodeLas.bas	Diode Laser DAQ with two step motor driving. Similar to Step9.	Step9.bas	Fang	6/00
ProjectOcean	Visual Basic program for transforming multiple OceanOptics spectrum file into one text formatted file for other programs to read.		Fang	6/00
Data.cpp	Diode Laser 3D Data processing	bmp.cpp		
ProjectN2	Visual Basic program. Backscattering & N2 threshold. Read data file generated by N2.bas or backs3.bas and set thresholds.		Fang	6/00

```
' program name: backs.bas
' (i)   reading conumber% data via CYDAS802 A/D board / CH0, continuously
'       plot on screen, or single shot with parameter input capability.
' (ii)  Drive step motor via CYDAS802 DIG1
' (iii) A/D with step motor control
' (iv)  A/D with external TTL trigger from CYDAS802 DIG Input 0
'       while driving step motor.

' by X.H.Hu, modification: June  05, 1997
' modified by Q.Y.Fang:    12-09-1998
'       added step motor control module:
'       "SUB moving()"
'       "SUB movestep()"
' modified by Q.Y.Fang:    03-23-2000
'       added data aquasition module for SRS 250 Boxcar integrator
'           from Stanford Research System
' modified by Q.Y.Fang:    04-17-2000
'       added step motor control module:
'       "SUB movestepnew()"
'       using 82C54 counter to generate square wave with precise pulse width.
' modified by Q. Y. Fang:  07-08-2000
'       add three channel A/D input for water backscattering
'       and n2 measurement
'       900 section similar to n2.bas for n2 z-scan measurment.

'$INCLUDE: 'CB.BI'          ' Mandatory INCLUDE file to access default
                            ' parameter values

DECLARE SUB delay (d1%)
DECLARE SUB delayA (d1%)
DECLARE SUB gaincnvt (gf!)
DECLARE SUB moving (stepsz%)
DECLARE SUB movestep (stepsize%)
DECLARE SUB CountOut (PulseWidth%)
DECLARE SUB movestepnew (distance%, PulseWidth%)

'$STATIC

        DefInt H-Z
        DECLARE SUB saving (startime$, stoptime$, st1$, totalsecond, J1%)
        DECLARE SUB GRAPHICSINITIALIZE (XMIN%, xmax%, Ymin%, Ymax%, XLABEL$,
YLABEL$)
        DECLARE SUB dproc (ADT%, Chan%)
        DECLARE SUB selemenu (ha%)
        DECLARE SUB procpara (st1$, Ymin%, Ymax%)
        DECLARE SUB adpara (d%)

        'DIM SHARED ADData%(2000)          'A/D data array Did not use
        Dim expara(600) As Single          'experimental parameter
        Dim indata0!(1000)                 'input signal data array
        Dim indata1!(1000)                 'input signal data array for A/D2
        Dim indata2!(1000)                 'hand input signal data array
```

```
        Dim conumber%                ' # of total data
        Dim Count&                   ' dsample=# of A/D sample per data
        Dim Rate&                    ' A/D sampling rate (#/s)
        Dim Gain%                    ' A/D actual gain
        Dim dactime As Single        ' time between data acquisition
        Dim svpointer                ' save pointer

        Dim HighChan%                ' Did not use
        Dim LowChan%                 ' Did not use

        Dim Thback As Single         ' Threshold of the reflection
        Dim Thtrans As Single        ' Threshold of the Spark
        Dim Thfls As Single          ' Threshold of the flash

        Dim Pback As Integer         ' Probability of the reflection
        Dim Ptrans As Integer        ' Probability of the Spark
        Dim Pfls As Integer          ' Probability of the flash

        Dim unitstep As Integer      ' unit step full=4 or half=2

        Dim ADChan0 As Integer       ' A/D channel 0
        Dim ADChan1 As Integer       ' A/D channel 1
        Dim ADChan2 As Integer       ' A/D channel 2
        Dim ADChan3 As Integer       ' A/D channel 3 as trigger

' parameter for reminding saving data
        Dim datacq As Integer        ' Number of data acquisition
        Dim datasav As Integer       ' Number of saved data set

        Dim ADT0 As Integer    ' parameter for A/D data from chan0
        Dim ADT1 As Integer    ' parameter for A/D data from Chan1
        Dim ADT2 As Integer    ' parameter for A/D data from chan2

        Dim ADVol0 As Single   ' parameter for A/D data from chan0
        Dim ADVol1 As Single   ' parameter for A/D data from chan1
        Dim ADVol2 As Single   ' parameter for A/D data from chan2
        Dim ADSum0 As Single   ' summation for A/D chan0
        Dim ADSum1 As Single   ' summation for A/D chan1
        Dim ADSum2 As Single   ' summation for A/D chan2

'default values
        Const BoardNum = 0     'Board number
        Gain% = UNI10VOLTS     'set the input range to 0-10 Volt
        ADChan0% = 0           ' A/D channel 0 to scan
        ADChan1% = 1           ' A/D channel 1 to scan
        ADChan2% = 2           ' A/D channel 2 to scan
        ADChan3% = 3           ' A/D Channel 3 to scan for trigger
'Change Channel
        LowChan% = 1           'first channel to scan
        HighChan% = 1          'last channel to scan
'End of Channel change

' Default values
```

```
        Count& = 10             ' total number of A/D data per scan
        Rate& = 20000           ' sampling rate (samples per second)

        conumber% = 100         'total number of data aquisition
        datasav% = 0
        datacq% = 0
        Ymin% = 0
        Ymax% = 4096
        dactime = 1             '1 sec between two data acquisition
        unitstep% = 4           'unit step at full step

'initilization of board with default values
CLS:        LOCATE 5, 1

' Declare UL Revision Level
        ULStat% = cbDeclareRevision(CURRENTREVNUM)

' Initiate error handling
'  activating error handling will trap errors like
'  bad channel numbers and non-configured conditions.
'  Parameters:
'    PRINTALL    :all warnings and errors encountered will be printed
'    DONTSTOP    :if an error is encountered, the program will not stop,
'                 errors must be handled locally

        ULStat% = cbErrHandling%(PRINTALL, DONTSTOP)
        If ULStat% <> 0 Then Stop

' If cbErrHandling% is set for STOPALL or STOPFATAL during the program
' design stage, Quick Basic will be unloaded when an error is encountered.
' We suggest trapping errors locally until the program is ready for compiling
' to avoid losing unsaved data during program design.  This can be done by
' setting cbErrHandling options as above and checking the value of ULStat%
' after a call to the library. If it is not equal to 0, an error has occurred.

        Print "This program read analog signal from CH0 of the CYDAS802 board."
        Print "The samples will be averaged to obtain data as a funtion of time."
        Print "The data can be plotted on screen as a function of time (mode 4)."
        Print "The input voltage range: 0.00 -- 10.00 (V)"
        Print
'calculate the voltage conversion factor from the voltage gain code

        Print "hit any key to continue. "
        Do While INKEY$ = "": Loop

'print menu
60  Call gaincnvt(gf!)
        Call selemenu(ha)
CLS:        LOCATE 10, 1

        'modification starts from here

        If ha = 7 Then GoTo 700         'Like 3 but with Step motor control
```

```
        If ha = 8 Then GoTo 800         'Like 4 but with Step motor control
        If ha = 9 Then GoTo 900         'Like 3 but continue
        'modification ends here by Fang 12-07-98

        If ha = 6 Then GoTo 1000        'Exit
        If ha = 1 Then GoTo 100         'A/D Parameter adjust
        If ha = 2 Then GoTo 200         'Data accquisition parameter adjust
        If ha = 3 Then GoTo 300         'Single data accquisition
        If ha = 4 Then GoTo 400         'continue data accquisition with plot
        If ha = 5 Then                  'Saving data
            If svpointer < 10 Then
                Print "there is nothing to save "
                Print "hit any key to main menu. "
                Do While INKEY$ = "": Loop
            Else
                GoTo 80
            End If
        End If
        GoTo 60

80  datasav% = datasav% + 1
        If svpointer = 10 Then K1% = j0%
        If svpointer = 20 Then K1% = J1%
        Call saving(startime$, stoptime$, st1$, totalsecond, K1%)
        GoTo 60

'change A/D parameters
100 Call adpara(d%)
        GoTo 60

'change data acquisition process parameters
200 Call procpara(st1$, Ymin%, Ymax%)
        GoTo 60

300 svpointer = 10          'pointer for saving data in single-shot mode
        datacq% = datacq% + 1
        CLS
        Print "single-shot data acquisition: hit any key when ready for next reading"
        Print "Press S key to stop the reading loop, press R key to redo last entry."
        Print "total number of reading <= "; conumber%
        Print
        Print "hit any key to proceed >> "
        Do While INKEY$ = "": Loop

        CLS                 'print the column title
        Print "sequnce"; Space$(5); "voltage reading (V)"; Space$(5), "parameter"

        For j0% = 0 To conumber% - 1
        INPUT "enter a parameter (S for stop, R for redo last entry): ", ik$

        If UCase$(ik$) = "S" Then
BEEP:       LOCATE 23, 10
        INPUT "STOP detected, enter: 1--continue, 2--main menu >> ", cc1%
```

```
        j0% = j0% - 1
            If cc1% = 2 Then GoTo 60 Else GoTo 380
        ElseIf UCase$(ik$) = "R" Then
        j0% = j0% - 2: GoTo 380
        Else
        expara(j0%) = Val(ik$)
        End If

        Call dproc(ADT0%, ADChan0%)
        indata0!(j0%) = ADT0%
        Print indata0!(j0%)
'converting into volt and be careful of overflow
        If Gain% < 10 Then
        ADVol0! = ((ADT0% - 2048) / 2048) * gf!
        Else
        ADVol0! = (ADT0% / 4096) * gf!
        End If

        Print j0% + 1; Space$(10); ADVol0!; Space$(10); expara(j0%)

380 Next j0%

        BEEP
        LOCATE 24, 10
        Print "Data acquissition is done.  Hit any key to main menu. "
        Do While INKEY$ = "": Loop
        GoTo 60

400
Rem     unitstep% = 2
Rem     stepsize% = 1

Rem     INPUT "Input step size (um): ", stepsize%
Rem     stepsize% = stepsize% / unitstep%

        average = 0

        INPUT "input waiting time (s): ", WaitTime
        dactime = WaitTime


        svpointer = 20          'saving pointer for continuous mode
        XMIN = 0:           xmax = conumber%
        XLABEL$ = "time":       YLABEL$ = "data"
        datacq% = datacq% + 1

        Screen 0: CLS
        Call GRAPHICSINITIALIZE(XMIN, xmax, Ymin%, Ymax%, XLABEL$, YLABEL$)
        LOCATE 3, 1: Print "S to stop"
        LOCATE 4, 1: Print "start time"
        LOCATE 5, 1: Print Time$
        LOCATE 8, 1: Print "range"
        LOCATE 9, 1: Print "1-10 V"
```

```
        LOCATE 10, 1: Print "total data"
        LOCATE 11, 1: Print "="; conumber%
        LOCATE 13, 1: Print "data"

        startime$ = Time$
        beginsecond = Timer

        For J1% = 0 To conumber% - 1

        dacbegin = Timer                        'start timing

        Call dproc(ADT0%, ADChan0%)
Rem         CALL movestep(stepsize%)

        indata0!(J1%) = ADT0%

        PSet (J1%, ADT0%)                       'draw on screen

        LOCATE 22, 1: Print Space$(79): LOCATE 22, 1
        If Gain% < 10 Then
            ADVol0! = ((ADT0% - 2048) / 2048) * gf!
        Else
            ADVol0! = (ADT0% / 4096) * gf!
        End If
        Print "present (V) = ";
        Print USING; "##.###"; ADVol0!

        If Gain% < 10 Then
        average = average + ((ADT0% - 2048) / 2048) * gf
        Else
        average = average + (ADT0% / 4096) * gf
        End If



        If J1% > 0 Then
            If Gain% < 10 Then
            LADvol! = ((indata0!(J1% - 1) - 2048) / 2048) * gf!
            Else
            LADvol! = (indata0!(J1% - 1) / 4096) * gf!
            End If
        LOCATE 22, 40
        Print "last (V) =";
        Print USING; "##.###"; LADvol!;
        End If

550     If (Timer - dacbegin) < dactime Then
            LOCATE 14, 1: Print J1%; " th"
            If UCase$(INKEY$) = "S" Then
BEEP:               LOCATE 23, 10
            stoptime$ = Time$
            totalsecond = Timer - beginsecond
            INPUT "stop detected, enter: 1--continue, 2--main menu >> ", cc1%
```

```
                If cc1% = 2 Then
                GoTo 60
                Else
                LOCATE 23, 1: Print Space$(80)
                GoTo 550
                End If
            End If
            GoTo 550
        End If

        Next J1%

        stoptime$ = Time$
        totalsecond = Timer - beginsecond
        average = average / conumber%
        Print "average is:", average

        BEEP
        LOCATE 6, 1: Print "stop time"
        LOCATE 7, 1: Print Time$
        LOCATE 23, 10
        Print "Data acquisition is done within"; totalsecond / 60; "munites, ";
        Print "hit any key to main menu. "
        Do While INKEY$ = "": Loop
        GoTo 60

'modification starts here
700     'step motor control and A/D

        unitstep% = 2           'unit step size for half step

Call moving(unitstep)

        GoTo 60

800     'Single-shot data acquisition with step motor control
        unitstep% = 4
        stepsize% = 10

        Print "This function is using the full step, turn the half step switch off!"
        Print "Use digital output 1 to drive the step motor!"
        'PRINT "This function does not use the divided by 10 chip, so the output should"
        'PRINT "         be the step motor output 1!"

        'INPUT "input pulse width (ms): ", PulseWidth%
        INPUT "Input step size (um): ", stepsize%
        stepsize% = stepsize% / unitstep%

        svpointer = 10          'pointer for saving data in single-shot mode
        datacq% = datacq% + 1
        CLS
        Print "single-shot data acquisition: hit any key when ready for next reading"
        Print "Press S key to stop the reading loop, press R key to redo last entry."
```

```
        Print "total number of reading <= "; conumber%
        Print "Half Step should be OFF!!!"
        Print "Connect Digital Output 1 to step motor TTL input "
        Print "number of steps are: ", stepsize%
        Print "hit any key to proceed >> "
        Do While INKEY$ = "": Loop

        CLS                     'print the column title
        Print "sequnce"; Space$(5); "voltage reading (V)"; Space$(5), "parameter"

        For j0% = 0 To conumber% - 1
        INPUT "enter a parameter (S for stop, R for redo last entry): ", ik$

        If UCase$(ik$) = "S" Then
BEEP:       LOCATE 23, 10
        INPUT "STOP detected, enter: 1--continue, 2--main menu >> ", cc1%
        j0% = j0% - 1
        If cc1% = 2 Then GoTo 60 Else GoTo 380
        ElseIf UCase$(ik$) = "R" Then
        j0% = j0% - 2: GoTo 880
        Else
        expara(j0%) = Val(ik$)
        End If

        Call delayA(20000)
        Call delayA(20000)

        Call dproc(ADT0%, ADChan0%)
        indata0!(j0%) = ADT0%

'converting into volt and be careful of overflow
        If Gain% < 10 Then
        ADVol0! = ((ADT0% - 2048) / 2048) * gf!
        Else
        ADVol0! = (ADT0% / 4096) * gf!
        End If

        Print j0% + 1; Space$(10); ADVol0!; Space$(10); expara(j0%); stepsize%

        'CALL movestepnew(stepsize%, PulseWidth%)
        Call movestep(stepsize%)
880     Next j0%

        BEEP
        LOCATE 24, 10
        Print "Data qcquission is done.  Hit any key to main menu. "
        Do While INKEY$ = "": Loop
        GoTo 60


'modification ends here by Fang 9-29-98

'modification starts by Fang 12-07-1998
```

```
900

      INPUT "Input Total number of data need to take: ", conumber%
      INPUT "Input laser Power (mW): ", Power!
      INPUT "Input the position of the water cell: ", Position$

905 INPUT "Enter output data file name: ", file$
      If file$ = "" Then GoTo 905
      Open file$ For Output As #2


      INPUT "Input threshold for the backscatterint> (V) A/D 0: ", Thback!
      INPUT "Input threshold for the Transmittance< (V) A/D 1: ", Thtrans!
      INPUT "Input threshold for the flash> (V) A/D 2: ", Thfls!

910 svpointer = 10          'pointer for saving data in single-shot mode
      sumation! = 0
      average! = 0

      Pback = 0
      Ptrans = 0
      Pfls = 0

      EngUnits! = 1!
      ULStat% = cbFromEngUnits%(BoardNum%, Gain%, EngUnits!, TrigValue%)

      datacq% = datacq% + 1
      CLS
      Print "data acquisition with external trigger at DigIn 1: Hit ENTER when ready for next 100 readings"
      Print "Press S key to stop the reading loop, press R key to redo last entry."
      Print "Total number of reading <= "; conumber%
      Print
      Print "Hit any key to proceed >> "
      Do While INKEY$ = "": Loop

      CLS                   'print the column title
      Print "Sequnce"; Space$(5); "Voltage reading (V)"; Space$(5), "Parameter"

      For j0% = 0 To conumber% - 1
'       INPUT "enter a parameter (S for stop, R for redo last entry): ", ik$

            ADSum0! = 0
            ADSum1! = 0
            ADSum2! = 0

            Print #2, j0%;

      If UCase$(INKEY$) = "S" Then
BEEP:             LOCATE 23, 10
            INPUT "STOP detected, enter: 1--continue, 2--main menu >> ", cc1%
            j0% = j0% - 1
            If cc1% = 2 Then
```

```
                Close #2
                GoTo 60
            Else
                GoTo 980
            End If
'       ELSEIF UCASE$(ik$) = "R" THEN
            j0% = j0% - 2: GoTo 980
        Else

            'configure AUXPORT for digital input
            '  Parameters:
            '    BoardNum    :the number used by CB.CFG to describe this board.
            '    PortNum%    :the input port
            '    Direction%  :sets the port for input or output

            PortNum% = AUXPORT
            BitNum% = 0
            counter% = 0

            ULStat% = cbDBitIn%(BoardNum, PortNum%, BitNum%, edge%)

            'read AUXPORT digital input and display

            ULStat% = cbDBitIn%(BoardNum, PortNum%, BitNum%, edge%)


            'Wait for the falling edge to trigger the data aquisition

            Do Until edge% = 1      'find HIGH first
            ULStat% = cbDBitIn%(BoardNum, PortNum%, BitNum%, edge%)
: Loop

            Do Until edge% = 0      ' LOW after HIGH is the falling edge
            ULStat% = cbDBitIn%(BoardNum, PortNum%, BitNum%, edge%)
: Loop


        End If

'  Get A/D data from ADChan0 for Backscattering
        Call dproc(ADT0%, ADChan0%)

'  Get A/D data from ADChan1 for Transmittance
        Call dproc(ADT1%, ADChan1%)

'  Get A/D data from ADChan2 for Flash
        Call dproc(ADT2%, ADChan2%)

'converting into volt and be careful of overflow
        If Gain% < 10 Then
            ADVol2! = ((ADT2% - 2048) / 2048) * gf!
        Else
            ADVol2! = (ADT2% / 4096) * gf!
```

```
        End If

'converting into volt and be careful of overflow
        If Gain% < 10 Then
                ADVol0! = ((ADT0% - 2048) / 2048) * gf!
        Else
                ADVol0! = (ADT0% / 4096) * gf!
        End If

'       IF ADVol0! > .01 THEN
'          counter% = counter% + 1
             sumation! = sumation! + ADVol0!
'       END IF

'converting into volt and be careful of overflow
        If Gain% < 10 Then
                ADVol1! = ((ADT1% - 2048) / 2048) * gf!
        Else
                ADVol1! = (ADT1% / 4096) * gf!
        End If

        Print #2, ADVol0!; ADVol1!; ADVol2!

        Print j0% + 1; Space$(5); ADVol0!; Space$(5); ADVol1!; Space$(5); ADVol2!

        If ADVol2! > Thfls Then
                Pfls% = Pfls% + 1
        End If

        If ADVol0! >= Thback Then
                Pback% = Pback% + 1
        End If

        If ADVol1! >= Thtrans Then
                Ptrans% = Ptrans% + 1
        End If

980     Next j0%

        BEEP
        LOCATE 24, 10

        Print "The probability for the reflection is: ", Pback% / conumber%
        Print "The probability for the spark from transmission is: ", Ptrans% / conumber%
        Print "The probability for the flash is: ", Pfls% / conumber%

'    INPUT "Do you want to continue?(Y/N)", continue$
'    IF UCASE$(continue$) = "N" THEN
'       GOTO 990
'    ELSE
'       GOTO 910
'    END IF
```

```
      Print #2, "The laser power is: ", Power!
      Print #2, "The position of the water cell is: ", Position$

      Print #2, "The backscattering threshold is: ", Thback
      Print #2, "The # of backscattering over the threshold is: ", Pback
      Print #2, "The transmittance threshold is: ", Thtrans
      Print #2, "The # of transmittance below the threshold is: ", Ptrans
      Print #2, "The Falsh theshold is: ", Thfls
      Print #2, "The # of Flash is: ", Pfls
990   Close #2
      Print "Data acquissition is done.  Hit any key to main menu. "
      Do While INKEY$ = "": Loop
      GoTo 60

'modification by Fang by 12-07-1998

1000  If datacq% > datasav% Then
CLS:            LOCATE 10, 1
         INPUT "YOUR DATA MAY NOT BE SAVED ! Do you want to save them (y/n) ? ", chc$
         If UCase$(chc$) = "N" Then GoTo 1100
         GoTo 60
      End If


1100  End

'************************************************

'*********************************************
Sub adpara(d%)

2000 CLS:    LOCATE 10, 1
      Print "the present value is: "; Count&
2010  INPUT "enter total # of A/D sample per data (< 2000): ", Count&
      Print "the new sample # is: "; Count&
      If Count& > 2000 Or Count& < 1 Then GoTo 2010

      Print "the present value is: "; Rate&
2100  INPUT "enter sample rate (sample # / s for each scan): ", Rate&
      Print "the new sample rate is: "; Rate&
      If Rate& > 50000 Or Rate& < 1 Then GoTo 2100

      If Count& / Rate& > dactime - 0.1 Then
      Print "the A/D time is too long, please redo "
      GoTo 2000
      End If

      Print "enter signal gain code: "
      Print "    code     <---->    voltage input range "
      Print "     1       <---->      +/- 10 V "
      Print "     0       <---->      +/- 5  V "
      Print "     2       <---->      +/- 2.5 V "
      Print "     3       <---->     +/- 1.25 V "
```

```
        Print "     5       <---->      +/- 0.625 V "
        Print "    100          <---->       0 - 10 V "
        Print "    101          <---->       0 - 5 V "
        Print "    102          <---->       0 - 2.5 V "
        Print "    104          <---->       0 - 1.25 V "
        Print
2200    INPUT "enter a code: ", Gain%
        Print "the new gain code is: "; Gain%

End Sub

Static Sub CountOut(PulseWidth%)
' this subroutine use 82C54 counter/timer 1 and 2 with internal 1MHz clock as
' square wave generator.
' The build in internal 1MHz clock is the input of CTR2.
' 1. Config CTR2 to have an output of 1MHz/CountValue2%;
' 2. Connect output of CTR2 (Pin 6) to the input of CTR1 (Pin 4);
' 3. Config CTR1 and get the square wave at its output (Pin 5)
' 4. The output frequency of CTR1 is 1MHz/CountValue2%/CountValue1%
' 5. The output of CTR1 (Pin 5) goes to one input of AND gate 7408 (Pin 13);
' 6. The Digite Output 1 (Pin 7) goes to another input of 7408 (Pin 12);
'    It is used to enable/disable the output of the square wave;
' 7. The final output comes from the output of 7408 (Pin 11).  This outpt
'    is connected to the step motor BNC output on the break out box
' 8. The GND and +5Vdc of the circult board also come from the CYDAS output.
'    GND is Pin 28 (Digital GND) and +5Vdc is Pin 29 (PC Bus +5V);

' The CTR0 was damaged during test, otherwise we do not have to use any other
' circult to achieve this function.  We can use all three counters to get the
' square wave with desired frequency.  The counter can be manually set
' enable/disable by the correspondent gate which takes over the function of
' the AND gate 7408.

'Varibles to be writen to 8254 control register to setup the timer

        Const BoardNum = 0              'Board Number for Cydas 802
        CounterNum2% = 3                'CTR2
        CounterNum1% = 2                'CTR1
        ConfigVal% = SQUAREWAVE         'See Mode 3 of 82C54 menu

' Config CTR2
        nDasErr = cbC8254Config%(BoardNum, CounterNum2%, ConfigVal%)
        If (nDasErr <> 0) Then
              BEEP
              Print "ERROR "; Hex$(nDasErr); " OCCURRED DURING 'cbC8254Config'": Stop
        End If

' Varibles for CYDAS 801 counter function
        RegNum1% = LOADREG2           'For CTR1 whoes CounterNum% is 2
        RegNum2% = LOADREG3           'For CTR2 whoes CounterNum% is 3
        CountValue2% = 100           '1MHz/CountValue2% at CTR2

'Load CounVal0% to CTR2 to get output with frenquency 1MHz/CountVal0%
```

```
        nDasErr = cbCLoad%(BoardNum, RegNum2%, CountValue2%)
        If (nDasErr <> 0) Then
            BEEP
            Print "ERROR "; Hex$(nDasErr); " OCCURRED DURING 'cbC8254Config'": Stop
        End If

'Config CTR1
        nDasErr = cbC8254Config(BoardNum, CounterNum1%, ConfigVal%)
        If (nDasErr <> 0) Then
            BEEP
            Print "ERROR "; Hex$(nDasErr); " OCCURRED DURING 'cbC8254Config'": Stop
        End If


'period count number based on 1MHz time base: nCountData=1000 --> rate=1kHz
        CountValue1% = PulseWidth%

' Write initial value to counter/timer 1 based on control
' this will enable the CTR1 pulse output
        nDasErr = cbCLoad%(BoardNum, RegNum1%, CountValue1%)
        If (nDasErr <> 0) Then
BEEP:               Print "ERROR "; Hex$(nDasErr); " OCCURRED DURING 'cbCLoad'": Stop
        End If

End Sub

Static Sub delay(d1%)
        BeginCount% = Timer
11000   EndCount% = BeginCount% + d1%
        If (Timer <= EndCount%) Then
            GoTo 11000
        Else
            GoTo 11010
            End If

11010   End Sub

Static Sub delayA(d1%)
        For j% = 1 To d1%
        a1 = 2.5 * 2.5 * 2.5 * 2.5 * 2.5 * 2.5 * 2.5
        Next j%

End Sub

'*********************************************************************
Static Sub dproc(ADT%, Chan%)

        Dim STotal As Long

'get data and stored in AdData%()
'       Options% = CONVERTDATA          ' return data as 12-bit values
'       ULStat% = cbAInScan%(BoardNum, LowChan%, HighChan%, Count&, Rate&, Gain%,
AdData%(0), Options%)
```

```
'       IF ULStat% = 84 THEN
'       PRINT "The CONVERT option cannot be used with 16 bit convertors. Set Options% to
NOCONVERTDATA."
'       STOP  'Change Options% above to NOCONVERTDATA (Options% = 0)
'       END IF
'       IF ULStat% <> 0 AND ULStat% <> 91 THEN STOP

'get signal at Chan% into digital data-DataValue% (0-4096) and average
        STotal = 0

        For i% = 0 To Count& - 1
        ULStat% = cbAIn%(BoardNum, Chan%, Gain%, ADT%)
        STotal = STotal + ADT%
        Next i%

        ADT% = STotal / Count&

End Sub

Sub gaincnvt(gf!)

        If Gain% = 1 Or Gain% = 100 Then gf! = 10
        If Gain% = 0 Or Gain% = 101 Then gf! = 5
        If Gain% = 2 Or Gain% = 102 Then gf! = 2.5
        If Gain% = 3 Or Gain% = 104 Then gf! = 1.25
        If Gain% = 5 Then gf! = 0.625

End Sub

'************************************************************************
Static Sub GRAPHICSINITIALIZE(XMIN, xmax, Ymin, Ymax, XLABEL$, YLABEL$)

'This routine puts up a graphics window, leaving room for axis labelling.
'It leaves the graphics screen in "real world" coordinates so no data
'transformations are necessary before plotting.  Also makes the last four
'lines of the screen a text window, so as to leave the graphics undisturbed.

Screen 9        'set up 640x350 graphics

VIEW (113, 1)-(638, 270), , 1   'initialize size of graphics window
                        'leaving room at left for labelling and
                        'four line text window at bottom
Color 7, 0

'if y label is > 18 characters, just take the first 18 characters
If Len(YLABEL$) > 18 Then YLABEL$ = Left$(YLABEL$, 18)
LASTCHAR% = Len(YLABEL$)
'print y axis label vertically in column 13 centered about line 10
For j% = 1 To LASTCHAR%
        LOCATE j% + 3, 13: Print Mid$(YLABEL$, j%, 1)
Next j%

'if the x label is longer than 39 characters, just take the first 39
```

```
If Len(XLABEL$) > 39 Then XLABEL$ = Left$(XLABEL$, 39)
LASTCHAR% = Len(XLABEL$)
'print x axis label on line 21 centered about column 46
LOCATE 21, 46 - LASTCHAR% / 2: Print XLABEL$

'print axis extrema
LOCATE 1, 1: Print Space$(13 - Len(Str$(Ymax))); Ymax
LOCATE 20, 1: Print Space$(13 - Len(Str$(Ymin))); Ymin
LOCATE 21, 15: Print XMIN
LOCATE 21, 67: Print Space$(13 - Len(Str$(xmax))); xmax

WINDOW (XMIN, Ymax)-(xmax, Ymin)    'define graphics window
                            'in "real world" coordinates

PSet (XMIN, Ymin)     'put the graphics pen in the lower left corner
                  'use "LINE -(xpoint,ypoint)" to connect points.

End Sub

Sub movestep(stepsize%)         'added by Fang on 09-22-98

For i% = 0 To stepsize% - 1

      ErrorCode% = cbDBitOut(0, AUXPORT, 0, 1)        'goto high one step
      Call delayA(50)
'      PRINT "high ", i%
      ErrorCode% = cbDBitOut(0, AUXPORT, 0, 0)        'goto low
      Call delayA(100)
Next i%

End Sub

DefSng H-Z
Sub movestepnew(distance%, PulseWidth%)

'By Qiyin Fang on April 17, 2000

'Step motor control using 82C54 counter to generate square wave with precise
'pulse width, while using Digital Input 2 to control the number of pulses.
'It requires to connect the step motor output 1 on the Cydas802 break out box
'to its digital input 2.
'(i)    Config the 82C54 counter on Cydas 802 A/D board
'      through SUB Countout()
'(ii)   Config the Digital Output 1 to enable/disable output at step motor
'      output 1 using a 7408 AND gate.  The 7490 divid-by-10 chip is NOT
'      used.
'(ii)   The Digital input 2 is used to count the number of pulses sending out
'      from step motor output 1 so as to control the steps moved in the motor.


'configure AUXPORT for digital input
'  Parameters:
'    BoardNum    :the number used by CB.CFG to describe this board.
```

```
'    PortNum%    :the input port
'    Direction%  :sets the port for input or output

      Const BoardNum = 0              'Board Number for Cydas 802
      Dim PortNum As Integer          'Specifies the port number for Digital Input
      Dim BitNum As Integer           'Specifies which bit to read BitValue
      Dim counter As Integer          'iterate parameter for pulse counting
      Dim edge As Integer             '1 for HIGH and 0 for LOW
      Dim PulseWidth As Integer       'pulse width for square wave


      PortNum% = AUXPORT      'Digital Input
      BitNum% = 1             'Digital Input 1 on Cydas 802
      counter% = 0            'Initial value

      ' Configure the 82C54 Counter Output.  The step motor output is
      ' disabled sine the Digial Output 1 is LOW
'      INPUT "Input Counter Output pulse width:(ms)", PulseWidth%     'test use only
      PulseWidth% = PulseWidth% * 20
      Call CountOut(PulseWidth%)

      'enable the motor driving by set Digital Output 1 HIGH
      dwOUTVal% = 1
      nDasErr = cbDBitOut(0, AUXPORT, 0, dwOUTVal%)
      If nDasErr <> 0 Then
BEEP:               Print "ERROR "; Hex$(nDasErr); " DURING 'cbDBitOut'": Stop
      End If

      'Count the number of pulses by counting the rising edges.
      'Terminate when Distance is reached
      Do Until counter% = distance%
            Do Until edge% = 1  'find High first
                  ULStat% = cbDBitIn%(BoardNum, PortNum%, BitNum%, edge%)
: Loop

            Do Until edge% = 0  ' LOW after HIGH is the falling edge
                  ULStat% = cbDBitIn%(BoardNum, PortNum%, BitNum%, edge%)
: Loop

            counter% = counter% + 1
            Print "The Current Count is: ", counter%
: Loop

      'Disable the step motor driving output
      dwOUTVal% = 0
      nDasErr = cbDBitOut(0, AUXPORT, 0, dwOUTVal%)
      If nDasErr <> 0 Then
BEEP:               Print "ERROR "; Hex$(nDasErr); " DURING 'cbDBitOut'": Stop
      End If

End Sub

DefInt H-Z
```

```
Static Sub moving(stpsz%)
' this subroutine use 8254 counter/timer 1 and 2 with internal 1MHz clock as
' square wave generator and a divide-by-ten dividing circuit to drive the
' motor (ref: user's guide, p.E-20)

' The build in internal 1MHz clock is the input of CTR2.
' 1. Config CTR2 to have an output of 1MHz/CountVal0%;
' 2. Connect output of CTR2 (Pin 6) to the input of CTR1 (Pin 4);
' 3. Config CTR1 and get the square wave at its output (Pin 5) before
'    the divided by 10 chip 7490;
' 4. CTR1 output (Pin5) goes to the input of 7490 (Pin 1) on the home made
'    circult board;
' 5. The output of 7490 goes to one input of AND gate 7408 (Pin 13);
' 6. The Digite Output 1 (Pin 7) goes to another input of 7408 (Pin 12);
'    It is used to enable or disable the output of the square wave;
' 7. The final output comes from the output of 7408 (Pin 11).  This outpt
'    is connected to the BNC output Dig1 in the box through a switch, which
'    enable us to choose between Digital output 1 and this output;
' 8. The GND and +5Vdc of the circult board also come from the CYDAS output.
'    GND is Pin 28 (Digital GND) and +5Vdc is Pin 29 (PC Bus +5V);

' The CTR0 was damaged during test, otherwise we do not have to use any other
' circult to achieve this function.  We can use all three counters to get the
' square wave with desired frequency.  The counter can be manually set
' enable/disable by the correspondent gate which takes over the function of
' the AND gate 7408.

'Varibles to be writen to 8254 control register to setup the timer

      Const BoardNum = 0
      CounterNum0% = 3              'CTR2
      CounterNum% = 2               'CTR1
      ConfigVal% = SQUAREWAVE       'See Mode 3 of 82C54 menu

' Config CTR2
      nDasErr = cbC8254Config%(BoardNum, CounterNum0%, ConfigVal%)
      If (nDasErr <> 0) Then
      BEEP
      Print "ERROR "; Hex$(nDasErr); " OCCURRED DURING 'cbC8254Config'": Stop
      End If

' Varibles for CYDAS 801 counter function
      RegNum% = LOADREG2          'For CTR0 whoes CounterNum% is 1
      RegNum0% = LOADREG3         'For CTR2 whoes CounterNum% is 3
      CountVal0% = 500            '1MHz/CountVal0% at CTR2

'Load CounVal0% to CTR2 to get output with frenquency 1MHz/CountVal0%
      nDasErr = cbCLoad%(BoardNum, RegNum0%, CountVal0%)
      If (nDasErr <> 0) Then
      BEEP
      Print "ERROR "; Hex$(nDasErr); " OCCURRED DURING 'cbC8254Config'": Stop
      End If
```

```
'Config CTR0
        nDasErr = cbC8254Config(BoardNum, CounterNum%, ConfigVal%)
        If (nDasErr <> 0) Then
        BEEP
        Print "ERROR "; Hex$(nDasErr); " OCCURRED DURING 'cbC8254Config'": Stop
        End If


' Prompts for motor operation variables
CLS:          LOCATE 10, 10
5050    INPUT "Enter the distance of travel in unit of (um)  >>>  ", distance
        If distance > 80000 Then
        Print "you must enter distance less than 80 mm, please redo"
        GoTo 5050
        End If
5070    Print "after the input of following data, motor will run !!! "
        INPUT "Enter motor speed in unit of (um/s)   >>>  ", speed

' (1) prdcnt (<1,000) is the number of base period (1us*CountVal0%)
'     for each output pulse @ CTR0 OUT @ rate=rate0/prdcnt which must be
'     > 3(Hz), rate0=1MHz/CountVal0%
' (2) divide-by-mv% chips was added for lower rate: rate=rate0/(prdcnt*mv%)
'     which becomes > 3/mv%(Hz)
' (3) with stepsz% in unit of (um) and speed of (um/s) thus:
'       speed = rate * stpsz% = 100000*stpsz!/prdcnt/mv%

        mv% = 10     ' should be 10 with the 7490 divided by 10 chip

        prdcnt = 1000000 * stpsz / speed / mv% / CountVal0%

        If prdcnt > 2000 Then
        Print "you must enter a larger speed (um/s), please redo"
        GoTo 5070
        End If

        Traveltime = distance / speed
        Print "Travel time is: ", Traveltime
        Print "Speed is: ", speed
        Print "prdcnt is: ", prdcnt
        Print "distance is: ", distance

'period count number based on 1MHz time base: nCountData=1000 --> rate=1kHz
        nCountData% = prdcnt%

' Write initial value to counter/timer 1 based on control
' this will enable the CTR1 pulse output
        nDasErr = cbCLoad%(BoardNum, RegNum%, nCountData%)
        If (nDasErr <> 0) Then
BEEP:         Print "ERROR "; Hex$(nDasErr); " OCCURRED DURING 'cbCLoad'": Stop
        End If

5090    n = 0: totaltime = 0: prvstime = 0
```

```
'start of the driving loop
5100    dwOUTVal = 1
'enable the logic gates in the home-made control circuit for motor driver
'by set Dig1 output 1
      Print "cbDBitOut output 1"
      nDasErr = cbDBitOut(0, AUXPORT, 0, 1)
      If nDasErr <> 0 Then
      BEEP
      Print "ERROR "; Hex$(nDasErr); " DURING 'cbDBitOut'": Stop
      End If
      Print "Running ...  press S to STOP:  "

      begintime = Timer
Print prvstime; begintime

'time control loop
      While totaltime < Traveltime
            If UCase$(INKEY$) = "S" Then
            dwOUTVal = 0                'stop the motor driving
                                        'by set Dig1 out 0
            nDasErr = cbDBitOut(0, AUXPORT, 0, 0)
                  If nDasErr <> 0 Then
BEEP:                       Print "ERROR "; Hex$(nDasErr); " DURING 'cbDBitOut'": Stop
                  End If
            prvstime = Timer - begintime + prvstime: BEEP
            INPUT "press: 1--continue; 2--menu  ", n1%
                  If n1% = 2 Then GoTo 5200 Else GoTo 5100
            End If
            totaltime = Timer - begintime + prvstime
            If totaltime > (Traveltime - 7) Then       'start of the ending warning
            SOUND 200 + n, 1
            n = n + 1
            End If

      Wend

      dwOUTVal = 0                  'stop the motor driving
      nDasErr = cbDBitOut(0, AUXPORT, 0, 0)
      If nDasErr <> 0 Then
BEEP:               Print "ERROR "; Hex$(nDasErr); " DURING 'cbDBitOut'": Stop
      End If
BEEP:       BEEP: BEEP

'end of drivng loop

      Print "total time: "; totaltime; "(s),   speed: "; distance / totaltime; "(um/s)"
'      IF dir = 0 THEN dir = 1 ELSE dir = 0           'direction toggle
      INPUT "Toggle direction and run again (y/n) ? ", ch20$
      If UCase$(ch20$) = "N" Then GoTo 5200
      GoTo 5090

5200    End Sub
```

```
Sub procpara(st1$, Ymin%, Ymax%)

CLS:        LOCATE 10, 1
      Print "the present value is: "; conumber%
4000   INPUT "enter total # of data you want to take (<10000): ", conumber%
      Print "the new data # is: "; conumber%
      If conumber% > 10000 Or conumber% < 1 Then GoTo 4000

      Print "the present value is: "; dactime
      INPUT "enter time between data acquisition (in seconds): ", dactime
      Print "the new data-taking time (s) is: "; dactime

      INPUT "enter test parameter: ", st1$

      INPUT "enter Y_mim (0 - 4096) for screen display: ", Ymin%
      INPUT "enter Y_max (0 - 4096) for screen display: ", Ymax%

End Sub

'*************************************************
Sub saving(startime$, stoptime$, st1$, totalsecond, K1%)

3000   LOCATE 22, 1
      INPUT "enter output data file name: ", fil$
      If fil$ = "" Then GoTo 3000
      Open fil$ For Output As #1

      timemark$ = startime$ + "---" + stoptime$
      Print #1, Date$, timemark$
      Print #1, "total seconds: ", totalsecond
      Print #1, "total number of data: ", K1%
      Print #1, "Input Voltage Range: "; Gain%
      Print #1, "total # of sample per A/D = "; Count&
      Print #1, "sampling rate = "; Rate&
      Print #1, st1$

      Print #1, "Reflection probability: ", Pback% / conumber%
      Print #1, "Spark probability: ", Ptrans% / conumber%

      Print #1, "-----------"

'   IF svpointer = 10 THEN
'   PRINT #1, "#    "; " data count"; "  parameter"
'   ELSE
'   PRINT #1, "#    "; " data count"
'   END IF

      For p1% = 0 To K1% - 1
'      IF svpointer = 10 THEN
'
'         PRINT #1, p1% + 1, indata%(p1%), expara(p1%)
'      ELSE
                'converting into volt and be careful of overflow
```

```
'               IF Gain% < 10 THEN
'                     PRINT #1, p1% + 1, ((indata%(p1%) - 2048) / 2048) * gf!
'               ELSE
'                     PRINT #1, p1% + 1, (indata%(p1%) / 4096) * gf!
'               END IF
                Print , p1% + 1, indata0!(p1%), indata1!(p1%), indata2!(p1%)
                Print #1, p1% + 1, indata0!(p1%), indata1!(p1%), indata2!(p1%)
'       END IF
        Next p1%

        Close

End Sub

'*****************************************
Static Sub selemenu(ha)

        Screen 0: CLS: LOCATE 10, 1
        Print "SELECT:"

        'modify starts here
'       PRINT " 7 ---- Step motor control only"
'       PRINT " 8 ---- Single Shot Data Acquisition with Step Motor Control"
        'modify ends here by Fang 9-29-98

        'modify starts here
        Print " 9 ---- Data acquisition for backscattering measurement"
        'modify ends here by Fang 12-07-98

        Print " 1 ---- Setting A/D parameters "
        Print " 2 ---- Setting data acquisition parameters"
        Print
'       PRINT " 3 ---- Start single-shot data acquisition"
'       PRINT " 4 ---- Start continuous data acquisition "
        Print
        Print " 5 ---- Saving data to file "
        Print " 6 ---- exit "
        Print
        INPUT " enter a number: ", ha

End Sub
```